

**FIRST-PRINCIPLES STUDY OF
MAGNETOELECTRIC EFFECTS AND
FERROELECTRICITY IN COMPLEX OXIDES**

BY MENG YE

A dissertation submitted to the
Graduate School—New Brunswick
Rutgers, The State University of New Jersey
in partial fulfillment of the requirements
for the degree of
Doctor of Philosophy
Graduate Program in Physics and Astronomy

Written under the direction of
Professor David Vanderbilt
and approved by

New Brunswick, New Jersey

October, 2016

ABSTRACT OF THE DISSERTATION

First-principles study of magnetoelectric effects and ferroelectricity in complex oxides

by Meng Ye

Dissertation Director: Professor David Vanderbilt

This thesis contains several investigations of magnetoelectric effects and ferroelectricity in complex oxides studied via first-principles calculations. We start by reviewing the mechanisms of ferroelectricity and magnetoelectric effects, and then we give a brief introduction to the first-principles computational methods that are involved. Next, our investigations are divided into two parts. The first half focuses on the magnetoelectric effects, while the second half is mainly on ferroelectricity. The first half aims to examine the lattice contribution to the magnetoelectricity by investigating the dynamical magnetic charge tensors induced by different mechanisms. Through the study of Cr_2O_3 and a fictitious material KITPite, we find that the dynamical magnetic charges driven by exchange striction are more significant than the ones induced by spin-orbit coupling. Since the lattice contribution to the magnetoelectric effect is proportional to the dynamical magnetic charges, we also study the magnetic charges and the magnetoelectric coupling in hexagonal manganite RMnO_3 and ferrite RFeO_3 . Our results further confirm the importance of the exchange-striction mechanism in inducing large magnetic

charges, but we also notice that the magnetoelectric contributions from various phonons tend to cancel each other, leading to a great reduction of the total coupling. These investigations not only provide a prediction of the magnetoelectric coupling constant in $RMnO_3$ and $RFeO_3$, but also emphasize the importance of phonons in magnetoelectric coupling. In the second half of the thesis, we focus on predicting new ferroelectrics in the family of corundum derivatives. Many new corundum derivatives have been synthesized recently; these are automatically polar, and many are magnetic as well. However, a polar material is only called ferroelectric if the polarization is reversible by an external field, and it is not yet clear whether or not this is the case for these new materials. Motivated by this question, we use a structural constraint method to study the ferroelectric reversal path and energy barrier of several corundum derivatives. As a result, we predict several FE candidates with insulating reversal paths and low barrier energies. Since the hysteresis behavior of ferroelectrics is attributed to the ferroelectric domain wall motion, we further investigate the formation and motion of ferroelectric domain walls in corundum derivatives. Our study predicts the atomic structure and orientation of the ferroelectric domain wall, as well as the shape of ferroelectric domains. In addition, we find novel properties at domain walls, including a strong magnetoelectric coupling and an interlocking between chirality and polarization. Moreover, we use the structural constraint method to study the barrier energy of ferroelectric domain wall reversal. Our results suggest that the barrier energy is linearly correlated with the bond valence sum, which can be used as a guide to find new ferroelectrics in the family of corundum derivatives.

Acknowledgements

I still remember the first day I came to Rutgers five years ago. I still have the receipt of the one-way flight from China to Newark, New Jersey. After five years, Rutgers, 11 thousand kilometers away from my hometown, has become a home away from my home. Five years is not a long time compared with one's lifetime, but this five years is definitely unforgettable. In this five years, I lived in a different country, I got married, and I got my Ph.D in physics. There are many people in my mind that I want to acknowledge.

Han Yu, a Chinese essayist and poet from the Tang dynasty, said "A teacher is one who transmits knowledge, provides for study and dispels confusion." This is an accurate depiction of my advisor Professor David Vanderbilt. He is always willing to teach me from scratch and answer my endless questions. His rigorous, modest, gentle, and professional attitudes guided me from every aspect about how to be a physicist and a respectful person. I not only appreciate all his contributions of time, creative ideas, and funding support, but also that he gave enough trust and freedom to me to explore on my own direction and at my own pace. He encouraged and supported me to attend many workshops, symposiums, and conferences, which gradually led me to be a good speaker and listener. I am so thankful that I have Professor David Vanderbilt as my advisor, who makes my Ph.D. experience productive, joyful, and stimulating.

I thank my committee members Professor Jane Hinch, Professor Charles Keeton, Professor Premala Chandra, and my outside committee member Professor Ismaila Dabo from Penn State. Their questions and active feedback deepened my understanding.

I also want to thank Professor Karin Rabe for her thought-provoking and inspiring questions and suggestions. The big smile on her face and her excitement towards new and bold ideas left deep impressions on me.

It was a very pleasant experience to collaborate with Professor Martha Greenblatt and Dr. Manrong Li. I feel fortunate that they introduced the interesting materials, the corundum derivatives, to me. Each interaction with them taught me to think about the physical problems from different perspectives.

My sincere thanks also go to Professor Sang-Wook Cheong for his inspiration and advice. In the last year of my Ph.D. program, I had many interactions with him and he greatly motivated me to learn more from experimentalists. His advices will be a great treasure for my future research.

I want to express my gratitude to Professor Weida Wu. He is very gentle, patient, and knowledgeable. I learned a lot about experiments as well as theories from him.

I want to give special thanks to Professor Premala Chandra and her efforts in the organization of “Women’s Lunch” activities. I thank all the attendees of “Women’s Lunch” for sharing their stories of personal lives and academic careers. Their advices and encouragements will accompany me through different stages of my life.

I would like to express my appreciation to Professor Jolie Cizewski. I have worked as a teaching assistant in her courses for several semesters and I have helped her proctoring many exams. Her rigorous attitude towards teaching and her endless efforts to achieve fairness will guide me to be a responsible teacher.

Confucian said, “When I walk along with two others, they may serve me as my teachers”. My thanks go to the postdoc fellows, graduate students at Rutgers, including Jianpeng Liu, Maryam Taherinejad, Yuanjun Zhou, Sebastian Reyes-Lillo, Qibin Zhou, John Bonini, Bartomeu Monserrat, Cyrus Dreyer, Michele Kotiuga, Xiaohui Liu, Jialan Zhang, Se Young Park, Turan Birol, Hongbin Zhang, Sergey Artyukhin, Joseph Bennett, Huaqing Huang, Andrei Malashevich, Fei-Ting Huang, Yazhong Wang, Xueyun Wang, Wenbo Wang, Wenhan Zhang, Shuchen Zhu, Qiang Han, Yanan Geng, Jae Wook Kim, Juho Lee, Chris Munson, Huijie Guan, Wenhui Xu, Wenshuo Liu, Can Xu, Jianguo Xiao, and Xukai Yan. I benefitted a lot from the enlightening discussion with them and they enriched my graduate life.

I cannot thank more for my husband Mohan Chen. He has made great efforts to come across the Pacific to Princeton and accompanied me for four years. We have

embraced the beauty of cherry blossom in the spring and have chased the foliage in the fall. We together have faced a winter storm in May and we have marched in the desert when all the families were enjoying turkeys and pumpkins. I like adventures because Mohan is always by my side to back me up. I hope our adventures in physics would last forever.

In the end, I would like to express my gratitude to my family. Although we are 11 thousand kilometers apart, we still share the same joy, sorrow, and the clear bright moonlight on Mid-Autumn Day.

Dedication

to Jianjian and his friends for their company days and nights

Table of Contents

Abstract	ii
Acknowledgements	iv
Dedication	vii
List of Tables	xi
List of Figures	xv
1. Introduction	1
1.1. Motivations	1
1.2. Ferroelectricity	3
1.2.1. General properties	3
1.2.2. Ferroelectric phase transition	5
1.2.3. Soft modes and boundary conditions	7
1.2.4. Beyond the soft-mode ferroelectricity	9
1.3. Magnetoelectricity and multiferroicity	10
1.3.1. Brief history	10
1.3.2. Mechanisms	13
1.4. Outline of the present work	15
2. Computational methods	18
2.1. Density functional theory	19
2.1.1. Kohn-Sham equations	19
2.1.2. Exchange-correlation functionals	20
2.1.3. On-site Coulomb correction	21
2.1.4. Practical implementations	21

2.2. Phonons	22
2.3. Modern theory of polarization	23
3. Dynamical magnetic charges and magnetoelectric effects	29
3.1. Introduction	29
3.2. Formalism	31
3.3. Structure and symmetry	36
3.3.1. Cr ₂ O ₃	36
3.3.2. KITPite	36
3.4. First-principles methodology	38
3.5. Results and discussion	39
3.5.1. Structure and phonon	39
3.5.2. Born charge	40
3.5.3. Magnetic charge	41
3.5.4. Electric and magnetic responses	42
3.6. Summary and outlook	44
4. Magnetoelectric effects in hexagonal rare-earth manganites and fer-	
rites	45
4.1. Introduction	45
4.2. Preliminary	47
4.2.1. Structure and magnetic phase	47
4.2.2. Symmetry analysis	49
4.3. First-principles methodology	51
4.4. Results and discussion	52
4.4.1. Born charge and force-constant matrix	52
4.4.2. Magnetization and magnetic charge	52
4.4.3. Magnetoelectric effect	57
4.5. Summary and outlook	61

5. Ferroelectricity in corundum derivatives	62
5.1. Introduction	62
5.2. Preliminary	64
5.2.1. Structure	64
5.2.2. Coherent ferroelectric reversal	65
5.2.3. Energy profile calculation	67
5.3. First-principles methodology	67
5.4. Results and discussion	68
5.4.1. Ground state structure and magnetic order	70
5.4.2. Symmetry of the reversal path	72
5.4.3. Polarization reversal barrier	76
5.4.4. Insulating vs conducting	80
5.4.5. More complicated magnetic structures	82
5.4.6. Hyperferroelectric?	84
5.5. Summary and outlook	85
6. Ferroelectric and magnetoelectric domain walls in corundum deriva-	
tives	87
6.1. Introduction	87
6.2. First-principles methodology	89
6.3. Results and discussion	89
6.3.1. Construction of domain walls	89
6.3.2. Orientation of domain walls	92
6.3.3. Magnetic and magnetoelectric domain walls	94
6.3.4. Domain wall reversal	98
6.4. Summary and outlook	103
7. Conclusion and outlook	105
References	108

List of Tables

3.1. Structural parameters of Cr_2O_3 from first-principles calculation and experiments: rhombohedral lattice constant a , lattice angle α , and Wyckoff positions for Cr (4c) and O (6e).	39
3.2. Frequencies (cm^{-1}) of IR-active phonon modes of Cr_2O_3 from first-principles calculations and experiments. The two A_{2u} modes are at longitudinal direction; the four E_u modes are at transverse direction (doubly degenerate).	40
3.3. Magnetic charges Z^m ($10^{-2}\mu_B/\text{\AA}$) for Cr_2O_3 in the atomic basis. . . .	41
3.4. Magnetic charges Z^m ($10^{-2}\mu_B/\text{\AA}$) for KITPite $\text{CaAlMn}_3\text{O}_7$ in atomic basis.	42
3.5. Top: Mode decomposition of the Born charges Z^e , and of the spin and orbital contributions to the magnetic charges Z^m , in Cr_2O_3 . C_n are the eigenvalues of the force-constant matrix. Bottom: Total A_{2u} -mode (longitudinal) and E_u -mode (transverse) elements of the lattice-mediated electric susceptibility χ^e , magnetic susceptibility χ^m , and the spin and orbital parts of the ME constant α	43
3.6. Born charges Z^e and magnetic charges Z^m for IR-active A_{2u} modes in $\text{CaAlMn}_3\text{O}_7$. C_n are the eigenvalues of the force-constant matrix.	43
4.1. Symmetry patterns of Born charges Z^e , magnetic charges Z^m and ME tensors α in RMnO_3 and RFeO_3 . Patterns for Mn, Fe, O_{T1} , and O_{T2} are for atoms lying on an M_y mirror plane. Unless otherwise specified, patterns apply to both A_1 and A_2 phases.	50
4.2. Atomic Born charge tensors Z^e (in units of $ e $) for RMnO_3 and LuFeO_3 in the A_2 phase. TM = Mn, Fe.	53

4.3. Eigenvalues of the force-constants matrix ($\text{eV}/\text{\AA}^2$) for IR-active modes in RMnO_3 and LuFeO_3 in the A_2 phase, and for HoMnO_3 in the A_1 phase	54
4.4. Longitudinal magnetic charge components Z^m ($10^{-3} \mu_B/\text{\AA}$) of RMnO_3 and LuFeO_3 in the A_2 phase. All components vanish in the absence of SOC.	55
4.5. Transverse magnetic charge components Z^m ($10^{-2} \mu_B/\text{\AA}$) of HoMnO_3 in the A_1 phase, as computed including or excluding SOC.	56
4.6. Transverse magnetic charge components Z^m ($10^{-2} \mu_B/\text{\AA}$) of RMnO_3 and LuFeO_3 in the A_2 phase, as computed including or excluding SOC. . . .	57
4.7. Computed ME couplings α_{zz} (longitudinal) and α_{xx} and α_{yx} (transverse) for RMnO_3 and LuFeO_3 (ps/m). Spin-lattice, spin-electronic, and total spin couplings are given as computed with and without SOC.	58
4.8. Transverse ME contributions (ps/m) from IR-active modes for A_2 and A_1 phases of HoMnO_3 and A_2 phase of LuMnO_3 . Results are given in ascending order of force-constant eigenvalues, which are reported in Table 4.3.	60
5.1. Corundum-derived structures before and after polarization reversal. . .	66
5.2. Rhombohedral structural parameters of LNO-type ABO_3 corundum derivatives LiNbO_3 , LiTaO_3 , ZnSnO_3 , FeTiO_3 and MnTiO_3 from our first-principles calculations and experiments [111, 127, 128, 129, 130]. The Wyckoff positions are 2a for A and B cations, and 6c for oxygen anions (note that $A_x = A_y = A_z$ and $B_x = B_y = B_z$). The origin is defined by setting the Wyckoff position B_x to zero.	69

5.3.	Rhombohedral structure parameters of ordered-LNO $A_2BB'O_6$ corundum derivatives Li_2ZrTeO_6 , Li_2HfTeO_6 , Mn_2FeWO_6 , Mn_3WO_6 and Zn_2FeOsO_6 from our first-principles calculations and experiments [115, 44]. Wyckoff positions are 1a for A_1 , A_2 , B and B' cations, and 3b for O_1 and O_2 anions. The origin is defined by setting the Wyckoff position B'_x to zero. For ordered-LNO Li_2HfTeO_6 and Zn_2FeOsO_6 , no experimental results are available. Magnetic orders used in the calculation for Mn_2FeWO_6 , Mn_3WO_6 , and Zn_2FeOsO_6 are also indicated by “Mag”.	69
5.4.	Oxidation states of the LNO-type ABO_3 and the ordered-LNO $A_2BB'O_6$ corundum derivatives. The oxidation state of O ion is -2 in all materials.	70
5.5.	Magnetic energy of different magnetic states relative to the lowest-energy state in Mn_2FeWO_6 and Mn_3WO_6 , in units of meV per unit cell.	71
5.6.	Relative spin direction between different magnetic ions in Mn_2FeWO_6 and Mn_3WO_6 . Here “FM” means ferromagnetic.	72
5.7.	Energy and unstable phonon modes at the midpoint structure of $LiNbO_3$, $LiTaO_3$, $ZnSnO_3$, $FeTiO_3$ and $MnTiO_3$ with symmetry $R\bar{3}c$ and $R\bar{3}$. The energy of the ground-state structure is set to be zero as reference and the unit is meV per unit cell. The imaginary frequency of the unstable phonon is given in units of cm^{-1}	73
5.8.	Coherent polarization reversal barrier E_{barrier} (meV) per unit cell and spontaneous polarization P_S ($\mu C/cm^2$) for FE candidates.	77
5.9.	Midpoint structures of ordered-LNO candidates and the energy differences between B and B' sandwiched midpoint structures. The distances between A_1 (or A_2) cation and the oxygen planes in the ground state are characterized by ξ_{1S} (or ξ_{2S}). The energy difference between the B and B' sandwiched midpoint structures is ΔE . The Madelung energy difference between the B and B' sandwiched midpoint structures is ΔE^M .	78

5.10. Magnetic energies for AFM doubled-cell magnetic structures. ΔE_1 is for energies evaluated at the unrelaxed experimental structure, while ΔE_2 applies to energies calculated after relaxation of the internal coordinates. The energy is given with respect to the <i>udu</i> magnetic order in the experimental cell with unit meV/f.u.	83
5.11.	84
6.1. Formation energy of X-wall and Y-wall. For the ordered-LNO structure, the formation energy is averaged between the $DW_{\uparrow\downarrow}$ and $DW_{\downarrow\uparrow}$. The unit is mJ/m ²	94
6.2. DW-mediated polarization reversal barrier E_{barrier} for corundum derivatives. The energy barriers of $DW_{\uparrow\downarrow}$ and $DW_{\downarrow\uparrow}$ are the same in LNO-type structures, but different in ordered-LNO structure. The unit of E_{barrier} is meV per unit cell.	100

List of Figures

1.1. The cross coupling between polarization, magnetization, and strain. The electric field \mathbf{E} , magnetic field \mathbf{H} , and stress $\boldsymbol{\sigma}$ control the electric polarization \mathbf{P} , magnetization \mathbf{M} , and strain $\boldsymbol{\varepsilon}$, respectively. This figure is taken from [2].	2
1.2. Relationship between dielectric, piezoelectric, pyroelectric and ferroelectric.	3
1.3. Sketch of \mathbf{P} - $\boldsymbol{\varepsilon}$ relation of (a) a dielectric and (b) a FE. (c) The first FE hysteresis loop of rochelle salt taken from Ref. [1].	4
1.4. PE-FE phase transition described by the Landau-Ginzburg-Devonshire theory. (a) Free energy as a function of polarization in the vicinity of T_c in the absent of an external electric field. (b) Free energy as a function of polarization in the FE phase at various electric fields. (c) Evolution of polarization as a function of an external electric field at various of temperatures. Hysteresis loop 1-2-3-1'-2'-3' is observed in the FE phase.	6
1.5. The FE structure (a) and the centrosymmetric reference structure (b) of PbTiO_3 . The arrow in (b) represent the magnitude of the atomic displacement in the unstable polar mode, where the position of Pb cation is fixed as the origin.	7
1.6. (a) $\boldsymbol{\mathcal{E}} = 0$ and (b) $\mathbf{D} = 0$ boundary conditions for FEs.	9
1.7. Publication per year with keyword “magnetoelectric” according to the <i>Web of Science</i>	12
1.8. Dzyaloshinskii-Moriya interaction. The open red circle represents oxygen ion. The filled blue circle and filled blue arrow are magnetic ion and its spin.	14

1.9.	Exchange-striction interaction. (a) The cation-anion-cation bond without external fields. (b) The cation-anion-cation bond in the presence of an electric field. The open red circle represents oxygen ion. The filled blue circle and filled blue arrow are magnetic ion and its spin.	15
2.1.	A 1D chain of alternating anions and cations. The distance between each anion and cation is $a/2$. The two dashed rectangles indicate two different choices of unit cell.	24
2.2.	An experimental setup to measure the spontaneous polarization in ferroelectric materials. The ferroelectric sample is inserted into a shorted capacitor. Free charges are accumulated on top and bottom of the capacitor to screen out the bulk polarization. When the bulk polarization is reversed from (a) to (b) by an electric field, current flows through the ammeter in the shorted wire to re-screen the bulk polarization.	25
2.3.	Polarization as a function of λ . The formal polarization is a multivalued quantity and at a certain λ value, the polarization in different branches differ by an integer times the polarization quantum \mathbf{P}_Q . Within each path, the polarization stays on the same branch and changes continuously.	28
3.1.	Sketch for different contributions to magnetoelectric effect. (a) The high symmetry system under no external field. (b) The electronic, (c) ionic, and (d) strain-mediated contributions. The small blue circle represents ion, the large red oval represents electron cloud, and the black outline represents the unit cell.	29
3.2.	Sketch showing how the six lattice-mediated responses indicated by solid circles are built up from the four elementary tensors indicated by open circles: the Born charge Z^e , magnetic charge Z^m , internal strain Λ , and force-constant inverse K^{-1} . Each lattice-mediated response is given by the product of the three elementary tensors connected to it, as indicated explicitly in Eqs. (3.11-3.16).	34

3.3.	Structure of Cr_2O_3 . (a) In the primitive cell, four Cr atoms align along the the rhombohedral axis with AFM order represented by the arrows on Cr atoms. (b) Each Cr atom is at the center of a distorted oxygen octahedron.	35
3.4.	Symmetry pattern of Born and magnetic charge tensors for (a) the Cr atom in Cr_2O_3 , (b) the O atom in Cr_2O_3 and the O^2 atom in $\text{CaAlMn}_3\text{O}_7$, (c) the Ca, Al and O^1 atoms in $\text{CaAlMn}_3\text{O}_7$, and (d) the Mn and O^3 atoms in $\text{CaAlMn}_3\text{O}_7$. The elements indicated by an asterisk vanish in the absence of SOC for Z^m in $\text{CaAlMn}_3\text{O}_7$	36
3.5.	Planar view of the $\text{CaAlMn}_3\text{O}_7$ (KITPite) structure. The broad arrows (blue) on the Mn atoms represent the magnetic moment directions in the absence of electric or magnetic fields. Small (black) arrows indicate the atomic forces induced by an external magnetic field applied in the \hat{y} direction.	37
4.1.	Structure of ferroelectric hexagonal RMnO_3 or RFeO_3 (6 f.u. per primitive cell). (a) Side view from $[110]$. (b) Plan view from $[001]$; dashed (solid) triangle indicates three Mn^{3+} or Fe^{3+} connected via Op_1 to form a triangular sublattice at $z = 0$ ($z = 1/2$).	48
4.2.	Magnetic phases of hexagonal RMnO_3 and RFeO_3 . Mn^{3+} or Fe^{3+} ions form triangular sublattices at $z = 0$ (dash line) and $z = 1/2$ (solid line). (a) A_2 phase with magnetic symmetry $\text{P6}_3\text{c}'\text{m}'$; spins on a given Mn^{3+} layer point all in or all out. (b) A_1 phase with the magnetic symmetry $\text{P6}_3\text{cm}$, with Mn^{3+} spins pointing tangentially to form a vortex pattern. The A_1 and A_2 phases differ by a 90° global rotation of spins. The B_1 and B_2 phases can be obtained from A_2 and A_1 by reversing the spins on the dashed triangles.	49
4.3.	Transverse ME couplings α_{xx} for A_2 phase RMnO_3 and LuFeO_3 , and α_{yx} for A_1 phase HoMnO_3 . (a) Spin-lattice; (b) spin-electronic; and (c) total spin couplings. The unit is ps/m.	59

5.1.	Structures of (a) a cubic perovskite ABO_3 and (b) a double perovskite $A_2BB'O_6$	63
5.2.	Structure of corundum derivatives. The unit cell in the rhombohedral setting is shown at the left; an enlarged hexagonal-setting view is shown at right. The cations α , β , γ , and δ are all identical in the X_2O_3 corundum structure. For the LNO-type ABO_3 , $\beta = \delta = A$, $\alpha = \gamma = B$; for the ilmenite ABO_3 , $\beta = \gamma = A$, $\alpha = \delta = B$; for the ordered-LNO $A_2BB'O_6$, $\beta = \delta = A$, $\gamma = B$, $\alpha = B'$; for the ordered-ilmenite $A_2BB'O_6$, $\beta = \gamma = A$, $\delta = B$, $\alpha = B'$. At left, ξ_1 (or ξ_2) is the distance between β (or δ) and the oxygen plane that it penetrates during the polarization reversal.	65
5.3.	Movements of A cations in LNO-type (red, here $LiNbO_3$) and ordered-LNO (blue, here Mn_2FeWO_6) corundum derivatives along the polarization reversal path. ξ_1 and ξ_2 are the distances from A atoms to the oxygen planes that are penetrated during the polarization reversal, here rescaled to a range between -1 and 1 . The symmetry at an arbitrary (ξ_1, ξ_2) point is $R\bar{3}$; on the $\xi_1 = \xi_2$ and $\xi_1 = -\xi_2$ diagonals it is raised to $R3c$ and $R\bar{3}$, respectively; and at the origin ($\xi_1 = \xi_2 = 0$) it reaches $R\bar{3}c$. Green diamonds denote the midpoint structure in the parameter space. In the LNO-type case “path1” and “path2” (filled and open red square symbols) are equivalent and equally probable, while the ordered-LNO system deterministically follows “path1” (full blue line), which becomes “path2” (dashed blue) under a relabeling $\xi_1 \leftrightarrow \xi_2$	74
5.4.	Structural evolution along the polarization reversal path of LNO-type and ordered-LNO corundum derivatives. “Before” and “After” are the initial and final structures on the reversal path with symmetry $R3c$ for the LNO-type and $R\bar{3}$ for the ordered-LNO corundum derivatives; “Midpoint” denotes the structure halfway between these and exhibits $R\bar{3}$ structural symmetry in both cases.	75

5.5. Polarization reversal energy profile for LiNbO_3 , LiTaO_3 , Mn_2FeWO_6 , $\text{Zn}_2\text{FeOsO}_6$, and $\text{Li}_2\text{ZrTeO}_6$	76
5.6. Empirical proportionality between the coherent FE energy barrier and P_S^2 . The red curve is the fitting polynomial $E_{\text{barrier}} = (\mu/2)P_S^2$, with $\mu/2 = 0.057 \text{ meVcm}^4/\mu\text{C}^2$	79
5.7. Empirical correlation between the spontaneous polarization and the reaction coordinate ξ in the ground state. The red curve is the fitting polynomial $P_S = m\xi_S + n\xi_S^3$ with $m = 13.3 \times 10^8 \mu\text{C}/\text{cm}^3$ and $n = 19.0 \times 10^{24} \mu\text{C}/\text{cm}^5$	79
5.8. Energy profile and bandgap at the polarization reversal path of FeTiO_3 . The band gap is 1.56 eV and 0.98 eV at points a and c, but FeTiO_3 is conducting at point b.	80
5.9. PDOS of FeTiO_3 at point (a), (b), and (c) along the coherent reversal path. Position of Fermi energy are indicated by dashed black lines. The density of states from two spin channels are represented by the positive branch and negative branch of density of states, respectively. The unit a.u. means arbitrary unit.	81
5.10. Sketch of energy levels of d orbital in the (a) insulating case and (b) the conducting case.	81
5.11. M-H relation (between -14 and 14 T) of Mn_2FeWO_6 at 2, 70, 120, and 400 K, taken from Ref. [44].	82
6.1. FE domains and domain walls observed in (a) LiNbO_3 , taken from Ref. [132] and (b) YMnO_3 , taken from Ref. [133]	88
6.2. Structure of LNO-type corundum derivative ABO_3 when $B' = B$, and ordered-LNO corundum derivative $A_2BB'O_6$. (a) Side view of the rhombohedral unit cell. ξ_1 (or ξ_2) is the vertical distance between an A cation and the oxygen plane that it penetrates during the polarization reversal. (b) Top view of the AB layer and (c) side view in the enlarged hexagonal-setting cell. The enlarged hexagonal cell consists of three columns of octahedra C1, C2, and C3.	90

- 6.3. Illustration of domains and DWs in chiral polar object. Left and right hands represent left (L) and right (R) chirality, and the direction in which the fingers point (\uparrow or \downarrow) represents the polarization direction. (a) Left and right chirality are related by a mirror symmetry. (b) Upward right hand ($R\uparrow$) and downward left hand ($L\downarrow$) are related by the inversion symmetry. (c) FE domains and DWs formed by ($R\uparrow$) domains and ($L\downarrow$) domains. The DW between adjacent thumbs represents $DW_{\uparrow\downarrow}$ and the DW between adjacent little fingers represents $DW_{\downarrow\uparrow}$ 91
- 6.4. Structures of X-wall in the 6+6 supercell and Y-wall in the 4+4 supercell. (a)(d) Top views of the X-wall and Y-wall. The number in each octahedron is the unit cell label. The X-wall is in the x - z or $(01\bar{1}0)$ plane and is located between the 6th and the 7th unit cell, shown by the dashed line. The Y-wall is in the y - z or $(2\bar{1}\bar{1}0)$ plane and is located between the 4th and the 5th unit cell. (b)(e) Side views of the X-wall and Y-wall. Odd-number cells are behind even-number cells in the X-wall. (c)(f) The $\xi_1 + \xi_2$ displacement profile of X-wall and Y-wall. (d) C1, C2, and C3 are three different columns of octahedra in the left-side domain. $\overline{C1}$ and $\overline{C3}$ are columns of octahedra in the right-side domain. The column C1 becomes $\overline{C1}$ after the polarization reversal. 93
- 6.5. Two possible magnetic orders at FE DWs in Mn_3WO_6 . The structure in the center has polarization and magnetization $(+P,+M)$ with the magnetic order udu . The structures on the left and right both have polarization $-P$ but the left one has the magnetic order dud while the right one is udu . In case 1, the FE DW is formed between structures in the center and on the right. In case 2, the FE DW is formed by the central and leftward structures. 95

6.6.	Exchange-interaction map of magnetic cations in Mn_3WO_6 (a) between C1, C2, and C3 columns of octahedra in the bulk structure, and (b) between $\overline{\text{C1}}$, C2, and $\overline{\text{C3}}$ columns of octahedra at the DW structure. The blue, red, and green lines represent the face-sharing, edge-sharing, and corner-sharing magnetic neighbors.	97
6.7.	Illustrations of DW motions in 4+4 and 3+4 supercells. The upward and downward arrows represent the polarization in each unit cell. The dashed blue line represents the $\text{DW}_{\downarrow\uparrow}$ and the solid green line is the $\text{DW}_{\uparrow\downarrow}$. The filled black arrows represent the polarization that are reversed during the DW motion.	99
6.8.	DW-mediated FE reversal in corundum derivatives. (a) Energy profiles of the DW reversal for selected corundum derivatives. The results of both the $\text{DW}_{\downarrow\uparrow}$ and $\text{DW}_{\uparrow\downarrow}$ are included for $\text{Li}_2\text{ZrTeO}_6$. The unit of energy is meV per unit cell. (b) Energy profile of the DW reversal in LiTaO_3 and the evolution of ξ_1 and ξ_2 . The dashed brown lines highlight the position when $\xi_1 = 0$ and $\xi_2 = 0$	100
6.9.	BVS of A cations <i>versus</i> DW-mediated reversal barriers. The linear fitting parameters are $a = 147 \text{ meV}$ and $b = 1650 \text{ meV}$ for $y = a + b(x - 1)$.102	

Chapter 1

Introduction

1.1 Motivations

Time-reversal symmetry means a system looks exactly the same if the flow of time is reversed ($t \mapsto -t$). Magnetization is time-reversal odd, since it can be produced by an electric current, which is odd in time. The spontaneous breaking of time-reversal symmetry in matter leads to the appearance of a ferromagnetic order. The earliest observation of ferromagnetic behavior is from the natural magnet lodestones, which can date back to 6th century BC in Greece and 4th century BC in China. From the early use in compasses for navigation to the modern application to magnetic storage in hard drives and the giant magnetoresistance effect in magnetic sensors, our lives have been greatly improved by the applications of magnetization. However, a magnetic field, which is the conjugate field of magnetization, is difficult to apply compared with an electric voltage.

Spatial-inversion symmetry means a system looks exactly the same if the position is reversed ($\mathbf{r} \mapsto -\mathbf{r}$). Since the polarization can be written as $e\mathbf{r}$, the spontaneous breaking of spatial-inversion symmetry in matter may result in the appearance of a ferroelectric order. Although the discovery of ferroelectrics was in 1920 [1], which is much later than the discovery of natural magnets, the applications of ferroelectrics are in every corner of our lives. For example, ferroelectrics can be used as memory devices, such as ferroelectric RAM. In addition, since ferroelectrics are sensitive to the change of pressure and temperature, they are used as sensors in many applications, such as medical ultrasound devices, fire sensors, and vibration sensors. Moreover, there is also the possibility to achieve the giant electroresistance switching effect in ferroelectric tunnel junctions. However, the application of ferroelectrics is also faced with many obstacles.

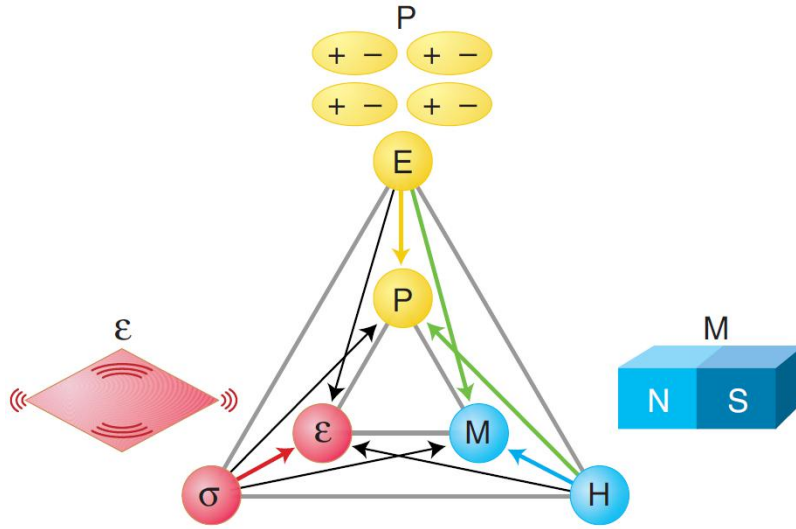


Figure 1.1: The cross coupling between polarization, magnetization, and strain. The electric field \mathbf{E} , magnetic field \mathbf{H} , and stress $\boldsymbol{\sigma}$ control the electric polarization \mathbf{P} , magnetization \mathbf{M} , and strain $\boldsymbol{\varepsilon}$, respectively. This figure is taken from [2].

Firstly, the extensively use of lead based materials such as PZT ($\text{PbZr}_x\text{Ti}_{1-x}\text{O}_3$) in sensors causes environmental problems because of the toxicity of lead and its compounds. Therefore, the discovery of more lead-free ferroelectrics is an urgent task. Secondly, the voltage control of electric polarization, which is accompanied by a current flow, cannot avoid the generation of heat by electron scattering.

If the magnetization can be controlled by an electric field, then the difficulties with generating a large magnetic field and the problems with heat generations are all solved. Such a cross-coupling between magnetization and polarization is called the magnetoelectric effect. As the strain can also couple with the polarization and magnetization, various cross-couplings can also be achieved as shown in Fig. 1.1. Such couplings include the rich interplays between charge, lattice, spin, and orbital orders. In this thesis, our motivation is to understand the interplay between the lattice and spin degrees of freedom in the magnetoelectric effects and in novel lead-free ferroelectrics.

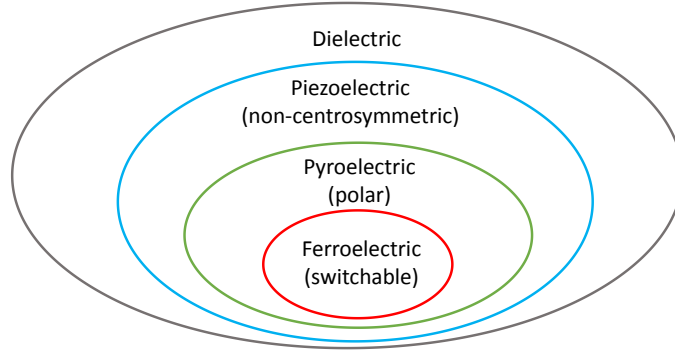


Figure 1.2: Relationship between dielectric, piezoelectric, pyroelectric and ferroelectric.

1.2 Ferroelectricity

1.2.1 General properties

In ordinary insulating materials, polarization \mathbf{P} is linearly induced by an external electric field \mathcal{E} , as shown in Fig. 1.3(a). However, if inversion symmetry is absent in the crystal, polarization can also be induced by a mechanical stress. This effect is called piezoelectricity and it is allowed in all non-centrosymmetric point groups except the cubic point group 432 in Hermann-Mauguin notation whose high symmetry enforces the piezoelectric tensor to be zero. If the piezoelectric material not only breaks the inversion symmetry but also has a unique polar axis, a nonzero polarization exists even without an external field, and the polarization is called “spontaneous polarization” with symbol P_S . In such materials, the polarization changes with temperature, and therefore these materials are called pyroelectrics. Of the 32 crystallographic point groups, the 10 polar point groups 6mm, 6, 3m, 3, 4mm, 4, mm2, m, 2, and 1 allow pyroelectricity. Pyroelectric materials have multiple symmetry-equivalent structures that have the same polarization magnitude but pointing at different directions that are related by symmetry operations. If the material is able to switch reversibly between these states in an applied electric field, this material is ferroelectric (FE) [3]. The relationship between dielectric, piezoelectric, pyroelectric, and ferroelectric is summarized in Fig. 1.2.

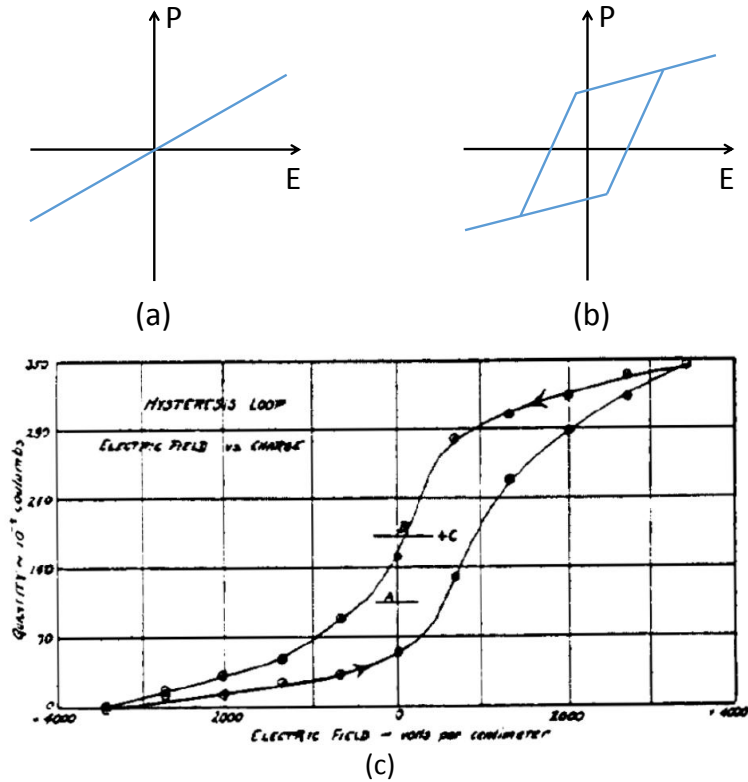


Figure 1.3: Sketch of \mathbf{P} - \mathcal{E} relation of (a) a dielectric and (b) a FE. (c) The first FE hysteresis loop of rochelle salt taken from Ref. [1].

Ferroelectricity was first discovered in 1920 by Valasek [1] when he observed the non-linear ferroelectric hysteresis loop in Rochelle salt ($\text{KNaC}_4\text{H}_4\text{O}_6 \cdot 4\text{H}_2\text{O}$), as sketched in Fig. 1.3(b). Ferroelectricity shares similarities with ferromagnetism, as both have polarization-field hysteresis loops and large susceptibilities. Therefore, the effect got the same prefix “ferro” as ferromagnetism, meaning iron, even though most FEs do not contain iron. On the other hand, the microscopic origins of ferroelectricity and ferromagnetism are radically different.

FEs exhibit many physical properties that are both interesting for fundamental research and industrial applications. The hysteresis effect can be used for energy storage and non-volatile memory devices [4]. FEs also exhibit high and tunable electric permittivity, which can be used in capacitors to increase the capacitance and reduce the size of devices. In addition, FEs are simultaneously piezoelectric and pyroelectric. These

combined properties make FEs ideal for electric, mechanical and thermal sensors. Recently, research on multiferroics, in which FE and ferromagnetic orders coexist in the same material, has further extended the range of application of ferroelectrics [5, 6, 7, 8].

1.2.2 Ferroelectric phase transition

Above the Curie temperature T_c , a FE loses spontaneous polarization and becomes a paraelectric (PE) after which the inversion symmetry is restored. The PE-FE transition is usually a second-order phase transition where the polarization evolves continuously as a function of temperature, and it is captured by the phenomenological Landau-Ginzburg-Devonshire theory as explained below. In a simple model, the Helmholtz free energy density \mathcal{F} of a FE can be expanded in terms of polarization P , which is the order parameter, as

$$\mathcal{F}(P) = \frac{1}{2}a_0(T - T_c)P^2 + \frac{1}{4}bP^4 - \mathcal{E}P, \quad (1.1)$$

where $a_0 > 0$ and $b < 0$. Here we choose the origin of energy for the unpolarized crystal to be zero. When the external electric field is absent ($\mathcal{E} = 0$), the free energy is symmetric with respect to P , as illustrated in Fig. 1.4(a). At $T > T_c$, the free energy has only one minimum at $P = 0$, which represents the PE phase. At $T < T_c$, the free energy has a double-well shape with two minima at polarization $\pm P_S$, which corresponds to the FE phase, and the spontaneous polarization is $P_S = \sqrt{a_0(T_c - T)/b}$.

When an external electric field is present ($\mathcal{E} \neq 0$), the free energy is no longer symmetric about P . The two minima at $T < T_c$ are not equivalent in energy, as illustrate in Fig. 1.4(b), and for large enough electric field, only one minimum survives. The equation of states is give by setting

$$\frac{\partial \mathcal{F}}{\partial P} = a_0(T - T_c)P + bP^3 - \mathcal{E} = 0, \quad (1.2)$$

which gives the the evolution of polarization as a function of electric field, as shown in Fig. 1.4(c). In the PE phase ($T > T_c$), polarization changes monotonically with respect to the electric field, and no spontaneous polarization is present at $\mathcal{E} = 0$. In the FE phase ($T < T_c$), $\mathcal{E} = 0$ corresponds to three distinct states, two stable states at

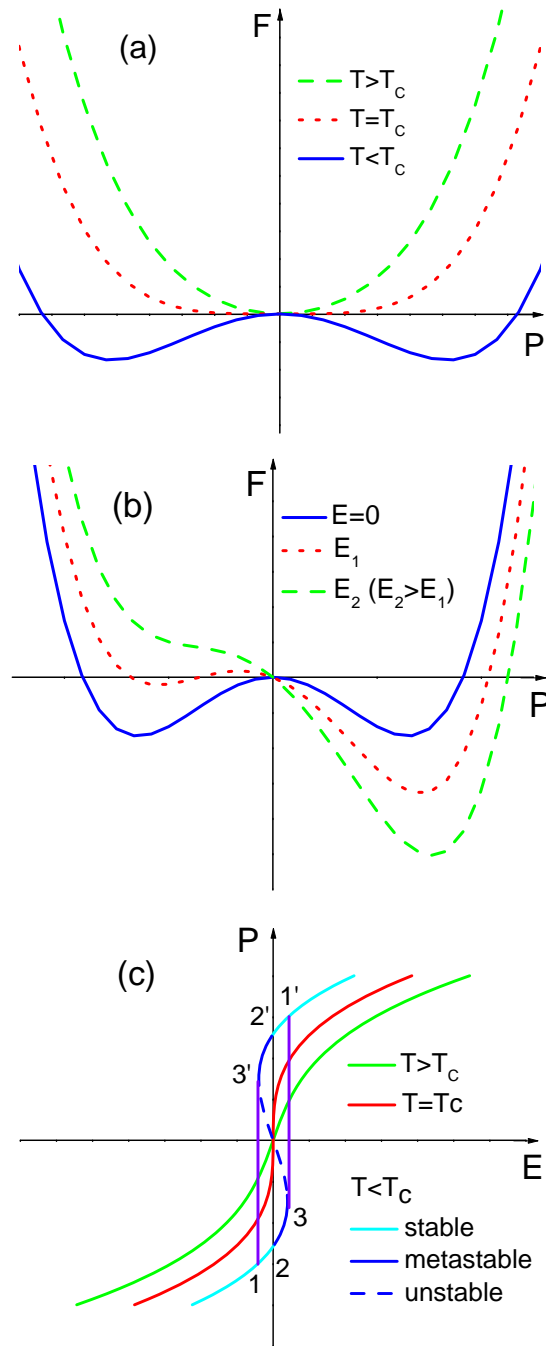


Figure 1.4: PE-FE phase transition described by the Landau-Ginzburg-Devonshire theory. (a) Free energy as a function of polarization in the vicinity of T_c in the absence of an external electric field. (b) Free energy as a function of polarization in the FE phase at various electric fields. (c) Evolution of polarization as a function of an external electric field at various temperatures. Hysteresis loop 1-2-3-1'-2'-3' is observed in the FE phase.

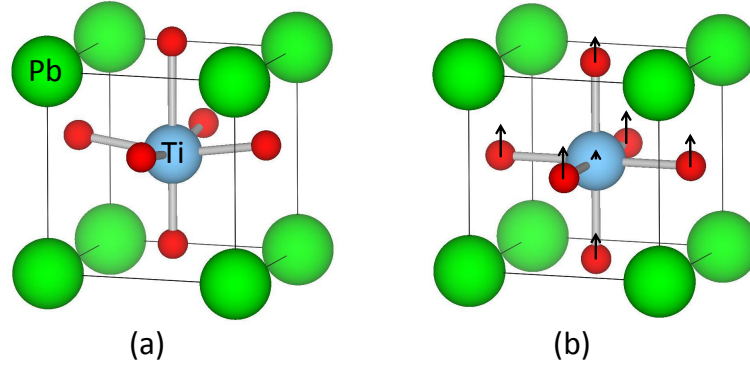


Figure 1.5: The FE structure (a) and the centrosymmetric reference structure (b) of PbTiO_3 . The arrow in (b) represent the magnitude of the atomic displacement in the unstable polar mode, where the position of Pb cation is fixed as the origin.

polarization $\pm P_S$ and one unstable state at $P = 0$. The solid blue regions 2-3 or 2'-3' in Fig. 1.4(c) refer to metastable states, which are also represented by the shallow well on the left side at $\mathcal{E} = \mathcal{E}_1$ in Fig. 1.4(b). The states in dashed blue segment 3-3' are unstable since $\partial^2 \mathcal{F} / \partial P^2 < 0$. Therefore, the polarization jumps from 3 to 1' or from 3' to 1 as shown by the dashed purple line in Fig. 1.4(c), and the loop 1-2-3-1'-2'-3' is the FE hysteresis loop.

1.2.3 Soft modes and boundary conditions

From a microscopic point of view, the PE-FE phase transition is driven by a soft polar mode of the PE structure with an imaginary frequency. Even for materials that do not have a PE phase, i.e. the material melts before the phase transition, the FE states can still be described by a polar distortion from a centrosymmetric reference structure. Meanwhile, the reference structure is often regarded as the barrier structure for FE polarization switching.

Here we illustrate the soft mode theory through the example of the perovskite PbTiO_3 . Perovskite PbTiO_3 is a ferroelectric with tetragonal symmetry in the ground state at zero temperature as shown in the Fig 1.5(a). The centrosymmetric reference structure, which is also the paraelectric structure, is of cubic symmetry with the Ti cation in the center of the cell as shown in Fig 1.5(b). Because of the electron cloud

hybridization between Ti d , Pb s and O p orbitals, there is an unstable transverse optical (TO) polar mode at the Brillouin-zone center in the reference structure at $T = 0\text{K}$, and therefore the ground state is ferroelectric. The soft mode involves the relative displacement between cations and anions, and their relative amplitudes are sketched in Fig 1.5(b). This soft mode get harder as temperature increases and becomes stable above the Curie temperature, which means that the PE structure is stable. Therefore, this soft mode is responsible for the PE-FE transition.

A reference structure with an unstable polar mode is essential for the existence of a ferroelectric state, but whether the phonon mode is a TO mode or a longitudinal optical (LO) mode is closely related to the experimental setup and boundary conditions. In polar materials, because the LO mode oscillates parallel to the electric field, it experiences an additional restoring force from the \mathcal{E} field compared to the TO mode which vibrates perpendicular to the field. Therefore, the frequency of the LO mode is higher than that of the TO mode, and this leads to the famous LO-TO splitting at the Brillouin zone center. In the $\mathbf{q} \rightarrow 0$ limit, the dynamical matrix D is split into an analytical part and a non-analytical part, and the direction-dependent non-analytical (NA) contribution is given by [9, 10]

$$D_{s\alpha,t\beta}^{\text{NA}} = (M_s M_t)^{-1/2} \frac{e^2}{\epsilon_0 \Omega} \frac{(\mathbf{q} \cdot \mathbf{Z}_s)_\alpha (\mathbf{q} \cdot \mathbf{Z}_t)_\beta}{\mathbf{q} \cdot \epsilon^\infty \cdot \mathbf{q}}, \quad (1.3)$$

where ϵ_0 is the vacuum permittivity and ϵ^∞ is the dimensionless relative permittivity from the frozen-ion contribution. Here s and t are sublattice indices, while α and β label the Cartesian direction. Then, M_s , u_s and Z_s are the mass, displacement and Born effective charge tensor of atom s , where the Born charge tensor is defined by $Z_s = \partial \mathbf{P} / \partial \mathbf{u}_s$. The NA part corresponds to the $1/r^3$ behavior in real space, which represents the long-range dipole-dipole interaction. Therefore, the frequencies of the TO modes are determined only by the analytical part of the dynamical matrix, while both parts are needed to determine the LO modes.

In most experiments, FEs are in contact with metallic electrodes with an experimental setup similar to the sketch shown in Fig. 1.6(a). Since the surface bound charges are

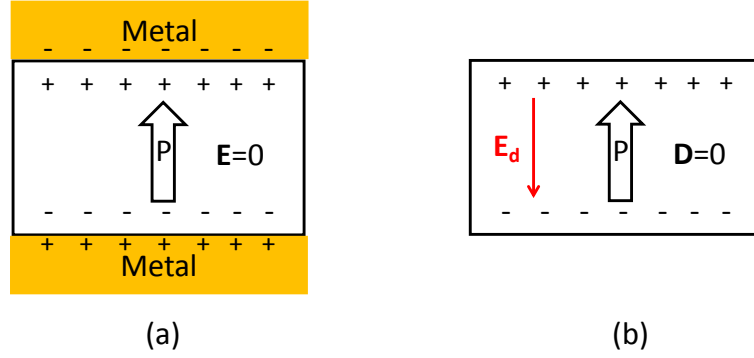


Figure 1.6: (a) $\mathcal{E} = 0$ and (b) $\mathbf{D} = 0$ boundary conditions for FEs.

screened by free electrons in metals, the macroscopic electric field is absent in the sample, which corresponds to the $\mathcal{E} = 0$ boundary condition. In this case, the unstable TO mode determines the FE instability. However, if the sample is isolated in an insulating environment where free charges are not available, as sketched in Fig. 1.6(b), the boundary condition is $\mathbf{D} = 0$, and the surface bound charges in FEs generate a depolarization field \mathcal{E}_d . In this situation, the LO mode frequency determines the ferroelectricity. For a normal FE that has an unstable TO mode, because of the LO-TO splitting, the LO mode is stable. Therefore, polarization does not survive in the depolarization field at $\mathbf{D} = 0$ boundary condition. However, if the FE not only has an unstable TO mode, but also the corresponding LO mode is unstable, polarization persists in the depolarization field. This type of material is called hyperferroelectric. Hyperferroelectricity is theoretically predicted in the hexagonal *ABC* semiconducting FE family [11] but the synthesis of these *ABC* compounds in laboratory is still an on-going problem.

1.2.4 Beyond the soft-mode ferroelectricity

The phenomenological theory and the soft mode theory introduced previously both regard the polar distortion as the driving force for ferroelectricity, and they are an accurate descriptions of most proper FEs, such as PbTiO_3 . However, there are also mechanisms that beyond these descriptions. For example, ferroelectricity can be driven by charge ordering in materials containing ions of mixed valence [12, 13].

Another example is the order-disorder FE. In an order-disorder FE, there is already a dipole moment in each unit cell in the high-temperature PE phase, but the dipole moments are pointing in random directions so that the structure is still centrosymmetric. Upon lowering the temperature and going through the PE-FE phase transition, the dipoles order and all point in the same direction within a domain. Such an order-disorder picture explains the ferroelectricity in the hydrogen-bonded system [14].

There are also FEs for which the primary order parameter is not the polar distortion but another type of phase change, like magnetic ordering or a non-polar structural change. The polar distortion is only a secondary order parameter that is driven by the primary order parameter. This type of material is called an improper FE. One example of an improper FE is hexagonal YMnO₃ [15]. The structure of hexagonal YMnO₃ is shown in Fig. 4.1. The primary order parameter is a non-polar mode at the zone boundary, which is caused by the size mismatch between the Y cation and the MnO₅ bipyramid. Polarization is developed due to the coupling between the zone-boundary mode and zone-center polar mode. Another example is the spin-driven ferroelectricity in TbMnO₃ [16]. At a magnetic phase transition, the emergence of spin spiral breaks inversion symmetry and as a result induces polarization through spin-orbit coupling.

1.3 Magnetolectricity and multiferroicity

1.3.1 Brief history

The magnetolectric (ME) effect is the phenomenon of inducing magnetic (electric) polarization by applying an external electric (magnetic) field in matter. In 1894, Curie pointed out the possibility of ME behavior of crystals in his paper “On symmetry in physical phenomena” [17]. However, it was not until the late 1950s that, along with the development of the magnetic point group [18], Landau and Lifshitz realized that the ME response is only allowed in media without time reversal symmetry and spatial inversion symmetry [19].

Phenomenologically, the Gibbs free energy density \mathcal{G} of a ME material can be written in terms of the electric field $\boldsymbol{\mathcal{E}}$ and the magnetic field \mathbf{H} around the zero-field energy

\mathcal{G}_0 as

$$\begin{aligned} \mathcal{G}(\boldsymbol{\mathcal{E}}, \mathbf{H}) = & \mathcal{G}_0 - \frac{1}{2}\epsilon_0\epsilon_{ij}\mathcal{E}_i\mathcal{E}_j - \frac{1}{2}\mu_0\mu_{ij}H_iH_j - \alpha_{ij}\mathcal{E}_iH_j \\ & - \frac{1}{2}\beta_{ijk}\mathcal{E}_iH_jH_k - \frac{1}{2}\gamma_{ijk}H_i\mathcal{E}_j\mathcal{E}_k - \dots \end{aligned} \quad (1.4)$$

where i , j and k label Cartesian directions and summation over repeated indices is assumed in all the equations. Here ϵ_0 and μ_0 are the permittivity and permeability of vacuum, ϵ and μ are the dimensionless relative dielectric constant and relative permeability. The second-order tensor α corresponds to the linear ME response defined as

$$\alpha_{ij} = \left. \frac{\partial P_i}{\partial H_j} \right|_{\boldsymbol{\mathcal{E}}} = \mu_0 \left. \frac{\partial M_j}{\partial \mathcal{E}_i} \right|_{\mathbf{H}}, \quad (1.5)$$

while the third-order tensor β and γ describe higher order effects. For the linear ME effect in Eq. (1.5), as \mathbf{P} and $\boldsymbol{\mathcal{E}}$ flip signs under spatial inversion $\bar{1}$, while \mathbf{M} and \mathbf{H} reverse directions under time reversal $1'$, the linear ME effect exists only in materials without time-reversal and spatial-inversion symmetries. According to Neumann's principle that any physical properties should be invariant with respect to crystal symmetry operations [20], 58 of the 122 magnetic point groups allow the linear ME effect [21].

In 1960, Dzyaloshinskii proposed the first ME crystal Cr_2O_3 with linear ME effect based on its magnetic symmetry [22]. The prediction was shortly proved by experiments through measuring the magnetization induced by an electric field [23, 24] and the polarization induced by a magnetic field [25, 26]. The successful observation of the ME effect in Cr_2O_3 triggered intense research interests in the field for the possibility of achieving the cross coupling between electric and magnetic properties. At the same period of time, the search for multiferroics, materials that exhibit more than one primary ferroic order parameter simultaneously, also began. In 1961, Smolenskii and Ioffe suggested to introduce magnetic ions into FE perovskites to create solid solutions hosting both long-range magnetic order without losing the FE order [27]. Later on, the multiferroicity was discovered in boracites, such as $\text{Ni}_3\text{B}_7\text{O}_{13}\text{I}$, without doping [28]. Because the ME coupling in a single-phase crystal is thermodynamically bounded by $\alpha_{ij} \leq \sqrt{\epsilon_{ii}\mu_{jj}}$ [29], multiferroics have a much higher upper limit and therefore have the potential to exhibit huge ME effect. After decades of effort, many ME single crystals

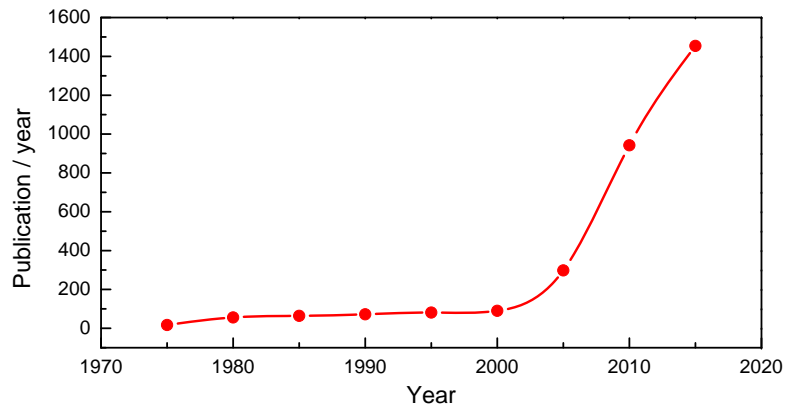


Figure 1.7: Publication per year with keyword “magnetolectric” according to the *Web of Science*

and multiferroics were discovered and some phenomenological theories were proposed [30, 31]. However, the limited understanding of the microscopic origin of the ME effect and multiferroicity impeded the further development of the field.

In the early 2000s, motivated by the question of “Why Are There so Few Magnetic Ferroelectrics?” [32], new multiferroics materials, such as BiFeO_3 [33] and orthorhombic TbMnO_3 [16] were discovered in experiments with novel ME coupling mechanisms, and the term “multiferroics” was expanded to include antiferromagnetism and ferrimagnetism. Since then, there has been a resurgence of research interest in ME effects as shown in Fig. 1.7, and the renaissance has been driven by the development in theory and experiment and their close collaborations. In experiment, the improved growth techniques of high-quality single crystals and thin films provide routes to explore more structures and phases, and identify new mechanisms in ME materials. In theory, with the development of the modern theory of polarization [34], the first-principles electronic structure theory is mature enough for the study and even design of the coupled polarization and magnetization in materials.

The study of magnetoelectricity and multiferroics drives the discovery of novel microscopic mechanisms of coupling between charge and spin. Meanwhile, ME materials and multiferroics exhibit desirable properties for various technological applications. For example, as both the magnetic order and FE order can be used for memory storage,

multiferroics are good candidates for four-state memory devices. Besides, the coupling between magnetic order and FE order makes it possible that a voltage pulse can be used directly to control the magnetic bit without generating electric current and excessive heat.

1.3.2 Mechanisms

There are many mechanisms for multiferroicity because of the variety of origins of ferroelectricity. However, the coexistence of ferroelectricity and ferromagnetism does not guarantee that the two order parameters are strongly coupled. In type-I multiferroics, the microscopic origins of ferroelectricity and ferromagnetism are different, therefore the ME coupling is weak in the bulk. Examples of type-I multiferroics are BiFeO_3 and hexagonal rare-earth manganite $R\text{MnO}_3$ [35]. In contrast, in type-II multiferroics, such as TbMnO_3 , the ferroelectricity is driven by the magnetic ordering which breaks inversion symmetry, and occurs only in the magnetically ordered phase. In general, ME effects also exist in materials without long range order because the space-time reversal symmetry $\bar{1}'$ is compatible with the ME effect but not allowed in multiferroics.

There are several different microscopic mechanisms that can give rise to ME effects, such as the inverse Dzyaloshinskii-Moriya interaction, $p-d$ hybridization, and exchange striction. However, in general, the mechanisms can be divided into two categories based on whether it depends on the presence of the relativistic spin-orbit coupling (SOC) $\lambda_{\text{SOC}} \mathbf{L} \cdot \mathbf{S}$. The ME effect caused by SOC is more significant for elements with large atomic number Z as λ_{SOC} scales roughly as Z^2 [36], while the non-relativistic mechanisms are not limited by the atomic number. In the following, we pick up two mechanisms as examples to demonstrate the microscopic origins of ME coupling.

Starting from the $\lambda_{\text{SOC}} \mathbf{L} \cdot \mathbf{S}$ interaction and considering the hopping between different orbitals, an effective spin interaction that is linear in λ_{SOC} can be extracted with the form

$$\mathcal{H}_{\text{ME}} = \sum_{i,j} \mathbf{D}_{ij} \cdot (\mathbf{S}_i \times \mathbf{S}_j), \quad (1.6)$$

and this is the Dzyaloshinskii-Moriya interaction, which is also called the antisymmetric

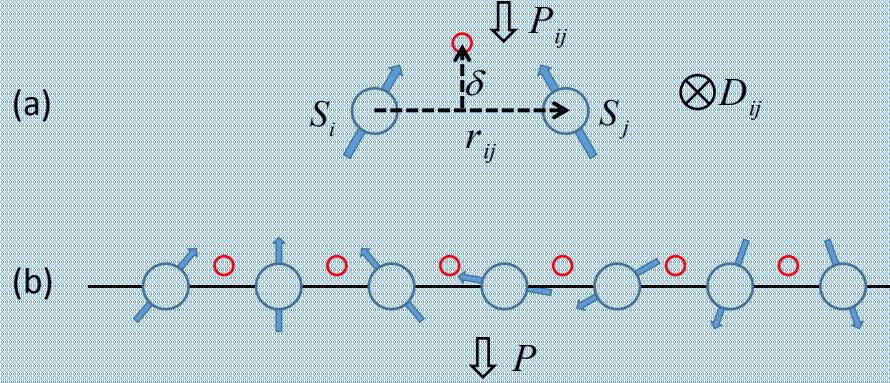


Figure 1.8: Dzyaloshinskii-Moriya interaction. The open red circle represents oxygen ion. The filled blue circle and filled blue arrow are magnetic ion and its spin.

exchange [37, 38]. Here \mathbf{D}_{ij} is the Dzyaloshinskii vector for a pair of spins on magnetic ions i and j mediated by an oxygen ion, as shown in Fig. 1.8(a). The Dzyaloshinskii vector is proportional to the displacement of the oxygen δ from the center of ij bond

$$\mathbf{D}_{ij} \sim \delta \times \mathbf{r}_{ij}, \quad (1.7)$$

where \mathbf{r}_{ij} is the vector pointing from ion i to ion j . This interaction favors non-collinear spins when the cation-anion-cation bond angle deviates away from 180° . Conversely, in a non-collinear magnetic structure, the oxygen ions tend to shift off-center to gain the Dzyaloshinskii-Moriya energy and the off-center movement generates a local electric dipole

$$\mathbf{P}_{ij} \sim \mathbf{r}_{ij} \times (\mathbf{S}_i \times \mathbf{S}_j). \quad (1.8)$$

In a cycloidal spin structure as shown in Fig. 1.8(b), because of this inverse Dzyaloshinskii-Moriya interaction, all the oxygen ions shift at the same direction. Therefore, a macroscopic polarization is coupled to the cycloidal spin structure.

Another mechanism of magnetoelectric coupling is the exchange striction, which is described by the Heisenberg model

$$\mathcal{H}_{\text{ME}} = \sum_{i,j} J_{ij} \mathbf{S}_i \cdot \mathbf{S}_j. \quad (1.9)$$

The exchange integral J depends on the bond length and bond angle of the cation-anion-cation bridge between magnetic cations, therefore it can couple the lattice to the

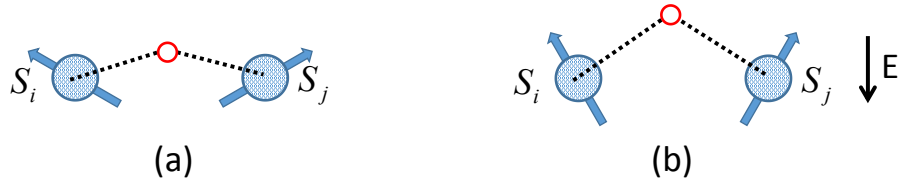


Figure 1.9: Exchange-striction interaction. (a) The cation-anion-cation bond without external fields. (b) The cation-anion-cation bond in the presence of an electric field. The open red circle represents oxygen ion. The filled blue circle and filled blue arrow are magnetic ion and its spin.

magnetic order [39, 40]. For example, if the cation-anion-cation bond angle is close to 180° , $J > 0$ and spins prefer to be antiparallel. If the bond angle is close to 90° , $J < 0$ so that spins prefer to be parallel. This mechanism does not depend on SOC, and it exists both in collinear and non-collinear magnetic orders. In the example illustrated in Fig. 1.9, the oxygen anion shifts away from magnetic cations in an applied electric field, making the bond angle closer to 90° . As a result, the Heisenberg exchange J becomes more negative, leading to spin canting and a change of net magnetic moment.

1.4 Outline of the present work

The rest of this dissertation is organized as follows.

In this thesis, we use first-principles density functional theory to calculate various properties, such as the total energy, polarization, and magnetization, of crystalline materials. In Chapter 2, we give a brief introduction of the computational methods that are used in later chapters. We covers the basic ideas of the density functional theory as well as short descriptions of several parameters that are used in practical calculations. In addition, we also briefly explain the meaning of phonons and normal modes in solids. Furthermore, the concept of bulk polarization in periodic system is explained in more detail as it is the foundation of computational study of the electric polarization.

Using first-principles methods to study ME responses can shed light on microscopic mechanisms that drive ME effects, and it is a powerful tool to predict and even design

new ME materials. The lattice-mediated ME contribution has been studied in several materials, and it has been shown that the lattice contribution is proportional to both the Born dynamical electric charge Z^e and its magnetic analog, the dynamical magnetic charge Z^m . In Chapter 3, we focus on the study of magnetic charge tensors Z^m generated by different mechanisms. Using first-principles density functional methods, we calculate the atomic Z^m tensors in Cr_2O_3 , which has a SOC induced ME effect, and in KITPite, a fictitious material that has previously been reported to show a strong ME response arising from exchange striction effects.

The study of magnetic charges in Chapter 3 sheds light on the mechanisms that may induce large ME effects. Comparing with the SOC mechanism, exchange striction acting on non-collinear spins is a more promising mechanism to generate large dynamical magnetic charges. The hexagonal manganites $R\text{MnO}_3$ and ferrites $R\text{FeO}_3$ ($R = \text{Sc}, \text{Y}, \text{In}, \text{Ho-Lu}$) are found to be good candidates to show such a mechanism. The transition-metal ions in the basal plane are antiferromagnetically coupled through super-exchange so as to form a 120° non-collinear spin arrangement. Therefore, in Chapter 4, we present a theoretical study of magnetic charges and ME responses in these hexagonal manganites and ferrites. Besides, we consider both the lattice-mediated ME effect and the electronic contributed ME effect in order to investigate the importance of each term.

The search for new FEs and FE mechanisms not only expands our understanding of ferroelectricity, but also provides more routes to discover and design multiferroics and ME materials. In Chapter 5, we focus on the theoretical prediction of new FEs. Here we investigate a class of ABO_3 and $A_2BB'O_6$ materials that can be derived from the X_2O_3 corundum structure by mixing two or three ordered cations on the X site. Most such corundum derivatives have polar structures, but it is unclear whether the polarization is reversible, which is a requirement for FEs. Therefore, we discuss the structural criteria for them to be FE and propose a structural constraint method to calculate the coherent FE reversal path in the corundum derivative family. Meanwhile, the versatile corundum derivative structure can also incorporate magnetism which is also worthwhile to investigate.

Although we discuss the coherent FE reversal process in corundum derivatives in

Chapter 5, the hysteresis behavior of FE reversal is caused by the nucleation, expansion or shrinkage of domains through the motion of domain walls in an applied electric field. Meanwhile, FE domain walls have different geometric and electronic structures comparing to the bulk, thus, domain walls may exhibit rich physics that are not present in the bulk. In Chapter 6, we construct supercells with a polarization-up domain and a polarization-down domain to study the structures, orientations, magnetic orders at the FE domain walls in corundum derivatives. In addition, we also use the structural constraint method to investigate the FE domain wall reversal barriers in comparison with the coherent barrier reported in Chapter 5.

In Chapter 7, we summarize our work in Chapter 3, 4, 5, and 6, and point out several promising research directions for future investigation in the field of ferroelectricity and magnetoelectric effects.

The contents of Chapters 3, 4 and 5 are mainly based on a series of papers [41, 42, 43] by Ye and Vanderbilt, and the Ref. [44] by Ye *et al.*

Chapter 2

Computational methods

We learn how to solve the Schrödinger's equation for the hydrogen atom analytically in undergraduate quantum mechanics courses, but most systems, such as molecules, are more complicated than the hydrogen atom and their wavefunctions are solved through numerical methods, such as the exact diagonalization method. As the dynamics of electrons is much faster than that of nuclei, the motion of electrons and nuclei can be treated separately. Therefore, when we consider the electronic structure, the nucleus can be approximated as a fixed potential, which is called the Born-Oppenheimer approximation. In a solid, the number of nuclei and electrons are on the order of 10^{23} . Considering the Coulomb interaction between electrons, it is impossible to solve such a huge many-body problem numerically within the current computational capability. Even if such a problem can be solved by advanced computers in the future, the complexity of the wavefunction would be beyond our understanding, and it would not be directly related to experimental observations.

In this chapter, we briefly introduce the first-principles density functional theory (DFT) [45], which is a widely used method in computational physics, chemistry and material science to solve the above mentioned many-body problem in a solid. We will also explain the meaning of several computation parameters that we will mention in the thesis. In addition, the computational methods for lattice dynamics and the bulk polarization are also briefly summarized in this chapter.

2.1 Density functional theory

2.1.1 Kohn-Sham equations

The foundation of density functional theory is laid on the two Hohenberg-Kohn theorems [46] published in 1964. The first Hohenberg-Koh theorem states that in principles the ground-state electron density $n(\mathbf{r})$ of the many-electron system uniquely determines the external potential $V_{\text{ext}}(\mathbf{r})$, and hence the Hamiltonian of the system. This means that the Hamiltonian can be written as a functional of the ground-state electron density. As a result, the N -electron many-body problem with $3N$ spatial coordinates is reduced to a 3-coordinate problem by using the functional of electron density instead of the many-body wavefunction. The second Hohenberg-Kohn theorem defines a general form of the energy functional and proves that the correct ground state electron density minimizes this energy functional.

One year later, based on the Hohenberg-Kohn theorems, Kohn and Sham formulated the energy functional into a practical form [47]. Their original idea is to map the interacting many-body system into a fictitious non-interaction system, the Kohn-Sham system, that has the same ground-state electron density as the interacting one. The electron density in the Kohn-Sham system is given by

$$n(\mathbf{r}) = \sum_i^{\text{occ}} |\psi_i(\mathbf{r})|^2, \quad (2.1)$$

where ψ_i is the wavefunction of the fictitious system of non-interaction electrons. According to the Hohenberg-Kohn theorems, the non-interacting ψ_i is also a functional of the noninteracting density. Then the density functional of the Kohn-Sham system is given by

$$\begin{aligned} E_{\text{KS}}[n] = & -\frac{\hbar^2}{2m} \sum_i \langle \psi_i | \nabla^2 | \psi_i \rangle + \int V_{\text{ext}}(\mathbf{r}) n(\mathbf{r}) d\mathbf{r} \\ & + \frac{e^2}{2} \int \int \frac{n(\mathbf{r}) n(\mathbf{r}')}{|\mathbf{r} - \mathbf{r}'|} d\mathbf{r} d\mathbf{r}' + E_{\text{xc}}[n(\mathbf{r})]. \end{aligned} \quad (2.2)$$

The density that minimizes Eq. (2.2) is the ground-state density, and the corresponding energy is the ground-state energy. In Eq. (2.2), the first term is the kinetic energy of non-interacting electrons and the second term is the potential energy of electrons in

the external field created by the nuclei. The effective field for the electron-electron interaction is contained in the third and fourth terms. The third term is the so-called Hartree energy, describing the classical electron-electron Coulomb repulsion. The fourth term, which includes all the many-body interactions, is called the exchange-correlation functional (see the next subsection for more details).

The Kohn-Sham wavefunction can be obtained by applying the variational principles $\delta E_{\text{KS}}/\delta\psi_i = 0$ to Eq. (2.2) with the orthogonality condition that $\langle\psi_i|\psi_j\rangle = \delta_{ij}$. The resulting Kohn-Sham equations are

$$\left[-\frac{\hbar^2}{2m}\nabla^2 + \int \frac{e^2 n(\mathbf{r}')}{|\mathbf{r}-\mathbf{r}'|} d\mathbf{r}' + V_{\text{ext}}(\mathbf{r}) + V_{\text{xc}}[n(\mathbf{r})]\right]|\psi_i\rangle = \epsilon_i|\psi_i\rangle. \quad (2.3)$$

Here the exchange-correlation potential V_{xc} is given by

$$V_{\text{xc}}[n(\mathbf{r})] = \frac{\delta E_{\text{xc}}[n(\mathbf{r})]}{\delta n(\mathbf{r})}. \quad (2.4)$$

If the explicit expression of $V_{\text{xc}}[n(\mathbf{r})]$ is known, the Kohn-Sham equations can be solved self-consistently and ϵ_i is the i th eigenvalue. The ground-state energy of the system given by Eq. (2.2) is then

$$E_0 = \sum_i \epsilon_i - \frac{e^2}{2} \int \int \frac{n(\mathbf{r})n(\mathbf{r}')}{|\mathbf{r}-\mathbf{r}'|} d\mathbf{r}d\mathbf{r}' + E_{\text{xc}}[n(\mathbf{r})] - \int V_{\text{xc}}[n(\mathbf{r})][n(\mathbf{r})] d\mathbf{r}. \quad (2.5)$$

2.1.2 Exchange-correlation functionals

Unfortunately, the Hohenberg-Kohn theorems only give an existence proof of the density functional but did not give any hint on how to obtain the exact form of the exchange-correlation functional. Therefore, different approximations of the exchange-correlation functional have been developed for practical calculations. One of the most commonly used functional is the local-density approximation (LDA) proposed in 1981 [48]. The LDA functional depends only on the local density $n(\mathbf{r})$, and it reproduces the exact results of the homogeneous electron gas. However, it fails in situations where the density undergoes rapid changes, such as in molecules. The general gradient approximation (GGA) overcomes this problem by including the density gradient $\nabla n(\mathbf{r})$ in the exchange-correlation functional. GGA is also widely used, and there are different parameterizations of the GGA, such as PW91 [49], PBE [50], and PBEsol [51]. Among

them, PBEsol is a revised PBE GGA that improves equilibrium properties of densely-packed solids and their surfaces. In addition, there are also more advanced functionals such as the hybrid functionals [52], which incorporate a portion of exact exchange from Hartree-Fock theory. In general, DFT is still a mean-field theory, and therefore there are many strongly correlated systems that are beyond the ability of DFT.

2.1.3 On-site Coulomb correction

Both LDA and GGA often fail to describe the magnetic properties of systems with partially filled d and f electron shells due to an underestimation of the on-site Coulomb repulsion on the localized orbitals. Therefore, in the DFT+ U method, additional terms, the on-site Hubbard U and Hund's coupling J , are introduced to improve the performance of DFT for d and f electrons [53, 54]. The Hubbard U is a penalty energy $U \sum_i n_{i\uparrow} n_{i\downarrow}$ if an atomic orbital is occupied by two opposite-spin electrons, and the orbital energy can be written as [55]

$$\epsilon_i = \epsilon_{\text{DFT}} - U(n_i - \frac{1}{2}). \quad (2.6)$$

The eigenvalues of an unoccupied orbital ($n_i = 0$) and an occupied orbital ($n_i = 1$) are differed exactly by the energy U . In addition to the on-site Coulomb repulsion, Hund's rule, which tends to maximize spin and orbital angular momentum, also affects the orbital occupancy. In practical calculations, the parameters U and J are usually adjusted to reach agreement with experimental results, such as the magnetic moment or band gap.

2.1.4 Practical implementations

The Kohn-Sham wavefunction at band n and wave vector \mathbf{k} has the Bloch form $\psi_{n\mathbf{k}}(\mathbf{r}) = e^{i\mathbf{k}\cdot\mathbf{r}} u_{n\mathbf{k}}(\mathbf{r})$, and $u_{n\mathbf{k}}(\mathbf{r})$ has the lattice periodicity. To solve the Kohn-Sham equations numerically, the Kohn-Sham wavefunctions are expanded in a set of basis functions. In many DFT packages, such as VASP [56] and Quantum Espresso [57], the orthogonal plane-wave basis sets are used. The wavefunction is expanded as

$$\psi_{n\mathbf{k}}(\mathbf{r}) = e^{i\mathbf{k}\cdot\mathbf{r}} \sum_{\mathbf{G}} c_{n\mathbf{k}}(\mathbf{G}) e^{i\mathbf{G}\cdot\mathbf{r}} = \sum_{\mathbf{G}} c_{n\mathbf{k}}(\mathbf{G}) e^{i(\mathbf{G}+\mathbf{k})\cdot\mathbf{r}}. \quad (2.7)$$

The accuracy of the expansion is controlled by the number of plane-wave basis states that are in use. In practical calculations, there is a truncation of the plane-wave sequence determined by $|\mathbf{k} + \mathbf{G}| < G_{\text{cut}}$, and the cut-off energy is defined as $E_{\text{cut}} = \frac{\hbar^2}{2m} G_{\text{cut}}^2$.

As the Coulomb potential close to the nucleus core is very deep, $\propto -\frac{1}{r}$, wavefunctions oscillate rapidly in the core, which requires a very large plane-wave basis set to describe. This type of all-electron calculation is accurate but also very time consuming. However, most physical properties are determined by the valence states and are insensitive to the core environment. Therefore, the core environment can be replaced by a shallow pseudopotential that is constructed to reproduce the same valence eigenstates outside a chosen core cut-off radius [58]. The pseudopotential method greatly reduces the plane-wave basis sets and the computational cost, and it is widely used in practical calculations. There are many different methods to construct pseudopotentials, and the most commonly used ones are the norm-conserving [59], ultrasoft [60], and PAW [61] pseudopotentials.

The Kohn-Sham wavefunction is solved at each wave vector \mathbf{k} in Eq. (2.3), and the physical properties, such as the ground-state energy, are obtained by integrating over all the wave vectors in the Brillouin zone. In practical calculations, the integral is replaced by a summation over a finite set of k points, and commonly, an equally-spaced k -mesh is used to sample the Brillouin zone. As the size of Brillouin zone is inversely proportional to the size of the real-space unit cell, the k -mesh should be more dense for smaller unit cells.

2.2 Phonons

Phonons are collective vibrations of atoms at certain frequencies in a solid, and the oscillation mode is called the normal mode. The normal modes are determined by the mass matrix $M_{i\alpha,j\beta} = \sqrt{M_i M_j}$ and the force-constant matrix

$$K_{i\alpha,j\beta} = \frac{\partial^2 E}{\partial u_{i\alpha} \partial u_{j\beta}}, \quad (2.8)$$

which is the second derivative of the total energy with respect to the displacement u . In the notation, i and j are atomic labels, while α and β indicate the three Cartesian directions. For the phonon with oscillation mode $\boldsymbol{\eta}(t)$, the force on the mode is $-\mathbf{K}\cdot\boldsymbol{\eta}(t)$. As a result, the equation of motion is expressed as

$$\mathbf{M}\cdot\ddot{\boldsymbol{\eta}}(t) = -\mathbf{K}\cdot\boldsymbol{\eta}(t). \quad (2.9)$$

For the harmonic oscillation $\boldsymbol{\eta}(t) = \boldsymbol{\eta}_0 e^{-i\omega t}$, the above equation becomes

$$(\mathbf{K} - \mathbf{M}\omega^2) \cdot \boldsymbol{\eta}_0 = 0. \quad (2.10)$$

The solutions of Eq. (2.10) are the phonon frequency ω and the normal mode $\boldsymbol{\eta}_0$.

2.3 Modern theory of polarization

The concept of electric polarization is the key to understand ferroelectricity, and the modern theory of polarization provides the conceptual foundation and the numerical tool to study polarization in bulk crystals. Before the development of the modern approach, it was debatable how to understand the microscopic picture of the bulk polarization and calculate it from first principles. The central problem is with the definition of bulk polarization in a periodic crystal. This problem was finally solved in the early 1990s by a series of papers by Resta [62, 63], and King-Smith and Vanderbilt [34], and this development is known as the “modern theory of polarization.” As the bulk polarization is expressed in terms of Berry phase, a geometric phase, this theory is also called “Berry-phase theory of polarization.” Until today, the modern approach has been widely implemented in first-principles calculation packages, and it is the standard method to study the bulk polarization and other dielectric responses in weakly correlated materials.

In this section, we first analyze the failure of several definitions of bulk polarization based on electronic charge density. Then we show how the modern theory of polarization changes our microscopic understanding of the bulk polarization by focusing on the change of polarization. Lastly, we briefly show the key formulas for the modern approach and discuss the physical meaning of the results.

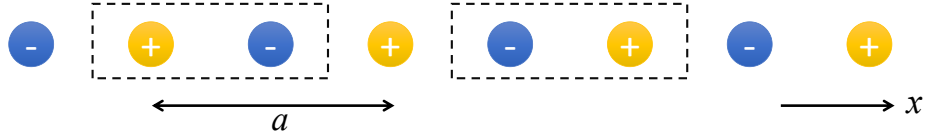


Figure 2.1: A 1D chain of alternating anions and cations. The distance between each anion and cation is $a/2$. The two dashed rectangles indicate two different choices of unit cell.

A classical picture of polarization in bulk crystals is the Clausius-Mossotti (CM) model [64]. Within the CM model, each unit cell provides a localized electric dipole, and the bulk polarization is the superposition of the localized contributions. The problem with the CM model is that the electronic charge density in a crystal has a periodic continuous distribution, so it is ambiguous to partition the charge distribution into localized contributions.

As the local electric dipole picture fails, it is tempting to use the continuous distributed charge density $\rho(\mathbf{r})$ to define the electric dipole in a bulk crystal. One possibility is to define it as the polarization of a macroscopic sample divided by its volume, i.e.,

$$\mathbf{P}_{\text{samp}} = \frac{1}{V_{\text{samp}}} \int_{\text{samp}} d\mathbf{r} \mathbf{r} \rho(\mathbf{r}). \quad (2.11)$$

This definition works well for finite systems such as molecules. However, for a bulk crystal, the above definition cannot distinguish between the polarization from the surface charges and the bulk polarization. Moreover, the surface polarization depends on the specific experimental environment in which the sample is prepared and the surface charge density is difficult to control. Therefore, Eq. (2.11) is not a useful definition for the intrinsic bulk polarization.

Another attempt to remove the surface dipole contribution in the definition is via

$$\mathbf{P}_{\text{cell}} = \frac{1}{V_{\text{cell}}} \int_{\text{cell}} d\mathbf{r} \mathbf{r} \rho(\mathbf{r}), \quad (2.12)$$

where the integral is taken over one unit cell. However, this definition is still ambiguous because the result of Eq. (2.12) depends on the shape and location of the unit cell used

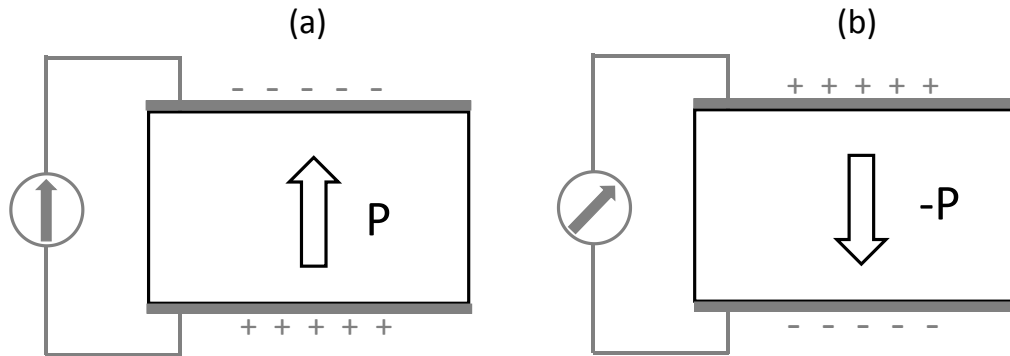


Figure 2.2: An experimental setup to measure the spontaneous polarization in ferroelectric materials. The ferroelectric sample is inserted into a shorted capacitor. Free charges are accumulated on top and bottom of the capacitor to screen out the bulk polarization. When the bulk polarization is reversed from (a) to (b) by an electric field, current flows through the ammeter in the shorted wire to re-screen the bulk polarization.

in the calculation. The ambiguity is clearly demonstrated in the example of a one-dimensional (1D) chain of alternating anions and cations. As shown in Fig. 2.1, the cations and anions are equally spaced with a distance $a/2$ so that the lattice constant is a . In Fig. 2.1, two different choices of unit cell are indicated by the dashed rectangles. The center of the unit cell is the origin in our convention, so the polarization per unit length is $P_L = \frac{1}{a}(-\frac{1}{4}a \times e + \frac{1}{4}a \times (-e)) = -\frac{1}{2}e$ for the left-most unit cell, and $P_R = \frac{1}{a}(-\frac{1}{4}a \times (-e) + \frac{1}{4}a \times e) = \frac{1}{2}e$ for the right-most unit cell. Even though, the two unit cells describe the same 1D chain, two different value of \mathbf{P}_{cell} are obtained. If more choices of unit cell are considered, a series of polarizations can be found, such as $\pm\frac{3}{2}e$, $\pm\frac{5}{2}e$, and they differ by an integer multiple of the charge unit e .

It is also constructive to learn how the polarization is measured in experiment in order to find a practical definition of bulk polarization. A cartoon is depicted in Fig. 2.2 to show the experiment setup where a ferroelectric sample is inserted into a shorted capacitor. In Fig. 2.2(a), the bulk polarization points up and free charges in the metal electrodes are accumulated at the top and bottom surfaces to screen out the polarization bound charges. When a downward electric field is applied, the bulk

polarization reverses direction as shown in Fig. 2.2(b). Meanwhile, the free charges flow through the shorted wire and the ammeter to re-screen the downward bulk polarization. Actually, the experiment measures the current flow \mathbf{j} during the polarization switching, and the accumulated current flow is related to the change of polarization $\Delta\mathbf{P}$ as

$$\Delta\mathbf{P} = \mathbf{P}(\Delta t) - \mathbf{P}(0) = \int_0^{\Delta t} \mathbf{j}(t) dt. \quad (2.13)$$

Then the spontaneous polarization is determined by $\mathbf{P}_S = \Delta\mathbf{P}/2$. Therefore, the spontaneous polarization itself is not directly measured; instead the change of polarization is measured in experiments.

The above discussion shows that the bulk polarization cannot be uniquely defined by the charge density. Instead, it is more meaningful to study the change of polarization, which is related to the adiabatic flow of current. The current-carrying particles are electrons and ions. While the ionic part can be treated classically as point charges, the quantum nature of electrons are essential. Within a quantum-mechanical description, the electron currents are closely related to the phase of the wavefunction, but the phase information is lost in the charge density, which only depends on the modulus of the wavefunction. Therefore, the quantum nature of electrons determines that the bulk polarization cannot be defined by the charge density.

The shift of research focus from polarization and charge density to the change of polarization and adiabatic flows of current laid the important conceptual foundation for the modern theory of polarization. In the next part, the derivation of the central formulas of the modern approach is briefly sketched. The polarization contributed by electrons is written in the form of a Berry phase in the Brillouin zone, and the total polarization is found to be a lattice instead of a single-valued quantity.

We start from a mean field Hamiltonian $H = \frac{p^2}{2m} + V$, such as the Kohn-Sham one, where the self-consistent potential V is periodic. The eigenfunction of the Schrödinger equation $H|\psi_{n\mathbf{k}}\rangle = E_{n\mathbf{k}}|\psi_{n\mathbf{k}}\rangle$ has the Bloch form $\psi_{n\mathbf{k}} = e^{i\mathbf{k}\cdot\mathbf{r}}u_{n\mathbf{k}}(\mathbf{r})$ where $u_{n\mathbf{k}}(\mathbf{r})$ has lattice periodicity. Equivalently, the eigenvalue problem can be rewritten as $H_{\mathbf{k}}|u_{n\mathbf{k}}\rangle = E_{n\mathbf{k}}|u_{n\mathbf{k}}\rangle$, where

$$H_{\mathbf{k}} = \frac{(\mathbf{p} + \hbar\mathbf{k})^2}{2m} + V. \quad (2.14)$$

All the quantities above depend implicitly on a parameter λ which changes slowly in time. For ferroelectric materials, λ can represent the sublattice displacement which drives the system from a centrosymmetric reference structure at $\lambda = 0$ to the ferroelectric ground state structure at $\lambda = 1$. Using the adiabatic perturbation theory, the first-order correction to the wavefunction is

$$|\delta\psi_{n\mathbf{k}}\rangle = -i\hbar\dot{\lambda} \sum_{m \neq n} \frac{\langle\psi_{m\mathbf{k}}|\partial_\lambda\psi_{n\mathbf{k}}\rangle}{E_{n\mathbf{k}} - E_{m\mathbf{k}}} |\psi_{m\mathbf{k}}\rangle. \quad (2.15)$$

Here ∂_λ means the derivative with respect to λ and $\dot{\lambda} = \frac{d\lambda}{dt}$. The change in wavefunction is accompanied by a current flow, and the first-order correction to the current from the n th band is

$$\mathbf{j}_n = \frac{d\mathbf{P}_n}{dt} = \dot{\lambda} \frac{d\mathbf{P}_n}{d\lambda} = \frac{i\hbar e \dot{\lambda}}{(2\pi)^3 m_e} \sum_{m \neq n} \int d\mathbf{k} \frac{\langle\psi_{n\mathbf{k}}|\mathbf{p}|\psi_{m\mathbf{k}}\rangle \langle\psi_{m\mathbf{k}}|\partial_\lambda\psi_{n\mathbf{k}}\rangle}{E_{n\mathbf{k}} - E_{m\mathbf{k}}} + \text{c.c.}, \quad (2.16)$$

where m_e is the mass of electron and c.c. means complex conjugate. The summation in Eq. (2.16) can be removed by using $H_{\mathbf{k}}$ in Eq. (2.14). After some manipulation and eliminating $\dot{\lambda}$ on both sides, the simplified result is

$$\frac{d\mathbf{P}_n}{d\lambda} = \frac{e}{(2\pi)^3} \int d\mathbf{k} 2\text{Im}\langle\partial_\lambda u_{n\mathbf{k}}|\nabla_{\mathbf{k}} u_{n\mathbf{k}}\rangle. \quad (2.17)$$

After a summation over the occupied bands and an integration over λ , the change of polarization takes the form

$$\Delta\mathbf{P} = \Delta\mathbf{P}_{\text{ion}} + [\mathbf{P}_{\text{el}}(\lambda = 1) - \mathbf{P}_{\text{el}}(\lambda = 0)], \quad (2.18)$$

where the explicit expression for the electronic contribution is

$$\mathbf{P}_{\text{el}}(\lambda) = \frac{e}{(2\pi)^3} \sum_n \int d\mathbf{k} \text{Im}\langle u_{n\mathbf{k}}|\nabla_{\mathbf{k}}|u_{n\mathbf{k}}\rangle. \quad (2.19)$$

After including the ionic contribution to the polarization, the final result for the formal polarization is

$$\mathbf{P} = \frac{e}{(2\pi)^3} \sum_n \int d\mathbf{k} \text{Im}\langle u_{n\mathbf{k}}|\nabla_{\mathbf{k}}|u_{n\mathbf{k}}\rangle + \frac{e}{\Omega} \sum_s Z_s^{\text{ion}} \mathbf{r}_s, \quad (2.20)$$

where eZ^{ion} is the nominal charge of the ion located at \mathbf{r}_s and Ω is the volume of the unit cell.

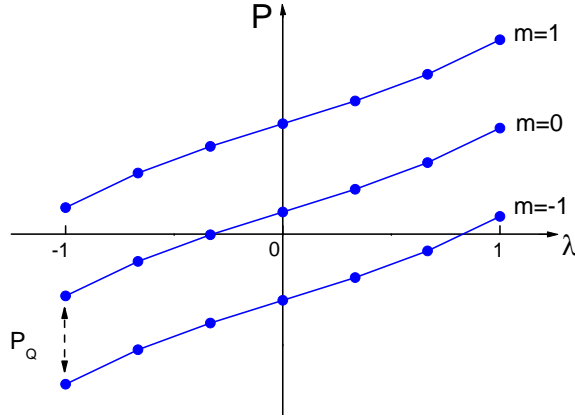


Figure 2.3: Polarization as a function of λ . The formal polarization is a multivalued quantity and at a certain λ value, the polarization in different branches differ by an integer times the polarization quantum \mathbf{P}_Q . Within each path, the polarization stays on the same branch and changes continuously.

The integrand in Eq. (2.19) has the form of $\mathbf{A}(k) = i\langle u_{n\mathbf{k}} | \nabla_{\mathbf{k}} | u_{n\mathbf{k}} \rangle$, which is known as the “Berry connection,” and the integral over the Brillouin zone is known as a “Berry phase.” A remarkable feature of the Berry phase is that the integral is independent of the path that traverses the parameter space if the path is adiabatically slow. Therefore, the result from Eq. (2.19) only depends on the initial and final states, as long as the path connecting them stays insulating. The averaged Berry phase for band n in direction j is $\phi_{n,j} = (\Omega/e) \mathbf{G}_j \cdot \mathbf{P}_n$, where \mathbf{G}_j is a primitive reciprocal vector corresponding to the primitive lattice vector \mathbf{R}_j that satisfies $\mathbf{G}_i \cdot \mathbf{R}_j = 2\pi\delta_{ij}$. Therefore, the electronic polarization from the n th band can be expressed in terms of the Berry phase of the n th band as

$$\mathbf{P}_n = \frac{1}{2\pi} \frac{e}{\Omega} \sum_j \phi_{n,j} \mathbf{R}_j. \quad (2.21)$$

Since the Berry phase is only well-defined modular 2π , the change of polarization in Eq. (2.18) and the formal polarization in Eq. (2.20) is also defined modular a polarization quantum $\mathbf{P}_Q = e\mathbf{R}/V_{\text{cell}}$, as shown in Fig. 2.3. For a given adiabatic path, the branch m is determined, and the polarization changes continuously along the path. Therefore, if the path is known, the change in polarization defined by Eq. (2.18) is a well-defined single-value vector quantity.

Chapter 3

Dynamical magnetic charges and magnetoelectric effects

3.1 Introduction

The magnetoelectric (ME) effect describes the phenomenon of inducing polarization \mathbf{P} by applying an external magnetic field \mathbf{H} , or generating magnetization by an applied electric field \mathcal{E} . The effect can be either linearly or nonlinearly to the applied field, and for the linear effect, the ME tensor α can be decoupled into three contributions depending on their microscopic origins as

$$\alpha = \alpha_{\text{elec}} + \alpha_{\text{ion}} + \alpha_{\text{strain}}, \quad (3.1)$$

where α_{elec} , α_{ion} and α_{strain} are the electronic (frozen-ion), ionic (lattice-mediated) and strain-mediated contributions [65]. The sketch of each term is illustrated in Fig. 3.1. The electronic contribution arises from the change in the wavefunction under an external field with all atomic coordinates frozen. In principle, this frozen-ion contribution can be measured at high frequency where ions cannot respond to the rapid changing field. On the contrary, α_{ion} and α_{strain} are all related to responses from the lattice, where α_{ion}

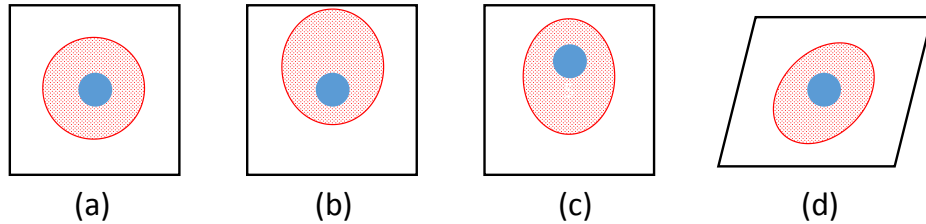


Figure 3.1: Sketch for different contributions to magnetoelectric effect. (a) The high symmetry system under no external field. (b) The electronic, (c) ionic, and (d) strain-mediated contributions. The small blue circle represents ion, the large red oval represents electron cloud, and the black outline represents the unit cell.

is from the change of internal ionic positions and α_{strain} arises from the change in the unit cell shape and volume. As the symmetry condition for the strain-mediated term is more restrictive, this term is absent in most bulk materials. From another aspect, the induced magnetization has two origins, namely, the orbital and spin magnetization. This also corresponds to $\mathbf{p} \cdot \mathbf{A}$ and Zeeman terms in the Hamiltonian. Therefore, each of the three ME couplings can be further subdivided into spin and orbital contributions.

The early *ab initio* studies were focused on the spin contribution to the ME effect, by integrating the spin density in the unit cell [66, 67, 68] or including a Zeeman term in the Hamiltonian [69]. Although there has been an attempt to obtain the orbital contribution by integrating the orbital moment in the vicinity of magnetic ions [70], the rigorous treatment of orbital magnetization, the modern theory of orbital magnetization [71, 72, 73], has become available recently. Therefore, first-principles methods have only recently been developed to calculate the full ME response tensor α , including both spin and orbital contributions [74].

Previous studies have shown that the spin-lattice term is dominant in many ME materials, for example, in Cr_2O_3 [74], as the orbital moment is usually strongly quenched on the transition-metal sites. Íñiguez has shown that the lattice contribution is proportional to the dynamical magnetic charge, which is the magnetic analog of the dynamical Born charge [66]. This dynamical magnetic charge is defined as

$$Z_{m\nu}^{\text{m}} = \Omega_0 \left. \frac{\partial M_\nu}{\partial u_m} \right|_{\boldsymbol{\varepsilon}, \mathbf{H}, \boldsymbol{\eta}}. \quad (3.2)$$

Here Ω_0 is the volume of the unit cell containing N atoms, and u_m denotes a periodicity-preserving sublattice displacement, where m is a composite label running from 1 to $3N$ to represent the atom and its displacement direction. The magnetic charge tensor Z^{m} plays an important role in various lattice-mediated magnetic responses and contributes to the Lyddane-Sachs-Teller relationship in ME materials [75, 76], but the mechanisms that give rise to it are not yet well understood. In particular, one route to optimizing the ME coupling is clearly to enhance Z^{m} , but it is not obvious how to do so.

In this chapter, we use first-principles density functional methods to study the dynamical magnetic charges and explore the different mechanisms that are responsible

for them in two representative materials. The materials are Cr_2O_3 , in which the ME effect is driven by spin-orbital coupling (SOC) mechanism, and a fictitious structure, “KITPite”, which was reported to have a large spin-lattice ME coupling according to a previous theory [77]. The structure of KITPite is such that the superexchange interactions between the magnetic moments of Mn ions are frustrated, leading to a 120° non-collinear spin structure. Our study shows that the large Z^m values in KITPite, which are orders of magnitude stronger than in Cr_2O_3 , are responsible for the strong ME effect. It is also found that this enhancement is present even when SOC is completely absent, thus confirming that it arises from exchange striction acting on the non-collinear spins, in contrast to the case of Cr_2O_3 where Z^m is driven only by SOC effects.

3.2 Formalism

In this section, following Wojdel and Íñiguez [66, 67], we generalize the formalism of Wu, Vanderbilt and Hamann [78] to include magnetic field, and use this systematic treatment to derive the ionic contribution of ME coupling and other magnetic properties.

For an insulating system with N atoms in a unit cell, four kinds of perturbation are considered: (i) a homogeneous electric field $\boldsymbol{\mathcal{E}}$, whose indices β, γ run over $\{x, y, z\}$; (ii) a homogeneous magnetic field \mathbf{H} , whose indices ν, ω also run over $\{x, y, z\}$; (iii) a homogeneous strain $\boldsymbol{\eta}$, with Voigt indices $i, j = \{1 \dots 6\}$; and (iv) internal displacements \mathbf{u} , indexed by composite labels m, n (atom and displacement direction) running over $1, \dots, 3N$. Here the displacements preserve the bulk periodicity, corresponding to zone-center phonon modes.

The magnetoelectric enthalpy density is defined as

$$E(\mathbf{u}, \boldsymbol{\eta}, \boldsymbol{\mathcal{E}}, \mathbf{H}) = \frac{1}{\Omega_0} [E_{\text{cell}}^{(0)} - \Omega(\boldsymbol{\mathcal{E}} \cdot \mathbf{P} + \mu_0 \mathbf{H} \cdot \mathbf{M})], \quad (3.3)$$

where $E_{\text{cell}}^{(0)}$ is the the zero-field energy per cell and μ_0 is the permeability of free space. Ω_0 and Ω are the undeformed and deformed cell volumes, respectively. $E(\mathbf{u}, \boldsymbol{\eta}, \boldsymbol{\mathcal{E}}, \mathbf{H})$

can be expanded around the zero-field equilibrium structure as

$$\begin{aligned}
E = & E_0 + A_m u_m + A_j \eta_j + A_\beta \mathcal{E}_\beta + A_\nu H_\nu + \frac{1}{2} B_{mn} u_m u_n + \frac{1}{2} B_{jk} \eta_j \eta_k \\
& + \frac{1}{2} B_{\beta\gamma} \mathcal{E}_\beta \mathcal{E}_\gamma + \frac{1}{2} B_{\nu\omega} H_\nu H_\omega + B_{mj} u_m \eta_j + B_{m\beta} u_m \mathcal{E}_\beta \\
& + B_{m\nu} u_m H_\nu + B_{\beta j} \mathcal{E}_\beta \eta_j + B_{\nu j} H_\nu \eta_j + B_{\beta\nu} \mathcal{E}_\beta H_\nu,
\end{aligned} \tag{3.4}$$

where summation over repeated indices is implied throughout. The coefficients of the first-order terms correspond to the atomic forces $F_m = -\Omega_0 A_m$, the stress tensor $\sigma_j = A_j$, the spontaneous polarization $(P_S)_\beta = -A_\beta$, and the spontaneous magnetization $(M_S)_\nu = -\mu_0^{-1} A_\nu$. In the equilibrium structure, the atomic forces and the stress tensor vanish. The diagonal second-order coefficients provide the force-constant matrix

$$K_{mn} = \Omega_0 \frac{\partial^2 E}{\partial u_m \partial u_n} \Big|_{\boldsymbol{\varepsilon}, \mathbf{H}, \boldsymbol{\eta}} = - \frac{\partial F_m}{\partial u_n} \Big|_{\boldsymbol{\varepsilon}, \mathbf{H}, \boldsymbol{\eta}} = \Omega_0 B_{mn}, \tag{3.5}$$

the frozen-ion elastic tensor $\bar{C}_{jk} = B_{jk}$, the frozen-ion electric susceptibility $\bar{\chi}_{\beta\gamma}^e = -\epsilon_0^{-1} B_{\beta\gamma}$, and the frozen-ion magnetic susceptibility $\bar{\chi}_{\nu\omega}^m = -\mu_0^{-1} B_{\nu\omega}$, where the bar on a quantity indicates a purely electronic response computed at fixed internal coordinates of the atoms and ϵ_0 is the permittivity of vacuum. The remaining terms correspond to off-diagonal responses, namely the force-response internal-strain tensor

$$\Lambda_{mj} = -\Omega_0 \frac{\partial^2 E}{\partial u_m \partial \eta_j} \Big|_{\boldsymbol{\varepsilon}, \mathbf{H}} = \frac{\partial F_m}{\partial \eta_j} \Big|_{\boldsymbol{\varepsilon}, \mathbf{H}} = -\Omega_0 \frac{\partial \sigma_j}{\partial u_m} \Big|_{\boldsymbol{\varepsilon}, \mathbf{H}, \boldsymbol{\eta}} = -\Omega_0 B_{mj}, \tag{3.6}$$

the frozen-ion piezoelectric tensor $\bar{e}_{\beta j} = -B_{\beta j}$, the frozen-ion piezomagnetic tensor $\bar{h}_{\nu j} = -\mu_0^{-1} B_{\nu j}$, the frozen-ion ME tensor $\bar{\alpha}_{\beta\nu} = -B_{\beta\nu}$, the atomic Born charge tensor

$$Z_{m\beta}^e = -\Omega_0 \frac{\partial^2 E}{\partial u_m \partial \mathcal{E}_\beta} \Big|_{\mathbf{H}, \boldsymbol{\eta}} = \Omega_0 \frac{\partial P_\beta}{\partial u_m} \Big|_{\boldsymbol{\varepsilon}, \mathbf{H}, \boldsymbol{\eta}} = \frac{\partial F_m}{\partial \mathcal{E}_\beta} \Big|_{\mathbf{H}, \boldsymbol{\eta}} = -\Omega_0 B_{m\beta}, \tag{3.7}$$

and the atomic magnetic charge tensor

$$Z_{m\nu}^m = -\Omega_0 \mu_0^{-1} \frac{\partial E^2}{\partial u_m \partial H_\nu} \Big|_{\boldsymbol{\varepsilon}, \boldsymbol{\eta}} = \Omega_0 \frac{\partial M_\nu}{\partial u_m} \Big|_{\boldsymbol{\varepsilon}, \mathbf{H}, \boldsymbol{\eta}} = \mu_0^{-1} \frac{\partial F_m}{\partial H_\nu} \Big|_{\boldsymbol{\varepsilon}, \boldsymbol{\eta}} = -\Omega_0 \mu_0^{-1} B_{m\nu}. \tag{3.8}$$

Static physical responses arise not only from the electronic part (barred quantities), but also from the ionic contribution associated with the change of the equilibrium internal displacements u_m with fields or strain. Therefore, the relaxed-ion ME enthalpy is

$$\tilde{E}(\boldsymbol{\eta}, \boldsymbol{\varepsilon}, \mathbf{H}) = \min_{\mathbf{u}} E(\mathbf{u}, \boldsymbol{\eta}, \boldsymbol{\varepsilon}, \mathbf{H}), \tag{3.9}$$

and the minimization is accomplished by substituting

$$u_m = -(B^{-1})_{mn}(B_{nj}\eta_j + B_{n\beta}\mathcal{E}_\beta + B_{n\nu}H_\nu) \quad (3.10)$$

into Eq. (3.4) to obtain the total relaxed-ion response (including both electronic and ionic parts). The total relaxed-ion electric susceptibility, magnetic susceptibility, elastic, piezoelectric, piezomagnetic, and ME tensors are then

$$\chi_{\beta\gamma}^e = -\epsilon_0^{-1} \frac{\partial^2 \tilde{E}}{\partial \mathcal{E}_\beta \partial \mathcal{E}_\gamma} \Big|_{\mathbf{H}, \boldsymbol{\eta}} = \bar{\chi}_{\beta\gamma}^e + \Omega_0^{-1} \epsilon_0^{-1} Z_{m\beta}^e (K^{-1})_{mn} Z_{n\gamma}^e, \quad (3.11)$$

$$\chi_{\nu\omega}^m = -\mu_0^{-1} \frac{\partial^2 \tilde{E}}{\partial H_\nu \partial H_\omega} \Big|_{\boldsymbol{\varepsilon}, \boldsymbol{\eta}} = \bar{\chi}_{\nu\omega}^m + \Omega_0^{-1} \mu_0 Z_{m\nu}^m (K^{-1})_{mn} Z_{n\omega}^m, \quad (3.12)$$

$$C_{jk} = \frac{\partial^2 \tilde{E}}{\partial \eta_j \partial \eta_k} \Big|_{\boldsymbol{\varepsilon}, \mathbf{H}} = \bar{C}_{jk} - \Omega_0^{-1} \Lambda_{mj} (K^{-1})_{mn} \Lambda_{nk}, \quad (3.13)$$

$$e_{\beta j} = -\frac{\partial^2 \tilde{E}}{\partial \mathcal{E}_\beta \partial \eta_j} \Big|_{\mathbf{H}} = \bar{e}_{\beta j} + \Omega_0^{-1} Z_{m\beta}^e (K^{-1})_{mn} \Lambda_{nj}, \quad (3.14)$$

$$h_{\nu j} = -\frac{\partial^2 \tilde{E}}{\partial H_\nu \partial \eta_j} \Big|_{\boldsymbol{\varepsilon}} = \bar{h}_{\nu j} + \Omega_0^{-1} Z_{m\nu}^m (K^{-1})_{mn} \Lambda_{nj}, \quad (3.15)$$

$$\alpha_{\beta\nu} = -\frac{\partial^2 \tilde{E}}{\partial \mathcal{E}_\beta \partial H_\nu} \Big|_{\boldsymbol{\eta}} = \bar{\alpha}_{\beta\nu} + \Omega_0^{-1} \mu_0 Z_{m\beta}^e (K^{-1})_{mn} Z_{n\nu}^m. \quad (3.16)$$

The six lattice-mediated responses in Eqs. (3.11-3.16) are all made up of four fundamental tensors: the Born charge Z^e , the magnetic charge Z^m , the internal strain tensor Λ , and the inverse force-constant matrix K^{-1} . The manner in which these six lattice responses are computed from the four fundamental tensors is illustrated in Fig. (3.2), which depicts the linear-response connections between elastic, electric and magnetic degrees of freedom.

The above equations also have very intuitive interpretations. Here we use the ME response from the lattice contribution as an example to demonstrate its physical meaning. In an electric field, the Born charge tensor Z^e describes the force on each atom induced by the electric field. Then the inverse force-constant matrix K^{-1} tells how large the atomic displacement should be at a certain force. Finally, the dynamical magnetic

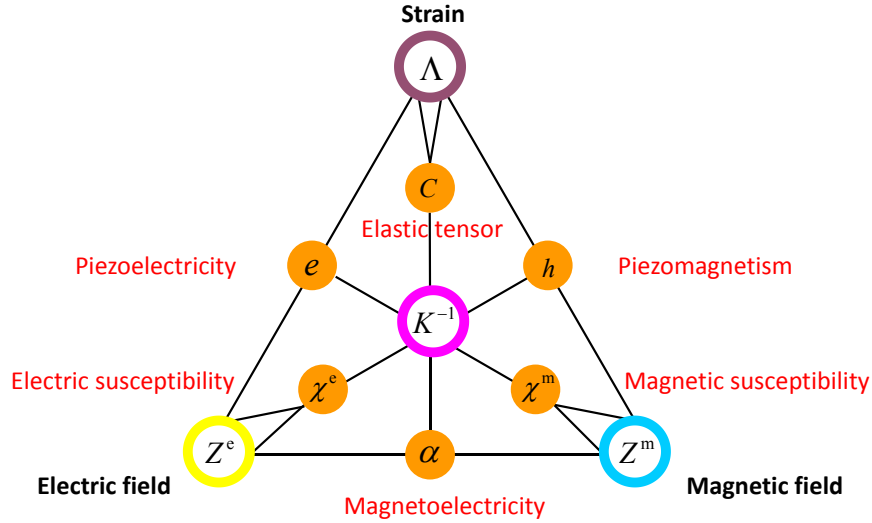


Figure 3.2: Sketch showing how the six lattice-mediated responses indicated by solid circles are built up from the four elementary tensors indicated by open circles: the Born charge Z^e , magnetic charge Z^m , internal strain Λ , and force-constant inverse K^{-1} . Each lattice-mediated response is given by the product of the three elementary tensors connected to it, as indicated explicitly in Eqs. (3.11-3.16).

charge tensor gives the amount of magnetization induced by a certain atomic displacement. Therefore, the lattice contribution to the ME effect is given by the product of Z^e , K^{-1} , and Z^m as shown in Eq. 3.16.

If the crystal symmetry allows piezoelectric or piezomagnetic effects, then the strain degree of freedom can similarly be eliminated by minimizing the ME enthalpy with respect to strain $\boldsymbol{\eta}$, leading to a strain-mediated contributions to χ^e or χ^m . If both piezoelectric and piezomagnetic effects are present, there is an additional term α_{strain} to the ME response which is proportional to the piezoelectric tensor and piezomagnetic tensor [67].

The above derivations are carried out in the $(\boldsymbol{\mathcal{E}}, \boldsymbol{\mathbf{H}})$ frame, which is consistent with the usual experimental convention. In the context of first-principles calculation, however, it is more natural to work in the $(\boldsymbol{\mathcal{E}}, \boldsymbol{\mathbf{B}})$ frame, as $\boldsymbol{\mathcal{E}}$ and $\boldsymbol{\mathbf{B}}$ are directly related to the scalar and vector potentials ϕ and \mathbf{A} . The ME tensor α has different units in these two frames. In the $(\boldsymbol{\mathcal{E}}, \boldsymbol{\mathbf{H}})$ frame, α is defined through Eq. (3.16) so that the units are

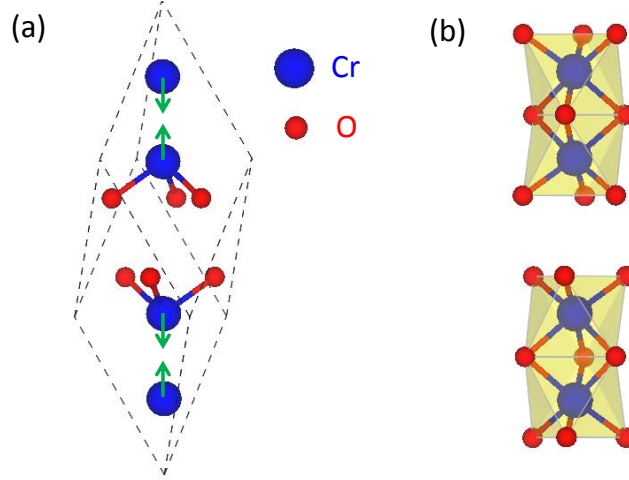


Figure 3.3: Structure of Cr_2O_3 . (a) In the primitive cell, four Cr atoms align along the the rhombohedral axis with AFM order represented by the arrows on Cr atoms. (b) Each Cr atom is at the center of a distorted oxygen octahedron.

s/m. In the $(\mathcal{E}, \mathbf{B})$ frame, α is instead defined as

$$\alpha_{\beta\nu}^{\mathcal{E}\mathbf{B}} = \left. \frac{\partial M_\nu}{\partial \mathcal{E}_\beta} \right|_{\mathbf{B}} = \left. \frac{\partial P_\beta}{\partial B_\nu} \right|_{\mathcal{E}} \quad (3.17)$$

and carries units of inverse Ohm, the same as for $\sqrt{\epsilon_0/\mu_0}$, the inverse of the impedance of free space. The ME tensors in these two frames are related by $\alpha^{\mathcal{E}\mathbf{H}} = (\mu\alpha)^{\mathcal{E}\mathbf{B}}$, where μ is the magnetic permeability. The electric and magnetic dynamical charges in the two frames are related by $(Z^e)^{\mathcal{E}\mathbf{H}} = (Z^e + \alpha\mu Z^m)^{\mathcal{E}\mathbf{B}}$ and $(Z^m)^{\mathcal{E}\mathbf{H}} = (\mu Z^m/\mu_0)^{\mathcal{E}\mathbf{B}}$.

For non-ferromagnetic materials we have $\mu \approx \mu_0$, so that the Z^m values are essentially the same in the two frames. The same is also true for Z^e , since the product $(\alpha\mu Z^m)^{\mathcal{E}\mathbf{B}}$ is at least five orders of magnitude smaller than Z^e in most ME materials. Since the difference are negligible, in this thesis, the results of ME coupling are reported in the more conventional $(\mathcal{E}, \mathbf{H})$ frame, even though the computations are carried out in the $(\mathcal{E}, \mathbf{B})$ frame.

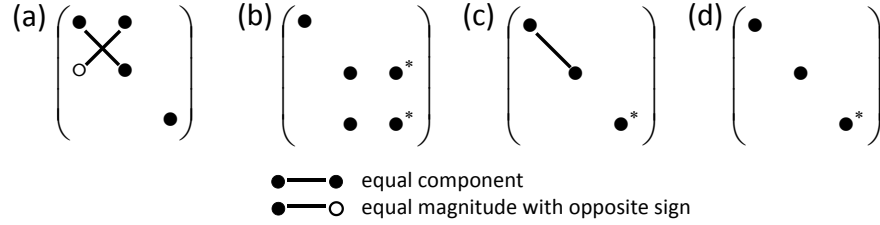


Figure 3.4: Symmetry pattern of Born and magnetic charge tensors for (a) the Cr atom in Cr_2O_3 , (b) the O atom in Cr_2O_3 and the O^2 atom in $\text{CaAlMn}_3\text{O}_7$, (c) the Ca, Al and O^1 atoms in $\text{CaAlMn}_3\text{O}_7$, and (d) the Mn and O^3 atoms in $\text{CaAlMn}_3\text{O}_7$. The elements indicated by an asterisk vanish in the absence of SOC for Z^m in $\text{CaAlMn}_3\text{O}_7$.

3.3 Structure and symmetry

3.3.1 Cr_2O_3

Cr_2O_3 adopts the corundum structure with two formula units per rhombohedral primitive cell as shown in Fig. 3.3(a) and each Cr atom is at the center of a distorted oxygen octahedron as illustrated in Fig. 3.3(b). Below the Néel temperature $T_N = 307$ K, Cr_2O_3 is an antiferromagnetic (AFM) insulator in which the spin moments on Cr atoms alternate directions along the rhombohedral axis. The magnetic space group is $R\bar{3}'c'$ which allows a non-zero ME tensor with two independent components $\alpha_{\perp} = \alpha_{xx} = \alpha_{yy}$ and $\alpha_{\parallel} = \alpha_{zz}$. In addition, this magnetic group has the feature that all the improper rotations are coupled to the time-reversal operator and vice versa. Therefore, pseudovectors and ordinary vectors transform in the same way, implying that the magnetic charge Z^m and the Born charge Z^e have the same tensor forms. The three-fold rotational symmetry on each Cr atom restricts its charge tensor to have the form shown in Fig. 3.4(a). The symmetry is lower on O atoms; for the one lying on the two-fold rotation axis along \hat{x} direction, for example, the charge tensor take the form shown in Fig. 3.4(b).

3.3.2 KITPite

The fictitious “KITPite” structure with chemical formula $\text{CaAlMn}_3\text{O}_7$ is Kagome-like with 120° in-plane AFM spin order as showed in Fig. 3.5. The unit cell includes two formula units made by stacking two MnO layers with 180° rotation between layers.

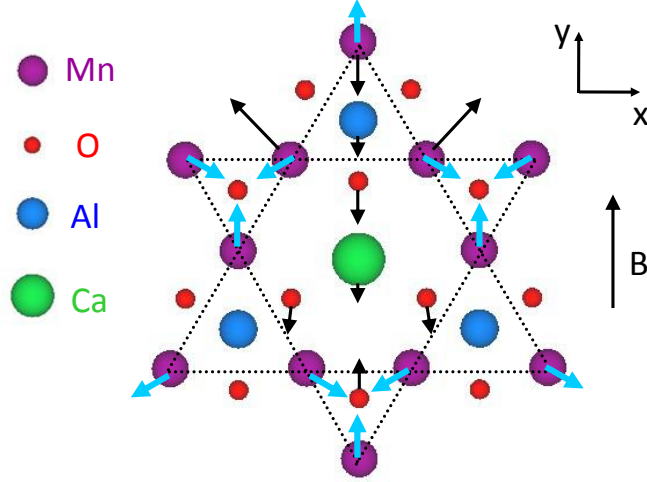


Figure 3.5: Planar view of the $\text{CaAlMn}_3\text{O}_7$ (KITPite) structure. The broad arrows (blue) on the Mn atoms represent the magnetic moment directions in the absence of electric or magnetic fields. Small (black) arrows indicate the atomic forces induced by an external magnetic field applied in the \hat{y} direction.

Each Mn atom is surrounded by an oxygen bipyramid and the O atoms are in three nonequivalent Wyckoff positions: O^1 is in the voids of the Mn triangles; O^2 is the apical atoms located between the two MnO layers (not shown in the planar view); and O^3 forms the MnO hexagons. The magnetic space group is $6_3/m'm'c'$; this has the same symmetry feature as Cr_2O_3 , namely that improper rotations and the time-reversal symmetry are coupled together, so that the Born charges and the magnetic charges follow the same symmetry restrictions. The charge tensors for Ca, Al and O^1 atoms have the symmetry pattern shown in Fig. 3.4(c), and the Mn and O^3 atoms have the charge tensor form of Fig. 3.4(d). For the apical O^2 atoms, the five independent components in the charge tensor can be written in the form of Fig. 3.4(b) when the on-site two-fold axis is along the \hat{x} direction.

The elements marked by asterisks in Fig. 3.4 are those that vanish for Z^m in $\text{CaAlMn}_3\text{O}_7$ when SOC is neglected. The system of magnetic moments is exactly coplanar in the absence of SOC, and will remain so even after the application of any first-order nonmagnetic perturbation. Thus, spin components along \hat{z} direction cannot be induced, and it follows that the elements in the third column all vanish in all atomic

Z^m tensors in $\text{CaAlMn}_3\text{O}_7$ when SOC is neglected.

3.4 First-principles methodology

The calculations for Cr_2O_3 are performed with QUANTUM ESPRESSO [57] using the generalized-gradient approximation parametrized by the Perdew-Burke-Ernzerhof functional [50]. We employ Troullier-Martin norm-conserving pseudopotentials [79] with SOC included and Cr $3s$ and $3p$ states incorporated in the valence. The wavefunctions are expanded in a plane-wave basis with cutoff energy 150 Ry, and a $4 \times 4 \times 4$ Monkhorst-Pack k -mesh is used to sample the Brillouin zone.

In order to calculate Born charges, magnetic charges, and the Γ -point force-constant matrix, finite-difference method is used by displacing atomic sublattices in each Cartesian direction and computing the Berry-phase polarization [34], total magnetization, and the Hellmann-Feynman forces. A $4 \times 4 \times 5$ k -mesh sampling is found to be sufficient for the polarization calculations, and the orbital magnetization is calculated using the modern theory of orbital magnetization [80, 72, 81].

Calculations for the fictitious KITPite material are carried out with plane-wave density-functional theory implemented in VASP [56]. The ionic core environment is simulated by projector augmented wave pseudopotentials [61]. A energy cutoff of 400 eV is used for the non-collinear magnetization calculation without SOC. For the exchange-correlation functional we use the rotationally invariant LSDA+U functional [54], with Hubbard $U = 5.5$ eV and $J = 2.0$ eV [82] on the d orbital of the Mn atoms. The Born charge and the Γ -point force-constant matrix are obtained by linear-response methods, while the magnetic charges are computed by applying an uniform Zeeman field in the crystal and computing the resulting forces [69]. A $4 \times 4 \times 4$ Monkhorst-Pack k -mesh is used in the calculations.

3.5 Results and discussion

3.5.1 Structure and phonon

The ground-state structural parameters of Cr_2O_3 are summarized in Table 3.1, and the calculated results are in good agreement with experiments. A group-theory analysis of the long-wavelength phonons shows that the infrared (IR)-active phonon modes, which couple to the electric field, are the longitudinal A_{2u} modes and the transverse doubly-degenerated E_u modes

$$\Gamma_{\text{IR}} = 2A_{2u} + 4E_u, \quad (3.18)$$

where the acoustic modes have been excluded. Since Born charges and magnetic charges have the same tensor form in Cr_2O_3 (also true for $\text{CaAlMn}_3\text{O}_7$), the IR-active modes are also coupled to magnetic field. The computed frequencies of IR-active modes in Cr_2O_3 are shown in Table 3.2, and the results are consistent with experiments.

The structure of KITPite $\text{CaAlMn}_3\text{O}_7$ is relaxed in the assumed $6_3/m'm'c'$ symmetry, and the unit cell has a volume of 311.05 \AA^3 with a c/a ratio of 0.998. The Wyckoff coordinates for the Mn atoms (6h) and O^3 atoms (6g) are 0.5216 and 0.1871, while other atoms are in high-symmetry Wyckoff positions. The IR-active modes are

$$\Gamma_{\text{IR}} = 6A_{2u} + 9E_{1u} \quad (3.19)$$

excluding the acoustic modes. The longitudinal A_{2u} modes do not contribute to the magnetic response when SOC is absent in $\text{CaAlMn}_3\text{O}_7$, because the longitudinal components of the magnetic charges Z^m are zero.

Table 3.1: Structural parameters of Cr_2O_3 from first-principles calculation and experiments: rhombohedral lattice constant a , lattice angle α , and Wyckoff positions for Cr (4c) and O (6e).

	a (\AA)	α ($^\circ$)	Wyckoff position	
			Cr	O
This work	5.386	54.3	0.1546	0.0617
Expt. (Ref. [83])	5.358	55.0	0.1528	0.0566

Table 3.2: Frequencies (cm^{-1}) of IR-active phonon modes of Cr_2O_3 from first-principles calculations and experiments. The two A_{2u} modes are at longitudinal direction; the four E_u modes are at transverse direction (doubly degenerate).

	A_{2u} modes			E_u modes		
This work	388	522	297	427	510	610
Expt. (Ref. [84])	402	533	305	440	538	609

3.5.2 Born charge

The Born charge tensors for Cr and O atoms in Cr_2O_3 are computed to be

$$Z^e(\text{Cr}) = \begin{pmatrix} 3.02 & -0.30 & 0 \\ 0.30 & 3.02 & 0 \\ 0 & 0 & 3.18 \end{pmatrix} e, \quad Z^e(\text{O}) = \begin{pmatrix} -2.36 & 0 & 0 \\ 0 & -1.66 & -1.00 \\ 0 & -0.88 & -2.12 \end{pmatrix} e,$$

and the independent Born charge tensors in $\text{CaAlMn}_3\text{O}_7$ are

$$Z^e(\text{Ca}) = \begin{pmatrix} 3.09 & 0 & 0 \\ 0 & 3.09 & 0 \\ 0 & 0 & 2.06 \end{pmatrix} e, \quad Z^e(\text{O}^1) = \begin{pmatrix} -3.40 & 0 & 0 \\ 0 & -3.40 & 0 \\ 0 & 0 & -0.94 \end{pmatrix} e,$$

$$Z^e(\text{Mn}) = \begin{pmatrix} 2.19 & 0 & 0 \\ 0 & 4.09 & 0 \\ 0 & 0 & 5.59 \end{pmatrix} e, \quad Z^e(\text{O}^2) = \begin{pmatrix} -1.06 & 0 & 0 \\ 0 & -1.58 & -0.12 \\ 0 & 0.02 & -5.63 \end{pmatrix} e,$$

$$Z^e(\text{Al}) = \begin{pmatrix} 2.98 & 0 & 0 \\ 0 & 2.98 & 0 \\ 0 & 0 & 3.24 \end{pmatrix} e, \quad Z^e(\text{O}^3) = \begin{pmatrix} -3.10 & 0 & 0 \\ 0 & -2.29 & 0 \\ 0 & 0 & -1.41 \end{pmatrix} e.$$

Even though, Cr_2O_3 and $\text{CaAlMn}_3\text{O}_7$ have quite different structures and spin orders, Born charges in both materials are similar in magnitude and are close to the atomic valence charge values.

3.5.3 Magnetic charge

The results for magnetic charge tensors of Cr_2O_3 are reported in atomic basis in Table 3.3 and IR-active mode basis in Table 3.5. Despite the fact that the symmetry constraints on the non-zero elements are the same for Born charges and magnetic charges, their numerical patterns are quite different, as Born charges is sensitive to the local bonding environment while magnetic charges, e.g. the spin contribution, are related to spin directions.

The magnetic charge results firstly suggest that although O atom does not have magnetic moment, its magnetic charge is not negligible and it can be comparable to the magnetic charge of magnetic cations. Secondly, for both Cr and O atoms, the spin contributions are dominant in the transverse direction, but much weaker in the longitudinal direction. This is to be expected from the nearly collinear spin order of Cr_2O_3 , considering that the magnitudes of the magnetic moments are quite stiff while their orientations are relatively free to rotate. Thirdly, the main effect in the longitudinal direction is from the orbital-magnetization contribution. Incidentally, we also find that the longitudinal components of the magnetic charge for Cr atoms are very sensitive to the lattice constant of Cr_2O_3 , especially the Cr-O distance in the longitudinal direction. Therefore, it is possible that a strain can be used to magnify the magnetic charge.

The magnetic charge tensors of $\text{CaAlMn}_3\text{O}_7$ are reported in atomic basis in Table 3.4 and IR-active mode basis in Table 3.6, respectively. Magnetic charges in the KITPite structure are found to be much larger than for Cr_2O_3 . For example, comparing the transition-metal atom, the magnetic charge of Mn in KITPite is ~ 50 times larger than

Table 3.3: Magnetic charges Z^m ($10^{-2}\mu_B/\text{\AA}$) for Cr_2O_3 in the atomic basis.

	spin	orbital		spin	orbital
$Z_{xx}^m(\text{Cr})$	5.88	0.25	$Z_{yy}^m(\text{O})$	-1.95	-0.38
$Z_{xy}^m(\text{Cr})$	-5.69	0.02	$Z_{yz}^m(\text{O})$	0.00	1.12
$Z_{zz}^m(\text{Cr})$	0.02	0.23	$Z_{zy}^m(\text{O})$	-1.10	-0.72
$Z_{xx}^m(\text{O})$	-5.92	0.06	$Z_{zz}^m(\text{O})$	-0.02	-0.15

Table 3.4: Magnetic charges Z^m ($10^{-2}\mu_B/\text{\AA}$) for KITPite $\text{CaAlMn}_3\text{O}_7$ in atomic basis.

	spin		spin
$Z_{xx}^m(\text{Ca})$	-43.46	$Z_{xx}^m(\text{O}^2)$	-39.15
$Z_{xx}^m(\text{Al})$	-24.63	$Z_{yy}^m(\text{O}^2)$	1.23
$Z_{xx}^m(\text{Mn})$	341.53	$Z_{zy}^m(\text{O}^2)$	-37.62
$Z_{yy}^m(\text{Mn})$	-171.46	$Z_{xx}^m(\text{O}^3)$	-56.09
$Z_{xx}^m(\text{O}^1)$	66.98	$Z_{yy}^m(\text{O}^3)$	-75.23

the magnetic charge of Cr in Cr_2O_3 . This huge difference is originated from the fact that the magnetic charges in Cr_2O_3 are driven by SOC, which acts as an antisymmetric exchange field. As a consequence, the weakness of the SOC on Cr atoms implies that the magnetic charges and magnetic responses are small in Cr_2O_3 . In the KITPite structure, SOC is excluded in the calculation deliberately, so magnetic charges are purely induced by the superexchange between non-collinear spins on Mn atoms. This exchange striction mechanism causes magnetic charges in $\text{CaAlMn}_3\text{O}_7$ to be dozens of times larger than the SOC-driven responses in Cr_2O_3 .

Since the orbital magnetization is strongly quenched in most $3d$ transition metals atoms, we expect the orbital contribution to Z^m tensors in $\text{CaAlMn}_3\text{O}_7$ to be comparable with those in Cr_2O_3 , i.e., on the order of $10^{-2}\mu_B/\text{\AA}$. Since this is ~ 2 orders of magnitude smaller than the typical spin contribution in $\text{CaAlMn}_3\text{O}_7$, this is not included in our calculations. The main point of this study of KITPite $\text{CaAlMn}_3\text{O}_7$ is to demonstrate that exchange-striction effects can give rise to large Z^m values based on a mechanism that does not involve SOC at all.

3.5.4 Electric and magnetic responses

The lattice-mediated magnetic and electric responses for Cr_2O_3 are computed from Eqs. (3.11-3.16) and the results are summarized in the bottom panel of Table 3.5. The computed lattice-mediated electric susceptibility are in reasonable agreement with the room-temperature lattice-mediated $\chi_{\parallel}^e = 4.96$ and $\chi_{\perp}^e = 3.60$ obtained from IR reflectance measurements [84]. In contrast, the experimentally measured longitudinal and transverse magnetic susceptibility at low temperature are on the order of $\sim 10^{-3}$

Table 3.5: Top: Mode decomposition of the Born charges Z^e , and of the spin and orbital contributions to the magnetic charges Z^m , in Cr_2O_3 . C_n are the eigenvalues of the force-constant matrix. Bottom: Total A_{2u} -mode (longitudinal) and E_u -mode (transverse) elements of the lattice-mediated electric susceptibility χ^e , magnetic susceptibility χ^m , and the spin and orbital parts of the ME constant α .

	A_{2u} modes			E_u modes		
C_n (eV/Å ²)	10.5	22.9	10.2	16.0	20.2	30.9
Z^e (e)	1.15	8.50	0.55	0.39	3.71	7.07
Z_{spin}^m (10 ⁻² μ _B /Å)	0.02	0.05	-0.76	-3.97	16.14	10.55
Z_{orb}^m (10 ⁻² μ _B /Å)	2.74	-0.59	0.66	-0.80	-0.29	1.06
Latt. χ^e	6.2			4.37		
Latt. χ^m	0.05 × 10 ⁻⁸			1.28 × 10 ⁻⁸		
α_{spin} (ps/m)	0.0024			0.633		
α_{orb} (ps/m)	0.0097			0.025		

Table 3.6: Born charges Z^e and magnetic charges Z^m for IR-active A_{2u} modes in $\text{CaAlMn}_3\text{O}_7$. C_n are the eigenvalues of the force-constant matrix.

C_n (eV/Å ²)	Z^e (e)	Z_{spin}^m (10 ⁻² μ _B /Å)
-2.4	3.7	539.7
-1.1	4.7	17.2
2.8	4.3	-0.6
7.1	2.4	266.4
11.6	5.1	-107.8
12.0	2.4	-74.5
35.3	7.9	-15.9
46.7	2.2	34.8
55.1	4.6	-325.7

[85], which is about five orders of magnitude larger than the lattice-mediated results obtained from Eq. (3.12). This difference undoubtedly arises from the fact that the experimental χ^m is dominated by the electronic (i.e., frozen-ion) contribution $\bar{\chi}^m$ that is not included in Table 3.5. The ME response α_{\parallel} and α_{\perp} both agree closely with previous theory, which are in reasonable agreement with experiment [66, 74].

The calculated force-constant eigenvalues and Born charges of IR-active modes in KITPite are also listed in Table 3.6. As the KITPite structure is fictitious and two E_{1u} modes are unstable in the high-symmetry structure, we omit any discussion of the magnetic and dielectric responses.

3.6 Summary and outlook

In summary, we first present a systematic formulation of the role played by the dynamic magnetic charge tensor Z^m in the magnetic, ME, and piezomagnetic responses of crystalline solids. Then first-principles density-functional methods are used to compute the atomic Z^m tensors for two prototypical materials, namely Cr_2O_3 , a well-studied ME material, and fictitious KITPite, which displays a very large lattice ME effect. Our study shows that the physics is quite different in the two cases, with mechanisms based on SOC giving only small Z^m values in the collinear antiferromagnet Cr_2O_3 , while exchange-striction effects inducing very large Z^m in non-collinear KITPite.

This study is part of a broader effort to identify mechanisms that could induce large magnetic charge values. They help to reinforce a picture in which SOC give only weak contributions, at least in $3d$ transition-metal compounds, whereas exchange striction can induce much larger effects in materials with non-collinear spin structure. In this respect, the conclusions parallel those that have emerged with respect to the polarization in multiferroics and magnetically-induced improper ferroelectrics, where exchange striction, when present, typically produce much larger effects than spin-orbit mechanisms [86].

This work points to some possible future directions for exploration. One subsequent direction is to identify experimentally known materials in which exchange striction gives rise to large Z^m values. In such systems, lattice-mediated effects might even contribute significantly to the magnetic susceptibility; while such contributions are normally neglected for χ^m , we note that Z^m appears to the second power in Eq. (3.12), so this contribution might be significant, especially in soft-mode systems. It might also be interesting to explore the role of magnetic charges in the phenomenology of electromagnons [87]. Finally, we point out that, unlike Z^e , Z^m remains well-defined even in metals; while ME effects do not exist in this case, it would still be interesting to explore the consequences of large Z^m values in such systems.

Chapter 4

Magnetoelectric effects in hexagonal rare-earth manganites and ferrites

4.1 Introduction

In Chapter 3, it was shown that the linear magnetoelectric (ME) effect defined by Eq. (1.5) can be decomposed into electronic (frozen-ion), ionic (lattice-mediated), and strain-mediated contributions. Among them, the lattice-mediated contribution can be written as the matrix product of the Born charge tensor Z^e , the inverse force-constant matrix K^{-1} , and the dynamical magnetic charge tensors Z^m as shown in Eq. (3.16). The previous study on magnetic charges in Cr_2O_3 and KITPite suggests that exchange striction acting on non-collinear spin structures induces much larger magnetic charges than when Z^m is driven only by spin-orbit coupling (SOC). Hence, exchange striction provides a promising mechanism for obtaining large ME effect. However, KITPite is a fictitious material that is only used as a model system to demonstrate the exchange-striction mechanism. In practice, it is important to identify experimentally known materials in which exchange striction gives rise to large Z^m values and even large ME responses.

The hexagonal manganites RMnO_3 and ferrites RFeO_3 ($R = \text{Sc}, \text{Y}, \text{In}, \text{ and Ho-Lu}$) form an interesting class of materials exhibiting strong couplings between electric, magnetic, and structural degrees of freedom [88]. A series of first-principles and phenomenological studies have greatly enhanced our understanding of the coupled properties. The ferroelectricity is induced by the structural trimerization, and the direction of the spontaneous polarization is determined by the trimerization pattern [89, 90]. An unusual “cloverleaf” pattern formed from interlocking domain walls between structural

and ferroelectric domains has been found in hexagonal $RMnO_3$ [91] and is now understood in terms of Landau theory [92, 93, 94]. Hexagonal $RMnO_3$ and $RFeO_3$ have rich magnetic phase diagrams and show considerable potential for manipulation and practical applications [95, 96, 97]. The magnetic orders have two different origins, with the transition-metal ion Mn^{3+} or Fe^{3+} sublattices ordering first, often followed by ordering of the rare-earth ions R^{3+} at lower temperature. The magnetic anisotropy is easy-plane and easy-axis for $3d$ and $4f$ spins, respectively; the $3d$ moments are antiferromagnetically coupled through superexchange and form a 120° non-collinear arrangement in the x - y plane, while the $4f$ rare-earth moments are collinear along the hexagonal z -axis.

The low-temperature magnetic phases of $RMnO_3$ and $RFeO_3$ allow linear ME effects to be present. The ME force microscopy technique has been used successfully to observe the ME domains in $ErMnO_3$ [98]. In that work, a large ME component $\alpha_{zz} \sim 13$ ps/m has been measured at 4 K, which is below the Mn^{3+} ordering temperature of 81 K but above the Er^{3+} ordering temperature of 2 K. Recently, a first-principles study [35] has been conducted for this SOC-induced ME response in $ErMnO_3$, but the spin-lattice ME coupling α_{zz} arising from the Mn^{3+} order was found to be only 0.7-1.0 ps/m. This discrepancy suggests that the dominant ME effect in the hexagonal \hat{z} direction is mediated by the Er^{3+} $4f$ electrons in $ErMnO_3$. The in-plane ME effect, which has not been measured or calculated, has an origin that is similar to the KITPite with non-collinear spins interacting through superexchange. Thus, hexagonal $RMnO_3$ and $RFeO_3$ are good candidates to show exchange-striction enhanced magnetic charges and anomalously large spin-lattice ME effects.

In this chapter, we use first-principles density-functional methods to study the magnetic charges and the spin-induced ME effects arising from the $3d$ electrons in hexagonal $HoMnO_3$, $ErMnO_3$, $YbMnO_3$, $LuMnO_3$, and $LuFeO_3$. For the transverse magnetic charge components and ME couplings, we also provide a comparison between results induced solely by exchange striction and ones including SOC. The results confirm that the exchange striction greatly enhances the in-plane magnetic charges, while the SOC contribution is minor for most components except on Mn atoms. However, the effect

of SOC on the ME components is surprisingly large in many cases. This occurs because the exchange-striction contribution tends to be reduced by cancellations between modes, while the SOC contribution is mainly amplified by a few low-frequency modes. The in-plane ME responses are discussed case by case and the conditions under which exchange striction leads to anomalously large in-plane spin-lattice ME couplings are clarified.

4.2 Preliminary

4.2.1 Structure and magnetic phase

Hexagonal manganites $RMnO_3$ ($R = \text{Sc, Y, In, and Ho-Lu}$) are paraelectric insulators above the structural transition temperature $T_c \sim 900\text{-}1500\text{ K}$. The space group is $P6_3/mmc$ with two formula units (f.u.) per primitive cell. Below T_c , the size mismatch between the small-radius R^{3+} ion and the large MnO_5 bipyramid leads to an inward tilting of the three corner-shared MnO_5 polyhedra and an associated “one-up/two-down” buckling of the R^{3+} ion layer, as shown in Fig. 4.1. As a result, the transition triples (“trimerizes”) the unit cell and lowers the structural symmetry to $P6_3cm$ with two inequivalent R sites R_1 and R_2 , two distinct apical oxygen sites O_{T1} and O_{T2} , and two independent planar oxygen sites O_{P1} and O_{P2} . Meanwhile the trimerization is nonlinearly coupled to polarization, therefore, these systems are improper ferroelectrics [89, 90, 93].

The Mn^{3+} magnetic order develops below the Néel temperature T_N of $\sim 70\text{-}130\text{ K}$. The in-plane Mn-O-Mn superexchange determines the non-collinear 120° antiferromagnetic order on the Mn^{3+} triangular lattice. On the other hand, the inter-plane Mn-O- R -O-Mn exchange, which is two orders of magnitude weaker than the in-plane exchange, modulates the relative spin directions between two consecutive Mn planes [95, 35]. At temperatures lower than $\sim 5.5\text{ K}$, the rare-earth ions with partially filled $4f$ shells develop collinear spin order along the hexagonal \hat{z} direction. For the Mn^{3+} order, there are four distinct magnetic phases, namely A_1 ($P6_3cm$), A_2 ($P6_3c'm'$), B_1 ($P6'_3cm'$), and B_2 ($P6'_3c'm$). The A_1 and A_2 phases are shown in Fig. 4.2; the B_1 and B_2 phases can be

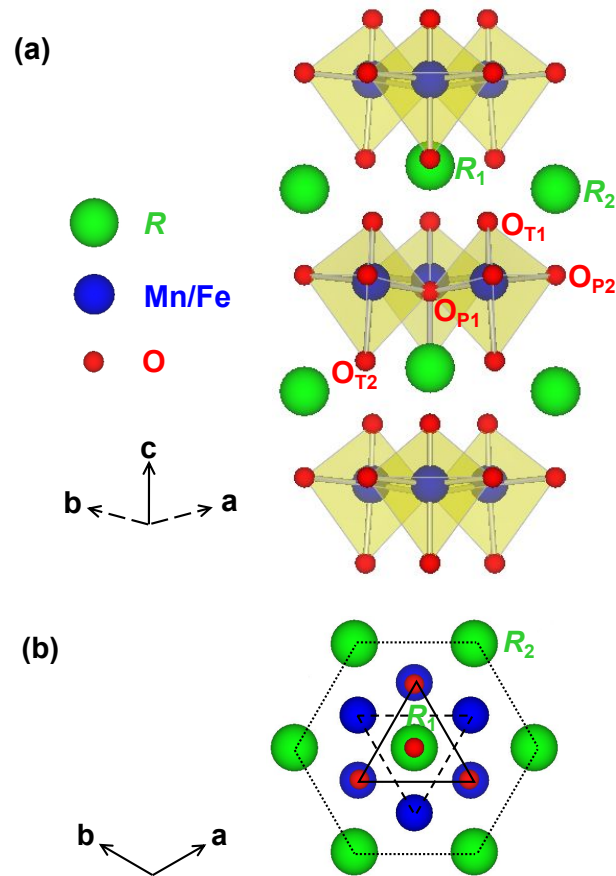


Figure 4.1: Structure of ferroelectric hexagonal $RMnO_3$ or $RFeO_3$ (6 f.u. per primitive cell). (a) Side view from $[110]$. (b) Plan view from $[001]$; dashed (solid) triangle indicates three Mn^{3+} or Fe^{3+} connected via O_{P1} to form a triangular sublattice at $z = 0$ ($z = 1/2$).

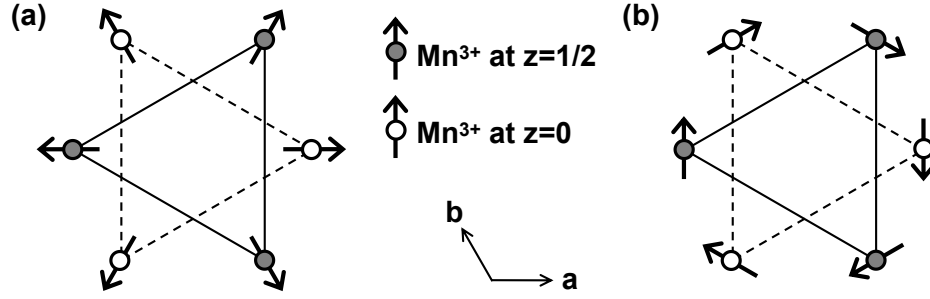


Figure 4.2: Magnetic phases of hexagonal $RMnO_3$ and $RFeO_3$. Mn^{3+} or Fe^{3+} ions form triangular sublattices at $z = 0$ (dash line) and $z = 1/2$ (solid line). (a) A_2 phase with magnetic symmetry $P6_3c'm'$; spins on a given Mn^{3+} layer point all in or all out. (b) A_1 phase with the magnetic symmetry $P6_3cm$, with Mn^{3+} spins pointing tangentially to form a vortex pattern. The A_1 and A_2 phases differ by a 90° global rotation of spins. The B_1 and B_2 phases can be obtained from A_2 and A_1 by reversing the spins on the dashed triangles.

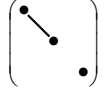
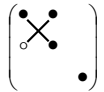
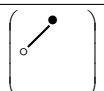
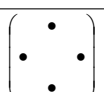
obtained from A_2 and A_1 by reversing the spins on the dashed triangles. Among them, the linear ME effect exists only in A_1 and A_2 phases. From previous experiments, it is known that at zero temperature without a magnetic field, $HoMnO_3$ is in the A_1 phase, while $ErMnO_3$, $YbMnO_3$, and $LuMnO_3$ are not in either A phase. But under a weak magnetic field along the \hat{z} direction, $ErMnO_3$ and $YbMnO_3$ undergo a transition into the A_2 phase [95, 96, 97].

Epitaxially grown thin-film hexagonal $RFeO_3$ has a similar structure as hexagonal $RMnO_3$, with improper ferroelectricity below ~ 1000 K. Replacing Mn^{3+} with Fe^{3+} introduces larger spin moments and stronger super-exchange interactions in the basal plane. It has also been confirmed that below 5 K, the magnetic structure of $LuFeO_3$ is that of the A_2 phase [99].

4.2.2 Symmetry analysis

The purpose of this chapter is to understand the mechanisms that generate large magnetic charges that may in turn induce anomalously large spin-lattice ME effects. Therefore, we focus on the A_1 and A_2 magnetic phases, shown in Fig. 4.2, which allow a linear ME effect to exist. $ErMnO_3$, $YbMnO_3$, and $LuMnO_3$ actually adopt other phases as their ground-state magnetic order at low temperature. Nevertheless, they are included

Table 4.1: Symmetry patterns of Born charges Z^e , magnetic charges Z^m and ME tensors α in $RMnO_3$ and $RFeO_3$. Patterns for Mn, Fe, O_{T1} , and O_{T2} are for atoms lying on an M_y mirror plane. Unless otherwise specified, patterns apply to both A_1 and A_2 phases.

(a)		α (A_2 only) Z^e on R_1 and O_{P1} Z^m on R_1 and O_{P1} (A_2 only)
(b)		Z^e on R_2 and O_{P2} Z^m on R_2 and O_{P2}
(c)		Z^e on Mn, Fe, O_{T1} , and O_{T2} Z^m on Mn, Fe, O_{T1} , and O_{T2} (A_2 only)
(d)		α (A_1 only) Z^m on R_1 and O_{P1} (A_1 only)
(e)		Z^m on Mn, Fe, O_{T1} , and O_{T2} (A_1 only)

- equal component
- equal magnitude with opposite sign

for purposes of comparison when calculating the properties of the hexagonal $RMnO_3$ materials in the A_2 phase. We also study $LuFeO_3$ in the A_2 phase, and for $HoMnO_3$ both the A_1 and A_2 phases are considered.

The A_1 and A_2 phases have the same $P6_3cm$ structural symmetry, so the forms of atomic Born charge tensors in the two phases are the same. The Born charges for R_1 and O_{P1} take the tensor form shown in Table 4.1(a), while those of R_2 and O_{P2} have the symmetry pattern shown in Table 4.1(b). For the Mn, Fe, O_{T1} , and O_{T2} sites lying on a vertical M_y mirror plane, the Born charges are as given in Table 4.1(c); for the partner sites related by rotational symmetry, the tensors also need to be rotated accordingly.

The symmetry forms of atomic magnetic charge tensors can be derived from the on-site magnetic point symmetries. For the A_1 phase, the magnetic space group is $P6_3cm$ and the magnetic charges of R_1 and O_{P1} take the forms given in Table 4.1(d); those for R_2 and O_{P2} have the tensor symmetry shown in Table 4.1(b); and for Mn,

Fe, O_{T1} , and O_{T2} they can be written in the form of Table 4.1(e). For the A_2 phase, the magnetic group is $P6_3c'm'$; all the improper operators are associated with the time-reversal operation, so magnetic charges have the same tensor forms as Born charges.

A symmetry analysis of the structure and the magnetic space group identifies the phonon modes that couple to the electromagnetic field. The infrared (IR)-active phonon modes that couple to the electric field are the longitudinal A_1 modes and the transverse E_1 modes,

$$\Gamma_{\text{IR}} = 10A_1 + 15E_1, \quad (4.1)$$

including the three acoustic modes. Magnetic charges are generated by phonon modes that couple to the magnetic field. In the A_1 phase, the magneto-active phonon modes are the longitudinal A_2 modes and the transverse E_1 modes,

$$\Gamma_{\text{mag}}^{A_1} = 5A_2 + 15E_1, \quad (4.2)$$

where one pair of acoustic E_1 modes are included. In the A_2 phase, on the other hand, the IR- and magneto-active phonon modes are identical, since magnetic and Born charge tensors have the same form in this case.

For the ME effects in the A_1 phase, as the longitudinal IR-active mode (A_1) and magneto-active modes (A_2) are mutually exclusive, the ME tensor does not have a longitudinal component and it takes the form of Table 4.1(d). For the A_2 magnetic phase, the A_1 and E_1 modes are both IR-active and magneto-active, so that the ME tensor has both longitudinal and transverse components and adopts the form shown in Table 4.1(a).

4.3 First-principles methodology

The calculations are performed with plane-wave density functional theory (DFT) implemented in VASP [56] using the generalized-gradient approximation parametrized by the Perdew-Burke-Ernzerhof functional [50]. The ionic core environment is simulated by projector augmented wave pseudopotentials (PAW) [61], and the $4f$ electrons are placed in the PAW core. We use a Hubbard $U = 4.5$ eV and $J = 0.95$ eV on the d orbitals of the Mn and Fe atoms, and the moment on the rare-earth ions are not

considered [35]. The structures are fully relaxed in the DFT+U [54] calculations with their non-collinear spin arrangements in two cases, when SOC is present and when it is absent. In non-collinear magnetization calculations, a high cutoff energy 700 eV and a tight energy error threshold 1.0×10^{-9} eV are necessary to get fully converged magnetic properties. Born charge tensors and the Γ -point force-constant matrices are obtained using linear-response methods in the absence of SOC. The dynamical magnetic charges are computed by applying a uniform Zeeman field [69] to the crystal and computing the resulting forces. Polarization is calculated using the Berry phase formalism [34]. A $4 \times 4 \times 2$ Γ -centered k -point mesh is used in calculations.

4.4 Results and discussion

4.4.1 Born charge and force-constant matrix

The f electrons are not included in our calculations for hexagonal $RMnO_3$ class of materials, so the major differences between compounds result from the variation of the rare-earth radius; the trimerization tends to increase as the radius of the rare-earth element decreases. The calculated Born charge tensors and the eigenvalues of the force-constant matrix for the IR-active modes of $RMnO_3$ and $LuFeO_3$ are listed in Tables 4.2 and 4.3. Because of the similarity in the geometric structures, the dielectric and phonon properties are almost identical in the $RMnO_3$ compounds, regardless of the magnetic order. Only small variations are observed between $LuMnO_3$ and $LuFeO_3$, reflecting the difference in transition-metal atoms.

4.4.2 Magnetization and magnetic charge

In the A_2 phase, the trimerization induces not only an electric polarization, but also a weak ferromagnetism in the \hat{z} direction resulting from a SOC-induced tilting of Mn^{3+} or Fe^{3+} spin moments. The net magnetizations in the 30-atom unit cell for A_2 -phase $HoMnO_3$, $ErMnO_3$, $YbMnO_3$, and $LuMnO_3$ are 0.309, 0.303, 0.292, and $0.268 \mu_B$, respectively. These magnetic moments are found to depend almost linearly on the tilting angle of the MnO_5 bipyramids, which takes values of 5.03° , 5.07° , 5.16° , and

Table 4.2: Atomic Born charge tensors Z^e (in units of $|e|$) for $RMnO_3$ and $LuFeO_3$ in the A_2 phase. TM = Mn, Fe.

	HoMnO ₃	ErMnO ₃	YbMnO ₃	LuMnO ₃	LuFeO ₃
$Z_{xx}^e(R_1)$	3.69	3.67	3.62	3.61	3.79
$Z_{zz}^e(R_1)$	4.16	4.15	4.11	4.12	3.94
$Z_{xx}^e(R_2)$	3.76	3.73	3.67	3.66	3.84
$Z_{yx}^e(R_2)$	0.13	0.13	0.13	0.13	0.15
$Z_{zz}^e(R_2)$	4.07	4.05	4.00	3.96	3.88
$Z_{xx}^e(TM)$	3.16	3.17	3.17	3.17	2.96
$Z_{zx}^e(TM)$	0.41	0.42	0.43	0.44	0.21
$Z_{yy}^e(TM)$	3.25	3.25	3.26	3.26	3.01
$Z_{xz}^e(TM)$	0.07	0.07	0.07	0.07	-0.02
$Z_{zz}^e(TM)$	4.02	4.01	3.97	3.95	4.16
$Z_{xx}^e(OT1)$	-1.95	-1.94	-1.92	-1.92	-2.19
$Z_{zx}^e(OT1)$	0.24	0.24	0.24	0.25	0.25
$Z_{yy}^e(OT1)$	-2.05	-2.03	-2.00	-2.00	-2.28
$Z_{xz}^e(OT1)$	0.19	0.19	0.19	0.19	0.11
$Z_{zz}^e(OT1)$	-3.24	-3.24	-3.20	-3.19	-3.21
$Z_{xx}^e(OT2)$	-1.95	-1.93	-1.91	-1.90	-2.15
$Z_{zx}^e(OT2)$	-0.20	-0.20	-0.20	-0.20	-0.19
$Z_{yy}^e(OT2)$	-1.88	-1.87	-1.85	-1.85	-2.13
$Z_{xz}^e(OT2)$	-0.18	-0.18	-0.18	-0.18	-0.11
$Z_{zz}^e(OT2)$	-3.38	-3.38	-3.34	-3.33	-3.30
$Z_{xx}^e(OP1)$	-3.01	-3.01	-3.01	-3.00	-2.40
$Z_{zz}^e(OP1)$	-1.58	-1.57	-1.54	-1.54	-1.61
$Z_{xx}^e(OP2)$	-3.05	-3.05	-3.06	-3.05	-2.45
$Z_{yx}^e(OP2)$	-0.03	-0.03	-0.03	-0.03	-0.02
$Z_{zz}^e(OP2)$	-1.47	-1.46	-1.43	-1.43	-1.52

Table 4.3: Eigenvalues of the force-constants matrix ($\text{eV}/\text{\AA}^2$) for IR-active modes in $R\text{MnO}_3$ and LuFeO_3 in the A_2 phase, and for HoMnO_3 in the A_1 phase

	HoMnO_3	ErMnO_3	YbMnO_3	LuMnO_3	LuFeO_3
Longitudinal A_1 modes					
	4.23	4.23	4.25	4.24	3.48
	7.11	7.18	7.35	7.44	6.70
	8.14	8.27	8.60	8.74	8.41
	10.77	10.90	11.34	11.51	11.47
	13.69	13.82	13.98	14.01	12.03
	14.85	15.03	15.42	15.60	15.59
	21.32	21.60	22.36	22.66	20.53
	25.44	25.57	25.67	25.87	22.83
	35.99	35.68	35.54	35.82	28.46
Transverse E_1 modes					
	3.23	3.37	3.27	3.32	3.56
	4.22	4.25	4.49	4.68	4.62
	5.96	6.28	6.63	6.73	6.97
	7.59	6.93	7.01	7.35	8.09
	8.41	8.56	8.57	8.63	8.83
	9.29	8.99	9.31	9.56	9.24
	9.65	10.12	10.95	11.36	11.37
	11.23	11.25	12.02	12.46	12.46
	12.57	12.85	12.95	13.02	13.85
	13.29	13.54	13.77	14.09	14.92
	16.41	16.76	16.57	16.49	16.87
	17.49	17.52	17.38	17.37	17.35
	22.79	23.02	23.16	23.36	21.19
	36.18	37.99	37.54	37.75	28.75

Table 4.4: Longitudinal magnetic charge components Z^m ($10^{-3} \mu_B/\text{\AA}$) of $RMnO_3$ and $LuFeO_3$ in the A_2 phase. All components vanish in the absence of SOC.

	HoMnO ₃	ErMnO ₃	YbMnO ₃	LuMnO ₃	LuFeO ₃
$Z_{zz}^m(R_1)$	-50	-53	-53	-67	7
$Z_{zz}^m(R_2)$	14	35	24	16	7
$Z_{xz}^m(TM)$	-92	-86	-61	-67	9
$Z_{zz}^m(TM)$	24	1	6	25	2
$Z_{xz}^m(O_{T1})$	-49	-44	-41	-19	23
$Z_{zz}^m(O_{T1})$	99	81	53	33	22
$Z_{xz}^m(O_{T2})$	-7	-12	-12	-12	0
$Z_{zz}^m(O_{T2})$	-119	-94	-64	-49	-25
$Z_{zz}^m(O_{P1})$	-276	-257	-230	-190	54
$Z_{zz}^m(O_{P2})$	141	140	125	100	-35

5.21° respectively in these four compounds, but in any case the variation is not very large. In contrast, the result for $LuFeO_3$ is $-0.077 \mu_B$, which is much smaller and of opposite sign compared with the $RMnO_3$ materials.

The magnetic charges defined in Eq. (3.8) are found to be more sensitive to the local environment, as the differences between $RMnO_3$ compounds are more significant. we divide the magnetic charge components into two groups that are labeled as “longitudinal” and “transverse” depending on whether the coupling is to magnetic fields along the \hat{z} direction or in the x - y plane, respectively.¹

The longitudinal magnetic charge components are calculated with a magnetic field directed along \hat{z} , which is roughly perpendicular to spin directions. These components are only non-zero when SOC is considered. The scenario here is similar to the case of a transverse magnetic field (H_x or H_y) applied to Cr_2O_3 , since the magnetization is along the z -axis for Cr_2O_3 . It is therefore not surprising to find that the longitudinal magnetic charges of $RMnO_3$ and $LuFeO_3$ in Table 4.4 are comparable to the SOC-induced transverse magnetic charges in Cr_2O_3 in chapter 3 [100]. The longitudinal magnetic charges for O_{P1} and O_{P2} in $LuFeO_3$ are opposite to, and about three times smaller than, the ones in $RMnO_3$. Considering the fact that the trimerization distortion

¹Note that this differs from the usual convention for the magnetic susceptibility, where the distinction between “longitudinal” and “transverse” corresponds to the direction of the applied field relative to the spin direction.

Table 4.5: Transverse magnetic charge components Z^m ($10^{-2} \mu_B/\text{\AA}$) of HoMnO_3 in the A_1 phase, as computed including or excluding SOC.

	Total	No SOC		Total	No SOC
$Z_{yx}^m(\text{Ho}_1)$	-25	-28	$Z_{zy}^m(\text{O}_{T1})$	-188	-230
$Z_{xx}^m(\text{Ho}_2)$	-15	-18	$Z_{yx}^m(\text{O}_{T2})$	-57	-67
$Z_{yx}^m(\text{Ho}_2)$	-1	3	$Z_{xy}^m(\text{O}_{T2})$	-20	-26
$Z_{yx}^m(\text{Mn})$	92	54	$Z_{zy}^m(\text{O}_{T2})$	-192	-231
$Z_{xy}^m(\text{Mn})$	-10	2	$Z_{yx}^m(\text{O}_{P1})$	-483	-551
$Z_{zy}^m(\text{Mn})$	41	48	$Z_{xx}^m(\text{O}_{P2})$	395	461
$Z_{yx}^m(\text{O}_{T1})$	23	28	$Z_{yx}^m(\text{O}_{P2})$	184	253
$Z_{xy}^m(\text{O}_{T1})$	-7	-7			

involves vertical displacements of O_{P1} and O_{P2} , these results explain the differences between RMnO_3 and LuFeO_3 regarding the magnitude and the direction of the weak ferromagnetism.

For the response to transverse magnetic fields, both the field and spins lie in the basal plane, so the dynamical magnetic charges are driven by both SOC and exchange striction. As the exchange-striction strength can exceed that of SOC by orders of magnitude in some materials, it is worthwhile to understand the relative size of these two effects in RMnO_3 and LuFeO_3 . In Tables 4.5 and 4.6, we present the transverse magnetic charges induced with and without SOC in the A_1 and A_2 phases. It is clear that the exchange-striction contributions are an order of magnitude larger for many transverse components. Similarly, the magnetic charges induced by exchange striction are about ten times stronger than the SOC-driven longitudinal ones in Table 4.4 (notice the units in Table 4.4 are different from Tables 4.5 and 4.6). The largest transverse magnetic charge contributions are from exchange striction on O atoms, which mediate the superexchange between Mn atoms. For Mn atoms themselves, on the other hand, the exchange-striction contribution is much weaker, and comparable in strength to the SOC-induced contributions. Since the signs of these two contributions are not correlated, a partial cancellation or even a sign reversal sometimes occurs, as can be seen by inspecting the results for the Mn atoms in Tables 4.5 and 4.6. The transverse magnetic charges on the Mn atoms are thus especially sensitive to SOC.

Table 4.6: Transverse magnetic charge components Z^m ($10^{-2} \mu_B/\text{\AA}$) of $RMnO_3$ and $LuFeO_3$ in the A_2 phase, as computed including or excluding SOC.

	HoMnO ₃		ErMnO ₃		YbMnO ₃		LuMnO ₃		LuFeO ₃	
	Total	No SOC								
$Z_{xx}^m(R_1)$	-23	-24	-21	-22	-37	-40	-42	-35	-36	-52
$Z_{xx}^m(R_2)$	6	-1	6	3	12	9	14	6	15	24
$Z_{yx}^m(R_2)$	16	18	11	12	10	10	8	7	-9	-11
$Z_{xx}^m(TM)$	-2	10	-7	-10	-16	-21	-11	1	-52	-43
$Z_{zx}^m(TM)$	-42	-24	-38	-22	-25	-34	-31	-17	-102	-95
$Z_{yy}^m(TM)$	-5	46	-7	32	-22	27	-32	15	-16	-11
$Z_{xx}^m(OT_1)$	5	5	6	6	12	16	14	11	0	0
$Z_{zx}^m(OT_1)$	191	221	150	154	162	178	150	122	128	105
$Z_{yy}^m(OT_1)$	24	23	22	22	31	33	34	25	15	11
$Z_{xx}^m(OT_2)$	20	23	16	19	19	22	17	12	25	20
$Z_{zx}^m(OT_2)$	195	217	140	161	173	189	166	134	130	110
$Z_{yy}^m(OT_2)$	-59	-61	-48	-46	-57	-60	-57	-45	-41	-42
$Z_{xx}^m(OP_1)$	-445	-510	-392	-422	-532	-602	-564	-499	-665	-609
$Z_{xx}^m(OP_2)$	241	234	215	202	298	299	316	247	388	356
$Z_{yx}^m(OP_2)$	-378	-422	-335	-355	-466	-506	-498	-427	-673	-621

4.4.3 Magnetolectric effect

We calculate the spin-lattice ME couplings from Eq. (3.16) using computed Born charges, force-constant matrices, and magnetic charges. The spin-electronic contributions are calculated based on the $\partial P/\partial H$ version of Eq. (1.5) with the lattice degrees of freedom frozen. The ME tensor components are subdivided into longitudinal and transverse ones based on the direction of magnetic field relative to the hexagonal axis as before, so that the longitudinal (transverse) spin-lattice ME coupling is calculated using the longitudinal (transverse) magnetic charge components. The ME tensor elements allowed by symmetry are the longitudinal α_{zz} and transverse $\alpha_{xx} = \alpha_{yy}$ in the A_2 phase, and only the transverse $\alpha_{yx} = -\alpha_{xy}$ components in the A_1 phase.

In the first part of Table 4.7, the spin-contributed longitudinal ME couplings are shown for $RMnO_3$ and $LuFeO_3$ in the A_2 phase. Comparing the lattice and electronic results, it is found that the longitudinal ME effect from the spin channel is dominated by the spin-lattice contribution. Besides, although the longitudinal magnetic charges

Table 4.7: Computed ME couplings α_{zz} (longitudinal) and α_{xx} and α_{yx} (transverse) for $RMnO_3$ and $LuFeO_3$ (ps/m). Spin-lattice, spin-electronic, and total spin couplings are given as computed with and without SOC.

	Spin-latt.		Spin-elec.		Total spin	
	Total	No SOC	Total	No SOC	Total	No SOC
	α_{zz} in A_2 phase					
HoMnO ₃	-0.27	0	0.06	0	-0.21	0
ErMnO ₃	-0.26	0	0.05	0	-0.21	0
YbMnO ₃	-0.25	0	0.06	0	-0.19	0
LuMnO ₃	-0.19	0	0.00	0	-0.19	0
LuFeO ₃	0.26	0	0.00	0	0.26	0
	α_{xx} in A_2 phase					
HoMnO ₃	-0.99	5.12	4.10	4.83	3.11	9.95
ErMnO ₃	-1.30	2.40	2.56	3.72	1.26	6.12
YbMnO ₃	-2.52	1.20	3.72	4.66	1.20	5.86
LuMnO ₃	-2.60	1.31	3.82	3.50	1.22	4.81
LuFeO ₃	-2.20	-1.57	-0.79	-0.32	-2.99	-1.89
	α_{yx} in A_1 phase					
HoMnO ₃	9.55	4.88	5.24	5.35	14.79	10.23

of $LuFeO_3$ are smaller than for $RMnO_3$, the spin-lattice ME couplings $|\alpha_{zz}|$ in $RMnO_3$ and $LuFeO_3$ are similar, ~ 0.25 ps/m. The results are comparable to those reported for the transverse ME coupling in Cr_2O_3 [74] and for α_{zz} in $ErMnO_3$ [35] in previous first-principles calculations. In the second part of Table 4.7, we present the spin-related transverse ME couplings α_{xx} for $RMnO_3$ and $LuFeO_3$ in the A_2 phase. The same information is presented in graphical form in Fig. 4.3.

It is clear from the comparison between the first and second parts of Table 4.7 that the transverse spin-lattice ME couplings are one order of magnitude larger than the longitudinal ones due to the exchange-striction mechanism. Surprisingly, Fig. 4.3(a) shows that the effect of SOC on the exchange striction is profound, even reversing the sign of spin-lattice ME couplings in $RMnO_3$. This unusual behavior can be traced mainly to two observations about spin-lattice contributions from different IR-active modes in the $RMnO_3$ materials. Firstly, the exchange-striction ME effect is smaller than expected as a result of a large degree of cancellation between the contributions from different transverse IR-active modes. To illustrate this, the mode-by-mode contributions are

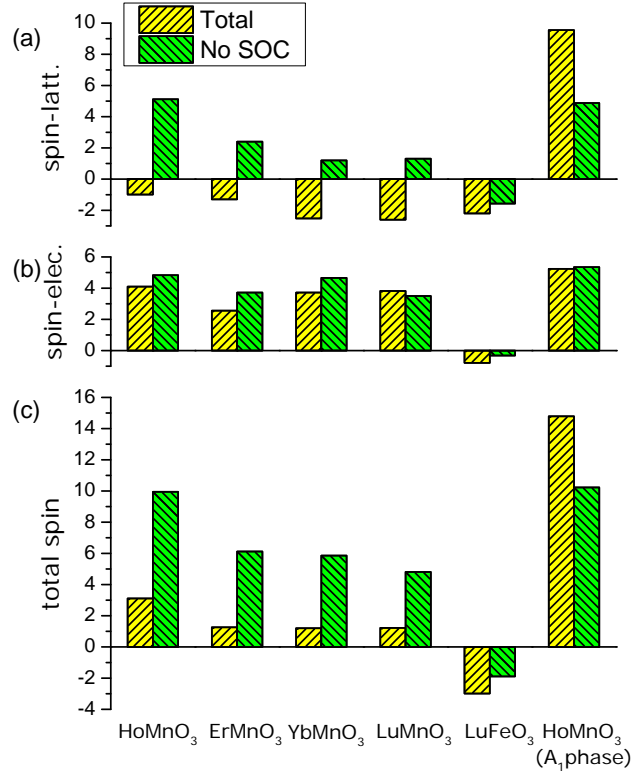


Figure 4.3: Transverse ME couplings α_{xx} for A_2 phase $RMnO_3$ and $LuFeO_3$, and α_{yx} for A_1 phase $HoMnO_3$. (a) Spin-lattice; (b) spin-electronic; and (c) total spin couplings. The unit is ps/m.

presented for a few selected cases in Table 4.8. Secondly, the softest modes are dominated by Mn displacements, precisely those for which SOC has the largest effect on Z^m values, even flipping the sign of some components. In this way, it turns out that SOC can result in large relative changes in the spin-lattice ME couplings. In the case of $LuFeO_3$, the SOC effect on the Z^m values is weak, even for Fe atoms. Thus, the ME coupling of $LuFeO_3$ does not change as dramatically as that of $RMnO_3$ when SOC is included.

From Fig. 4.3(b) it can be seen that the spin-electronic contribution is not negligible in the transverse direction, and it counteracts the ME effects from the spin-lattice channel in A_2 phase $RMnO_3$. The total transverse ME effect is summarized in Fig. 4.3(c). Because of the large SOC effect and the cancellation between the lattice and electronic contributions, the total spin ME coupling α_{xx} is ~ 1.2 ps/m in most A_2 -phase $RMnO_3$

Table 4.8: Transverse ME contributions (ps/m) from IR-active modes for A_2 and A_1 phases of HoMnO_3 and A_2 phase of LuFeO_3 . Results are given in ascending order of force-constant eigenvalues, which are reported in Table 4.3.

A ₂ phase HoMnO ₃		A ₁ phase HoMnO ₃		A ₂ phase LuFeO ₃	
Total	No SOC	Total	No SOC	Total	No SOC
0.01	0.12	0.25	0.18	0.28	0.39
-1.16	2.62	4.98	2.36	-0.54	-0.50
0.66	2.32	3.59	2.37	-1.31	-1.22
-0.51	-0.35	-0.32	-0.48	1.30	1.23
2.79	3.13	2.87	3.33	3.31	3.12
0.35	0.21	0.30	0.30	1.84	1.73
-1.88	-1.85	-1.35	-1.90	-4.43	-4.11
1.13	1.25	1.19	1.38	-2.59	-2.25
-2.96	-3.07	-2.70	-3.40	1.24	1.13
0.01	0.13	0.19	0.06	-1.48	-1.27
0.21	0.24	0.21	0.26	-0.15	-0.14
0.36	0.40	0.34	0.42	0.89	0.83
-0.03	-0.03	-0.03	-0.04	-0.62	-0.55
0.02	0.01	0.03	0.03	0.07	0.03

compounds, except for HoMnO_3 . In HoMnO_3 , the cancellation between the spin-lattice and the spin-electronic ME couplings is the weakest of all the RMnO_3 compounds, resulting in the largest total spin ME response of ~ 3.1 ps/m in the A_2 phase. In LuFeO_3 , the spin-lattice and spin-electronic terms are all smaller than in RMnO_3 . However, the cancellation induced by the SOC perturbation and the spin-electronic contribution is avoided, so that LuFeO_3 has a large total spin ME coupling of ~ -3 ps/m.

The ME results for HoMnO_3 in the A_1 phase are presented in the last line of Table 4.7 and at the last column Fig. 4.3. In principle the ME couplings of HoMnO_3 in the A_1 and A_2 phases should be the same without SOC, as the two phases only differ by a global spin rotation. This is approximately confirmed by a comparison of the corresponding entries for HoMnO_3 in Table 4.7. The ME contribution from exchange striction (i.e., without SOC) is ~ 5 ps/m for both A_2 and A_1 phases. However, when the effect of SOC is included, the spin-lattice contribution is strongly enhanced by another ~ 5 ps/m in the A_1 phase. Furthermore, the spin-electronic ME effect has the same sign as the spin-lattice one, which adds ~ 5 ps/m to the ME coupling. Therefore, the

total spin ME coupling α_{yx} reaches ~ 15 ps/m, and is the largest in all of the $RMnO_3$ and $LuMnO_3$ materials we studied.

4.5 Summary and outlook

In summary, we have studied the spin-related magnetic charges and ME couplings for $HoMnO_3$, $ErMnO_3$, $YbMnO_3$, $LuMnO_3$, and $LuFeO_3$ using first-principles calculations. It has been confirmed that the exchange striction acting on non-collinear spins induces much larger magnetic charges than does SOC acting alone. Nevertheless, the effect of SOC on ME couplings is surprisingly large, rivaling that of exchange striction in many cases. This occurs because the exchange-striction contribution tends to be reduced by cancellations between different IR-active modes, while the SOC contribution is mainly associated with just a few low-frequency modes with large Mn displacements. It has also been found that the $RMnO_3$ materials have spin-electronic ME couplings comparable to the spin-lattice ones. Among the $RMnO_3$ and $LuFeO_3$ materials we studied, the A_1 phase of $HoMnO_3$ is the most promising ME material, with the largest ME coupling of ~ 15 ps/m. Extrapolating the conclusions to other hexagonal $RMnO_3$ and $RFeO_3$ compounds that are not included in our calculations, we predict that the A_2 phase is more promising for the ferrites, while the A_1 phase has a stronger ME coupling for the manganites.

Chapter 5

Ferroelectricity in corundum derivatives

5.1 Introduction

Ferroelectricity requires a material to have a spontaneous electric polarization that can be reversed by an external electric field. The search for new ferroelectric (FE) materials holds promise for broadening our understanding of FE mechanisms and extending the range of applications of FE materials.

The most intensively studied family of FE oxides is that of the perovskite oxides [101, 102] such as BaTiO_3 . Perovskite oxides have the chemical formula ABO_3 with the A cation much larger than the B cation. The structure of a cubic perovskite is shown in Fig. 5.1(a). The B cation has a 6-fold oxygen coordination which forms a BO_6 oxygen octahedron, and the perovskite structure is made up of these corner sharing octahedra. The A cation occupies the hole of BO_6 octahedra and has a 12-fold oxygen coordination. If ions are stacked ideally in the cubic structure, the radius of A cation (r_A), B cation (r_B) and O anion (r_O) satisfy $\tau = (r_A + r_O)/\sqrt{2}(r_B + r_O) = 1$, and the ratio τ is called the ‘‘Goldschmidt’s Tolerance Factor’’ [103]. The tolerance factor is an indicator for the stability and distortion of perovskites, and if τ is not close to 1, the ideal cubic structure is distorted to a lower symmetry. For example, in the case of a smaller τ , the A cation is not large enough to fit into the interstices, thus BO_6 octahedra rotations may develop to reduce the A -O distance and optimize the coordination environment of the A cation [104]. The FE distortion also lowers the symmetry and it is usually driven by B -site off-centering which typically requires an empty d shell on the B cation. Therefore, most FE perovskite oxides does not have magnetism [105]. Recently, rocksalt-ordered $A_2BB'O_6$ (and more complex $AA'BB'O_6$ materials) double perovskites as sketched in Fig. 5.1(b) have also attracted great interest [106, 107].

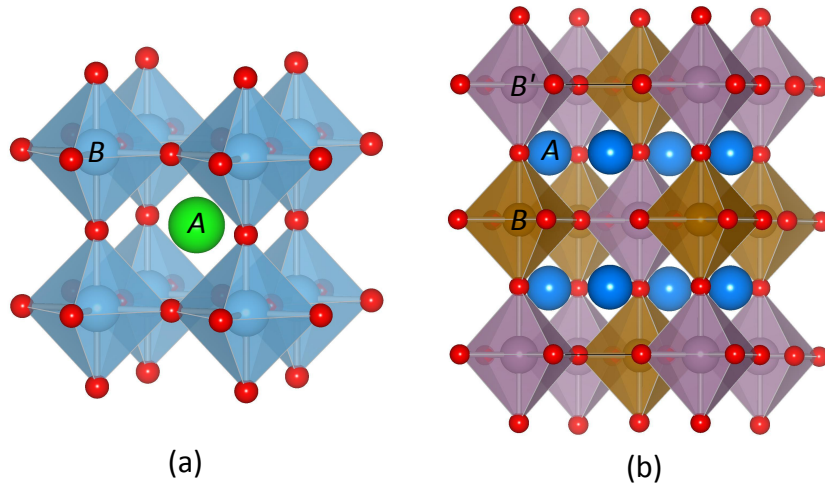


Figure 5.1: Structures of (a) a cubic perovskite ABO_3 and (b) a double perovskite $A_2BB'O_6$.

The corundum derivatives ABO_3 and $A_2BB'O_6$ make up a family of oxides that can be derived from the corundum structure with cation ordering as shown in Fig. 5.2. Some corundum derivatives are discovered in nature [108], and recently, more corundum derivatives become available as metastable states through high-pressure synthesis [109, 110, 111, 112, 113, 114, 115, 116, 117, 118, 119, 44]. Previous experimental and theoretical studies suggest that most corundum derivatives are polar and exhibit large polarization [120, 110, 121, 122, 114, 123], thus can potentially be new FE oxides similar to the well-known FE LiNbO_3 (LNO) and LiTaO_3 .

Despite the similar chemical formula, corundum derivatives are different from perovskites in many aspects. In corundum derivatives the A cation and B cation are comparable in size, so they have small tolerance factors ($\tau < 0.8$) and large BO_6 octahedra rotations. The large rotation changes the local environment of A cation from 12-fold coordination to 6-fold coordination which forms a distorted oxygen octahedron as shown in Fig. 5.2. The rotation is so prominent that the high-symmetry reference structure for corundum derivatives is rhombohedral instead of cubic, which is the high-temperature paraelectric structure of perovskites. The polarization reversal mechanisms are also distinct. In corundum derivatives, the polarization reversal is driven by the small A or B cations migrating between oxygen octahedra [124, 125], so that d^0 configuration

is not required. This is in contrast to the off-centering displacement of d^0 B cations in the oxygen octahedra in most perovskites. Therefore, corundum derivatives are also good candidates for multiferroics and magnetoelectric effect [121].

Huge numbers of potential combinations of A , B and B' cations in the ABO_3 and $A_2BB'O_6$ corundum-derivative family opens the possibility to achieve ferroelectricity, multiferroicity and even more desirable properties. In this chapter, we focus on the polarization switching process of corundum derivatives, which is the crucial feature that distinguishes FEs from polar materials. we use first-principles density functional methods to systematically study polar structures and coherent FE reversal paths for a variety of corundum derivatives. we first categorize corundum derivatives into four types and show that only two of these allow for the possibility of FE reversal. Then a systematic method to analyze the coherent FE barrier and energy profile using structural constraints are proposed and the method is applied to several corundum derivatives. Furthermore, we identify several empirical measures that can provide a rule of thumb for estimating the energy barriers. Finally, the possibilities of including magnetism and hyperferroelectricity in corundum derivatives are discussed. These results lead us to the prediction of several potentially new FEs.

5.2 Preliminary

5.2.1 Structure

Corundum derivatives ABO_3 and $A_2BB'O_6$ can be derived from the corundum structure X_2O_3 with cation ordering as shown in Fig. 5.2. In the 10-atom rhombohedral unit cell, the cations are spaced along the three-fold rotation axis and each one is surrounded by a distorted oxygen octahedron. Two thirds of the oxygen octahedra are filled with cations, while one third of them are cation-vacant.

Based on the combinations and arrangements of cations, corundum derivatives can be classified into four types with notations as follows. An oxygen octahedron with an A or B cation inside is written as “ A ” or “ B ”, and if an oxygen octahedron is cation-vacant, the octahedron is denoted by “ $-$ ”. This notation is then used to represent

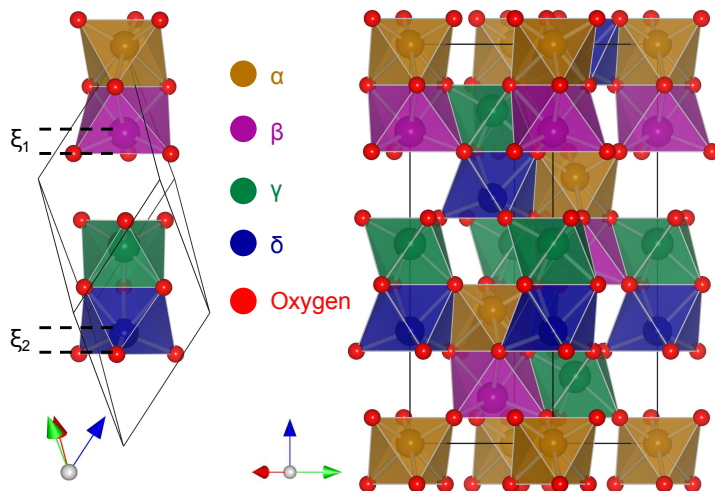


Figure 5.2: Structure of corundum derivatives. The unit cell in the rhombohedral setting is shown at the left; an enlarged hexagonal-setting view is shown at right. The cations α , β , γ , and δ are all identical in the X_2O_3 corundum structure. For the LNO-type ABO_3 , $\beta = \delta = A$, $\alpha = \gamma = B$; for the ilmenite ABO_3 , $\beta = \gamma = A$, $\alpha = \delta = B$; for the ordered-LNO $A_2BB'O_6$, $\beta = \delta = A$, $\gamma = B$, $\alpha = B'$; for the ordered-ilmenite $A_2BB'O_6$, $\beta = \gamma = A$, $\delta = B$, $\alpha = B'$. At left, ξ_1 (or ξ_2) is the distance between β (or δ) and the oxygen plane that it penetrates during the polarization reversal.

the column of six face-sharing oxygen octahedra in the unit cell for each of the four different types of corundum derivatives. Thus, the LNO-type ABO_3 is $AB-AB-$, the ilmenite ABO_3 is $AB-BA-$, the ordered-LNO $A_2BB'O_6$ is $AB-AB'-$, and the ordered-ilmenite $A_2BB'O_6$ is $AB-B'A-$. Other combinations, such as $AA-BB-$, are connected to the four existing types as explained in the next section.

5.2.2 Coherent ferroelectric reversal

Experimentally, the FE polarization reversal process is a complicated one that typically proceeds by nucleation and motion of domain walls, involving both intrinsic atomic motion and extrinsic pinning by defects. In this chapter, we focus only on the coherent FE domain reversal, in which every unit cell undergoes the polarization reversal simultaneously. This coherent reversal process is clearly oversimplified and the barrier energy of the coherent path is not equivalent to the coercive electric field in the FE hysteresis measurement. However, previous studies of perovskite oxides have shown that the

Table 5.1: Corundum-derived structures before and after polarization reversal.

	Before	After
LNO-type	$AB-AB-$	$-BA-BA$
Ilmenite	$AB-BA-$	$-BB-AA$
Ordered-LNO	$AB-AB'-$	$-BA-B'A$
Ordered ilmenite	$AB-B'A-$	$-BB'-AA$

coherent barrier provides a figure of merit that is often a useful indicator of the real barrier to polarization reversal. For example, the well-known FE perovskite PbTiO_3 has a coherent barrier around 0.2 eV per five-atom cell [101], hence perovskite oxides with coherent barriers lower than this is considered likely to be FE.

The atomic origin of ferroelectricity in LiNbO_3 is well-understood [124, 125]. In LiNbO_3 the polarization reversal is driven by an infrared (IR)-active mode that is associated with the motion of Li cations along the rhombohedral axis. In the reversal process, each Li cation penetrates through an oxygen plane and migrates into an adjacent unoccupied oxygen octahedron. In our notation, the polarization reversal process interchanges Li with $-$, so that the polar structure changes from $\text{LiNb}-\text{LiNb}-$ to its inversion image $-\text{NbLi}-\text{NbLi}$.

For all types of polar corundum derivatives, we assume that their polarization reversal mechanisms are similar to that of LiNbO_3 , i.e., that the reversal process interchanges A or B with $-$. The structures before and after this process are listed in Table 5.1. Under such an operation, the LNO-type structure is transformed into its own inversion-reversed image, which is a typical FE behavior. The same is true for the ordered-LNO structure. By contrast, the ilmenite-type $AB-BA-$ is transformed into $BB-AA-$, and the ordered-ilmenite $AB-B'A-$ into $BB'-AA-$. These structures are not inversion-equivalent to the starting structures. Moreover, they exhibit face-sharing A -containing octahedra, making them relatively unfavorable energetically. Additionally, both the ilmenite structure and its switched partner are centrosymmetric. For these reasons, ilmenite and ordered-ilmenite structures are excluded from our further consideration as FE candidates.

5.2.3 Energy profile calculation

For the LNO-type and the ordered-LNO FE candidates, we firstly analyze the symmetry of the reversal path. The ground state symmetry is $R3c$ for LNO-type materials, and $R3$ for ordered-LNO ones, but the symmetry of the reversal path is not straightforward. For the coherent reversal, we assume that the three-fold rotation is always preserved, so that the symmetry of the path can only be $R3c$ or $R3$ for the LNO-type case, and $R3$ for the ordered-LNO case. If the structure acquires an inversion center at the midpoint of the path when the polarization is zero ($R\bar{3}c$ or $R\bar{3}$ for the two cases respectively), the energy profile would be symmetric. If the inversion symmetry at the midpoint is broken, as for example by magnetic orders, the energy profile would be asymmetric.

Different methods are adopted to calculate the energy profile of the FE reversal based on the symmetry of the reversal path. In the case when the inversion symmetry is present at the midpoint structure, the polarization reversal can be analyzed in terms of an unstable IR-active phonon mode at the high-symmetry midpoint. In general, even if the midpoint is not in a high-symmetry reference structure, the motion of the small A cations is responsible for the polarization reversal. Therefore, we define ξ_1 (ξ_2) to be the distance between the first (second) A cation and the oxygen plane that it penetrates as this A cation moves along its path, as illustrated in Fig. 5.2. Then $\xi_1 + \xi_2$ is adopted as a “reaction coordinate” to describe the reversal. Finally, we use either the unstable IR-active mode at the midpoint (for the high-symmetry case) or $\xi = \xi_1 + \xi_2$ (otherwise) as a structural constraint, and relax all other internal structural degrees of freedom while stepping through a sequence of values of this constraint. This gives the energy profile along the path, from which the energy barrier is obtained by inspection.

5.3 First-principles methodology

The calculations are performed with plane-wave density functional theory (DFT) implemented in VASP [56]. The exchange-correlation functional that we use is PBEsol, a revised Perdew-Burke-Ernzerhof generalized-gradient approximation that improves

equilibrium properties of densely-packed solids [51]. The ionic core environment is simulated by projector augmented-wave pseudopotentials (PAW) [61]. For transition metal elements Mn and Fe, a Hubbard $U = 4.2$ eV is used on the $3d$ orbitals [53, 118]. For the Os $5d$ orbital, a Hubbard $U = 1.4$ eV is used [123]. The magnetic moments are collinear and spin-orbit coupling is neglected. The cutoff energy for all calculations is 550 eV. The energy error threshold varied slightly in different calculations, but an accuracy between 1.0×10^{-5} and 1.0×10^{-7} eV is achieved in all calculations. The forces are reduced below 0.001 eV/Å for calculations of structural relaxation. A $6 \times 6 \times 6$ Monkhorst-Pack k -mesh is used in calculations. Linear-response methods are used to calculate the Γ -point force-constant matrices. The spontaneous polarization is calculated using the Berry phase formalism [34].

5.4 Results and discussion

In this section, we apply the method introduced in previous sections to fully analyze the coherent FE reversal path of the LNO-type corundum derivatives LiNbO_3 , LiTaO_3 , ZnSnO_3 , FeTiO_3 , and MnTiO_3 , and the ordered-LNO corundum derivatives $\text{Li}_2\text{ZrTeO}_6$, $\text{Li}_2\text{HfTeO}_6$, Mn_2FeWO_6 , Mn_3WO_6 and $\text{Zn}_2\text{FeOsO}_6$. Among these materials, LiNbO_3 and LiTaO_3 are well-known ferroelectrics [108], so they are used as references for comparison. The high-pressure synthesized ZnSnO_3 thin film [120] and FeTiO_3 polycrystal [110] have also been experimentally confirmed to be FE, while experimental results for bulk crystals are absent. Similar to FeTiO_3 , MnTiO_3 has also been predicted to be FE from theoretical calculations [121], but the experimental evidence is lacking. Ordered-LNO $\text{Li}_2\text{ZrTeO}_6$ and $\text{Li}_2\text{HfTeO}_6$ are stabilized at 700° [115] without detailed investigation of FE properties. Mn_2FeWO_6 [44] and Mn_3WO_6 [126] are stabilized in high pressure, but FE properties are still under experimental investigation. $\text{Zn}_2\text{FeOsO}_6$ is predicted to be FE from a previous theoretical calculation [123], but the compound has not been synthesized yet.

Table 5.2: Rhombohedral structural parameters of LNO-type ABO_3 corundum derivatives $LiNbO_3$, $LiTaO_3$, $ZnSnO_3$, $FeTiO_3$ and $MnTiO_3$ from our first-principles calculations and experiments [111, 127, 128, 129, 130]. The Wyckoff positions are 2a for A and B cations, and 6c for oxygen anions (note that $A_x = A_y = A_z$ and $B_x = B_y = B_z$). The origin is defined by setting the Wyckoff position B_x to zero.

	$LiNbO_3$		$LiTaO_3$		$ZnSnO_3$		$FeTiO_3$		$MnTiO_3$	
	Calc.	Exp.								
Lattice constants										
a (Å)	5.486	5.494	5.476	5.473	5.584	5.569	5.434	5.458	5.481	5.455
α (°)	56.0	55.9	56.2	56.2	56.5	56.4	56.5	56.0	56.6	56.8
Wyckoff positions										
A_x	0.282	0.280	0.284	0.291	0.283	0.286	0.290	0.287	0.279	0.276
B_x	0.000	0.000	0.000	0.000	0.000	0.000	0.000	0.000	0.000	0.000
O_x	0.360	0.359	0.365	0.368	0.392	0.381	0.364	0.364	0.348	0.345
O_y	0.719	0.720	0.726	0.732	0.709	0.721	0.721	0.720	0.721	0.731
O_z	0.112	0.111	0.119	0.124	0.104	0.111	0.104	0.109	0.120	0.128

Table 5.3: Rhombohedral structure parameters of ordered-LNO $A_2BB'O_6$ corundum derivatives Li_2ZrTeO_6 , Li_2HfTeO_6 , Mn_2FeWO_6 , Mn_3WO_6 and Zn_2FeOsO_6 from our first-principles calculations and experiments [115, 44]. Wyckoff positions are 1a for A_1 , A_2 , B and B' cations, and 3b for O_1 and O_2 anions. The origin is defined by setting the Wyckoff position B'_x to zero. For ordered-LNO Li_2HfTeO_6 and Zn_2FeOsO_6 , no experimental results are available. Magnetic orders used in the calculation for Mn_2FeWO_6 , Mn_3WO_6 , and Zn_2FeOsO_6 are also indicated by “Mag”.

	Li_2ZrTeO_6		Li_2HfTeO_6		Mn_2FeWO_6		Mn_3WO_6		Zn_2FeOsO_6	
	Calc.	Exp.	Calc.	Calc.	Exp.	Calc.	Exp.	Calc.	Calc.	
Mag	—	—	—		<i>udu</i>	NA	<i>udu</i>	<i>uud</i>	NA	FiM
Lattice constants										
a (Å)	5.526	5.497	5.480		5.531	5.562	5.607	5.613	5.605	5.410
α (°)	56.1	56.1	56.3		57.3	56.9	56.7	56.6	56.7	56.7
Wyckoff positions										
A_{1x}	0.291	0.298	0.289		0.286	0.278	0.287	0.283	0.283	0.284
A_{2x}	0.781	0.768	0.781		0.787	0.785	0.790	0.779	0.788	0.783
B_x	0.504	0.507	0.504		0.506	0.493	0.508	0.493	0.510	0.504
B'_x	0.000	0.000	0.000		0.000	0.000	0.000	0.000	0.000	0.000
O_{1x}	0.366	0.390	0.366		0.356	0.347	0.356	0.384	0.351	0.376
O_{1y}	0.745	0.729	0.743		0.744	0.745	0.742	0.693	0.744	0.732
O_{1z}	0.111	0.133	0.115		0.109	0.102	0.102	0.124	0.104	0.114
O_{2x}	0.628	0.621	0.629		0.632	0.631	0.631	0.595	0.631	0.619
O_{2y}	0.219	0.235	0.222		0.207	0.197	0.199	0.234	0.190	0.223
O_{2z}	0.895	0.893	0.889		0.884	0.885	0.893	0.848	0.901	0.885

Table 5.4: Oxidation states of the LNO-type ABO_3 and the ordered-LNO $A_2BB'O_6$ corundum derivatives. The oxidation state of O ion is -2 in all materials.

LNO-type	A	B	Ordered LNO	A	B	B'
LiNbO ₃	+1	+5	Li ₂ ZrTeO ₆	+1	+4	+6
LiTaO ₃	+1	+5	Li ₂ HfTeO ₆	+1	+4	+6
ZnSnO ₃	+2	+4	Mn ₂ FeWO ₆	+2	+2	+6
FeTiO ₃	+2	+4	Mn ₃ WO ₆	+2	+2	+6
MnTiO ₃	+2	+4	Zn ₂ FeOsO ₆	+2	+3	+5

5.4.1 Ground state structure and magnetic order

The FE properties are sensitive to atomic displacements and strain, so it is essential to start calculations with accurate structural parameters. The lattice constants and Wyckoff positions obtained from our calculations are summarized in Tables 5.2 and 5.3 with experimental results provided for reference and the calculated structural parameters are very close to the experimental results. The oxidation states, obtained by rounding the integrated charge around each cation, are also displayed in Table 5.4 and are consistent with experimental observations.

The on-site spin moments are investigated for FeTiO₃, MnTiO₃, Mn₂FeWO₆, Mn₃WO₆, and Zn₂FeOsO₆ by integrating the spin density inside the PAW sphere. DFT+ U calculations predict that the magnetic moment is about $3.7 \mu_B$ on each Fe²⁺, $4.6 \mu_B$ on each Mn²⁺, and $4.2 \mu_B$ on Fe³⁺. These results are in agreement with the high-spin d^6 state of Fe²⁺ and the high-spin d^5 configuration of Fe³⁺ and Mn²⁺. The magnetic moment on Os⁵⁺ is $2.1 \mu_B$ from our calculation, which is consistent with the high-spin d^3 state after taking into account the screening of the Os moment arising from the hybridization between Os $5d$ and O $2p$ orbitals.

The energy of different magnetic orders that preserve the periodicity of the rhombohedral unit cell is also studied. Calculation results suggest that the ground-state magnetic order is antiferromagnetic (AFM) for FeTiO₃ and MnTiO₃ and ferrimagnetic (FiM) for Zn₂FeOsO₆. To investigate magnetic structures of Mn₂FeWO₆ and Mn₃WO₆, four different types of unit cell are considered in the calculation. We adopt a notation like “ udu ” to describe the possible spin structure on the three cations excepting W.

Table 5.5: Magnetic energy of different magnetic states relative to the lowest-energy state in Mn_2FeWO_6 and Mn_3WO_6 , in units of meV per unit cell.

	Energy			
	<i>uuu</i>	<i>uud</i>	<i>udd</i>	<i>udu</i>
Mn_2FeWO_6	90.2	32.1	39.5	0.0
Mn_3WO_6	101.8	1.0	19.2	0.0

Here “*u*” is spin-up, “*d*” is spin-down, and the spins are given on cations A_1 , A_2 and B in that order, where A_1 and A_2 are face-sharing with B' and B cations, respectively. (Note that A_1 , A_2 and B correspond to cations β , δ and γ , respectively, in Fig. 5.2.) The four possible states (not counting those that are trivially related by a global spin reversal) are *uuu*, *uud*, *udu*, and *udd*. The energy of each fully-relaxed magnetic structure is listed in Table 5.5. Of those, the most stable state for both Mn_2FeWO_6 and Mn_3WO_6 is *udu*. However, for Mn_3WO_6 , the energy difference between the *uud* and *udu* states is tiny, so both magnetic states are considered in the study of polarization reversal.

The magnetic ground states of Mn_2FeWO_6 and Mn_3WO_6 can be understood by analyzing the superexchange interactions between the spins of A_1 , A_2 and B cations. The magnetic moments are coupled through the oxygen octahedra, and there are three independent coupling constants. The moments on A_2 and B sites are coupled through face-sharing and corner-sharing oxygen octahedra with strength J_{A_2B} ; the A_1 and B moments are coupled through edge-sharing octahedra with strength J_{A_1B} ; and the A_1 and A_2 moments are coupled through corner-sharing octahedra with strength $J_{A_1A_2}$. Then the magnetic energy E_{mag} can be written as

$$E_{\text{mag}} = J_{A_1B} \hat{S}_{A_1} \cdot \hat{S}_B + J_{A_2B} \hat{S}_{A_2} \cdot \hat{S}_B + J_{A_1A_2} \hat{S}_{A_1} \cdot \hat{S}_{A_2}, \quad (5.1)$$

where \hat{S} represent the spin direction on each site. Substituting the energy of different magnetic orders in Table 5.5 into Eq.(5.1), it is discovered that the coupling constants are all positive. This result means that the three magnetic moments all favor AFM coupling. However, it is impossible to make three collinear spins couple antiferromagnetically, and this frustration implies that one pair must be ferromagnetically coupled.

Table 5.6: Relative spin direction between different magnetic ions in Mn_2FeWO_6 and Mn_3WO_6 . Here “FM” means ferromagnetic.

	uuu	uud	udd	udu
A_1 and B	FM	AFM	AFM	FM
A_2 and B	FM	AFM	FM	AFM
A_1 and A_2	FM	FM	AFM	AFM

In Table 5.6, we list the relative spin orientations of the magnetic ions. Since the face-sharing coupling J_{A_2B} is the strongest, it is not surprising that the A_2 and B moments couple antiferromagnetically; the competition between J_{A_1B} and $J_{A_1A_2}$ then determines the magnetic ground state. In Mn_3WO_6 , these two couplings are comparable, so the energy difference between the uud and udu states is tiny. In the case of Mn_2FeWO_6 , the magnetic moment on the B cation is smaller, so the coupling J_{A_1B} is weaker than $J_{A_1A_2}$. Therefore, the lowest-energy state is udu .

5.4.2 Symmetry of the reversal path

For the LNO-type materials, the simplest possible reversal path would be one in which the two A cations move synchronously, so that $\xi_1 = \xi_2$ everywhere along the path. In this case the symmetry along the path is $\text{R}\bar{3}\text{c}$, except at the midpoint where there is an inversion center and the symmetry becomes $\text{R}\bar{3}\text{c}$. Another possibility is that the cations move sequentially, one after the other, so that $\xi_1 \neq \xi_2$ for at least part of the path. In this case the symmetry is $\text{R}\bar{3}$ except at the $\text{R}\bar{3}$ midpoint. In order to find out which scenario occurs, we calculate the energy of the midpoint structures with symmetry $\text{R}\bar{3}\text{c}$ and $\text{R}\bar{3}$, respectively; the results are shown in Table 5.7. For all LNO-type materials in Table 5.7, the $\text{R}\bar{3}$ midpoint structure is energetically favored, which implies that the reversal occurs via the lower-symmetry $\text{R}\bar{3} \rightarrow \text{R}\bar{3} \rightarrow \text{R}\bar{3}$ scenario, at least in the central portion of the path. Considering the fact that the high-temperature paraelectric phase of LiNbO_3 has the symmetry $\text{R}\bar{3}\text{c}$ [124, 125], this striking result demonstrates that the midpoint of FE reversal path in the LNO-type FE materials is *not* identified with the paraelectric structure, but instead has lower symmetry.

Table 5.7: Energy and unstable phonon modes at the midpoint structure of LiNbO₃, LiTaO₃, ZnSnO₃, FeTiO₃ and MnTiO₃ with symmetry R $\bar{3}$ c and R $\bar{3}$. The energy of the ground-state structure is set to be zero as reference and the unit is meV per unit cell. The imaginary frequency of the unstable phonon is given in units of cm⁻¹.

	Energy		Unstable modes		
	R $\bar{3}$ c	R $\bar{3}$	R $\bar{3}$ c		R $\bar{3}$
			A _{2u}	A _{2g}	A _u
LiNbO ₃	303	259	216 <i>i</i>	123 <i>i</i>	158 <i>i</i>
LiTaO ₃	163	129	178 <i>i</i>	116 <i>i</i>	24
ZnSnO ₃	255	241	93 <i>i</i>	30 <i>i</i>	47 <i>i</i>
FeTiO ₃	1014	735	195 <i>i</i>	75 <i>i</i>	—
MnTiO ₃	550	468	177 <i>i</i>	73 <i>i</i>	114 <i>i</i>

The energy differences between R $\bar{3}$ c and R $\bar{3}$ structures can be explained by comparing their unstable phonons, for which the frequencies are listed in Table 5.7. At R $\bar{3}$ c symmetry, all LNO-type candidates have *two* unstable modes along the rhombohedral axis direction, namely one A_{2u} and one A_{2g} mode. The A_{2u} mode is IR-active, and it describes the synchronous movement of *A* cations. The non-polar A_{2g} mode, however, is related to the out-of-phase movement of the two *A* cations. Comparing the unstable modes in the R $\bar{3}$ c and R $\bar{3}$ structures, it is found that the unstable non-polar mode is absent in the R $\bar{3}$ structure. Therefore, the unstable A_{2g} mode is responsible for the energy reduction in going from the R $\bar{3}$ c to the R $\bar{3}$ structure. In addition, an unstable E_u mode is found in LiNbO₃ and FeTiO₃ for both the R $\bar{3}$ c and R $\bar{3}$ structures. As the three-fold rotational symmetry is preserved in our calculation, the E_u modes are not allowed to relax and further lower the energy.

For the ordered-LNO materials, since the two *A* cations are not related by any symmetry even in the ground state, the two *A* cations move sequentially so that $\xi_1 \neq \xi_2$. Therefore, the reversal path adopts the R3 symmetry, except at the R $\bar{3}$ midpoint. The only exception in our calculations is the case of the *udu* magnetic state in Mn₂FeWO₆ and Mn₃WO₆, where the magnetic order break inversion symmetry so that the midpoint structure slightly deviates from R $\bar{3}$ to R3. Leaving aside this small distortion, the midpoint structures of the LNO-type and the ordered-LNO paths have the same structural symmetry, even though the ordered-LNO compounds have lower symmetry

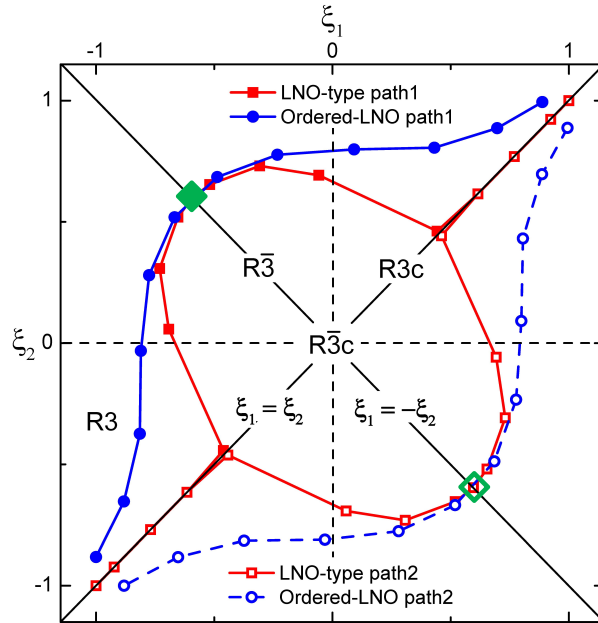


Figure 5.3: Movements of A cations in LNO-type (red, here LiNbO_3) and ordered-LNO (blue, here Mn_2FeWO_6) corundum derivatives along the polarization reversal path. ξ_1 and ξ_2 are the distances from A atoms to the oxygen planes that are penetrated during the polarization reversal, here rescaled to a range between -1 and 1 . The symmetry at an arbitrary (ξ_1, ξ_2) point is $R\bar{3}$; on the $\xi_1 = \xi_2$ and $\xi_1 = -\xi_2$ diagonals it is raised to $R3c$ and $R\bar{3}$, respectively; and at the origin ($\xi_1 = \xi_2 = 0$) it reaches $R\bar{3}c$. Green diamonds denote the midpoint structure in the parameter space. In the LNO-type case “path1” and “path2” (filled and open red square symbols) are equivalent and equally probable, while the ordered-LNO system deterministically follows “path1” (full blue line), which becomes “path2” (dashed blue) under a relabeling $\xi_1 \leftrightarrow \xi_2$.

in their ground state.

The sequence of movements of the A cations along the FE reversal path is illustrated in Fig 5.4, and described quantitatively using our computed results for LiNbO_3 and Mn_2FeWO_6 as paradigmatic examples in Fig. 5.3. The “Before” and “After” structures in Fig. 5.4 correspond to the points at the top right and bottom left corners of Fig. 5.3, respectively. For the LNO-type case, the ideal $R\bar{3}c$ “Midpoint” structure would correspond to the origin on the plot, but the reversal path does not pass through this point because of an unstable A_{2g} mode along the $\xi_1 = -\xi_2$ direction. The “bubble” in the center confirms the significant effect of the unstable A_{2g} mode. The “Midpoint” in

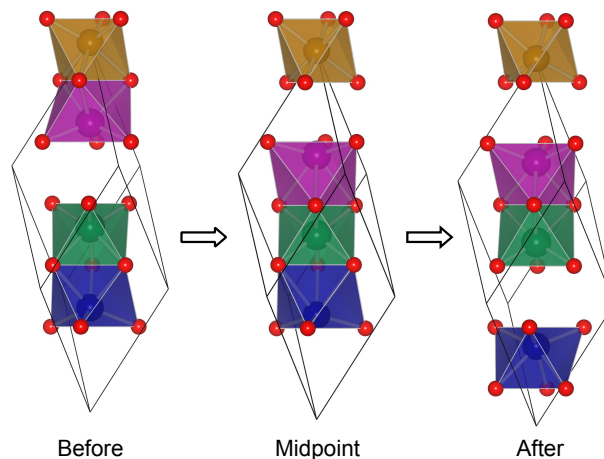


Figure 5.4: Structural evolution along the polarization reversal path of LNO-type and ordered-LNO corundum derivatives. “Before” and “After” are the initial and final structures on the reversal path with symmetry $R3c$ for the LNO-type and $R\bar{3}$ for the ordered-LNO corundum derivatives; “Midpoint” denotes the structure halfway between these and exhibits $R\bar{3}$ structural symmetry in both cases.

Fig. 5.4 is thus displaced from the origin along the line $\xi_1 = -\xi_2$. There is a spontaneous breaking of symmetry at the point where the structure departs from the $\xi_1 = \xi_2$ diagonal; at this point the system “randomly” makes a choice between two equivalent paths, marked by filled and open red symbols in Fig. 5.3.

For the ordered-LNO materials the two A cations are inequivalent, and one of them is already closer to the oxygen plane in the ground state. Let this be the one labeled by ξ_1 . Therefore, it is energetically favorable for this particular A cation to migrate first in the reversal path, which causes either the B or B' cation to be sandwiched between two A cations in the ‘Midpoint’ structure as illustrated in Fig. 5.4. The system thus deterministically follows the path indicated by the full blue line in Fig. 5.3, with the configuration always staying on one side of the $\xi_1 = \xi_2$ diagonal. If we would reverse the convention on the definition of ξ_1 and ξ_2 , the system would be described by the dashed blue path in Fig. 5.3.

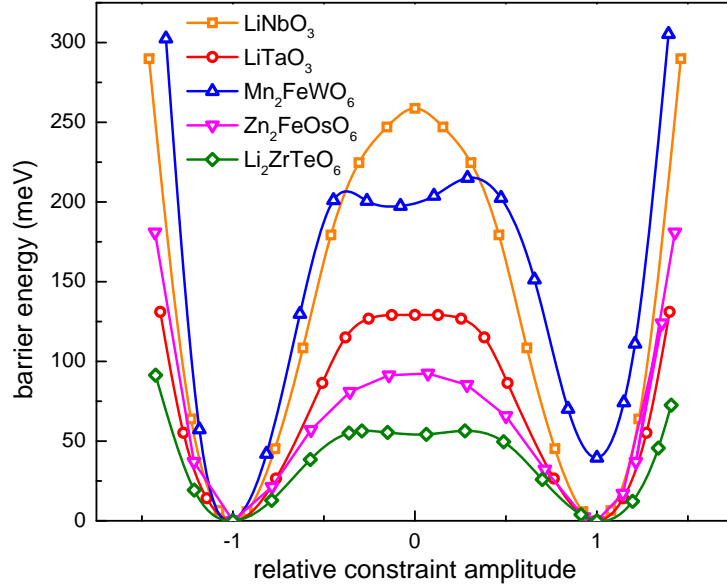


Figure 5.5: Polarization reversal energy profile for LiNbO_3 , LiTaO_3 , Mn_2FeWO_6 , $\text{Zn}_2\text{FeOsO}_6$, and $\text{Li}_2\text{ZrTeO}_6$.

5.4.3 Polarization reversal barrier

Using structural constraint methods, we compute the relaxed structures and energies for a sequence of constrained values of reaction coordinate for each material of interest. A selection of results for the energy along the path are presented in Fig. 5.5, and quantitative results for the energy barrier E_{barrier} and the spontaneous polarization P_S in the ground-state structure are reported in Table 5.8. For Mn_3WO_6 and Mn_2FeWO_6 with udu magnetic order, the FE reversal changes the magnetic state to duu , so that the energy profile is no longer symmetric and the two minima become inequivalent. For these two compounds, the value of the energy barrier in Table 5.8 is that of the highest barrier along the transformation path. Among the computed energy barriers, those for ZnSnO_3 , $\text{Li}_2\text{ZrTeO}_6$, $\text{Li}_2\text{HfTeO}_6$, Mn_2FeWO_6 , Mn_3WO_6 , and $\text{Zn}_2\text{FeOsO}_6$ are lower than or comparable to those of the established FE materials LiNbO_3 and LiTaO_3 .

The midpoint of ordered-LNO have two possible structures in which either B or B' cation is sandwiched by two A cations. Comparing energy of the two midpoint structures $\Delta E = E_B - E_{B'}$ listed in Table 5.9, it is found that the sandwiched cations

Table 5.8: Coherent polarization reversal barrier E_{barrier} (meV) per unit cell and spontaneous polarization P_S ($\mu\text{C}/\text{cm}^2$) for FE candidates.

LNO-type	E_{barrier}	P_S	Ordered-LNO	E_{barrier}	P_S
LiNbO ₃	259	82	Li ₂ ZrTeO ₆	57	33
LiTaO ₃	129	57	Li ₂ HfTeO ₆	61	32
ZnSnO ₃	241	57	Mn ₂ FeWO ₆	215	63
FeTiO ₃	763	105	<i>uud</i> Mn ₃ WO ₆	240	69
MnTiO ₃	468	94	<i>udu</i> Mn ₃ WO ₆	272	70
			Zn ₂ FeOsO ₆	92	52

are Zr for Li₂ZrTeO₆, Hf for Li₂HfTeO₆, W for Mn₂FeWO₆ and Mn₃WO₆, and Os for Zn₂FeOsO₆. The results can also be directly predicted from their ground state. For the ordered-LNO materials the two A cations are inequivalent, and one of them is already closer to the oxygen plane in the ground state,. Therefore it is energetically favorable for this particular A cation to migrate first in the reversal path, which causes either the B or B' cation to be sandwiched between two A cations in the midpoint structure. Let me denote the distance between A_1 (or A_2) cation and the oxygen plane in the ground state by ξ_{1S} (or ξ_{2S}). If $\xi_{1S} > \xi_{2S}$, the sandwiched cation is B ; otherwise it is B' . The above analysis is consistent with the calculated energy difference between the B and B' sandwiched midpoint structures, as shown in Table 5.9. In addition, it is found that the energy difference between the two distinct midpoint structures is mainly due to the difference of Madelung energies $\Delta E^M = E_B^M - E_{B'}^M$ of the two structures in a simple point-ion model, as shown in Table. 5.9.

We have analyzed the calculation results in an attempt to extract empirical rules of thumb that may help point in the direction of more new materials with low reversal barriers. Firstly, we have considered how the energy barriers are correlated with the spontaneous polarizations. In a FE material the energy E is often approximated as a double well of the form $E(P) = E_0 - \mu P^2 + \nu P^4$ with positive μ and ν . Minimizing $E(P)$ within this model gives the spontaneous polarization as $P_S^2 = \mu/2\nu$ and the energy barrier $E_{\text{barrier}} = E(0) - E(P_S) = \mu^2/4\nu$, which can also be written as $E_{\text{barrier}} = (\mu/2)P_S^2$. Thus, as long as μ can be taken as approximately constant, E_{barrier} is proportional to P_S^2 . Interestingly, it is found that the computed coherent barrier energies E_{barrier}

Table 5.9: Midpoint structures of ordered-LNO candidates and the energy differences between B and B' sandwiched midpoint structures. The distances between A_1 (or A_2) cation and the oxygen planes in the ground state are characterized by ξ_{1S} (or ξ_{2S}). The energy difference between the B and B' sandwiched midpoint structures is ΔE . The Madelung energy difference between the B and B' sandwiched midpoint structures is ΔE^M .

Ordered-LNO	B	B'	Sandwiched	ξ_{1S} (Å)	ξ_{2S} (Å)	ΔE^M (meV)	ΔE (meV)
$\text{Li}_2\text{ZrTeO}_6$	Zr	Te	Zr	0.607	0.559	-186	-48
$\text{Li}_2\text{HfTeO}_6$	Hf	Te	Hf	0.582	0.550	-94	-29
Mn_2FeWO_6	Fe	W	W	0.623	0.707	2085	225
$uud \text{ Mn}_3\text{WO}_6$	Mn	W	W	0.635	0.799	1666	266
$udu \text{ Mn}_3\text{WO}_6$	Mn	W	W	0.642	0.790	1499	290
$\text{Zn}_2\text{FeOsO}_6$	Fe	Os	Os	0.565	0.574	382	102

roughly follow this trend with $\mu/2 = 0.057 \text{ meVcm}^4/\mu\text{C}^2$ as shown in Fig. 5.6. Therefore, the results suggest that FE corundum derivatives are more likely to be discovered in materials having a relatively low spontaneous polarization.

Furthermore, we have investigated the correlation between the spontaneous polarizations and the geometric properties of the crystals. Our results suggest that for each FE candidate, the polarization P along the reversal path is almost linearly related to the reaction coordinate ξ . Expecting $P(\xi)$ to be an odd function, we add a small cubic part and fit it as $P(\xi) = m\xi + n\xi^3$. The parameters m and n are different in each material, and they are determined by several factors that are not included in the reaction coordinate ξ , such as displacements of the B cations and valence states of the A cations. Despite these differences between materials, it is found that the spontaneous polarizations P_S of corundum derivatives are correlated with the reaction coordinate $\xi_S = \xi_{1S} + \xi_{2S}$ in the spontaneously polarized ground state, as shown in Fig. 5.7. This time a roughly linear fit clearly does not work. Again we try fitting $P_S(\xi_S)$ to an odd third-order polynomial, and find that $P_S = m\xi_S + n\xi_S^3$ gives a reasonable fit with $m = 13.3 \times 10^8 \mu\text{C}/\text{cm}^3$ and $n = 19.0 \times 10^{24} \mu\text{C}/\text{cm}^5$ as shown in the figure. As the distance between A cations and oxygen planes can be experimentally determined, this empirical rule can provide a rough estimation of the spontaneous polarization.

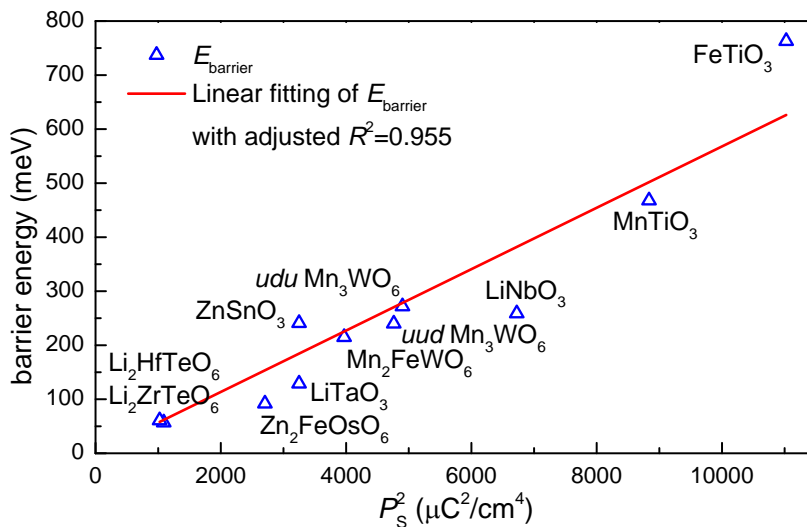


Figure 5.6: Empirical proportionality between the coherent FE energy barrier and P_S^2 . The red curve is the fitting polynomial $E_{\text{barrier}} = (\mu/2)P_S^2$, with $\mu/2 = 0.057 \text{ meVcm}^4/\mu\text{C}^2$.

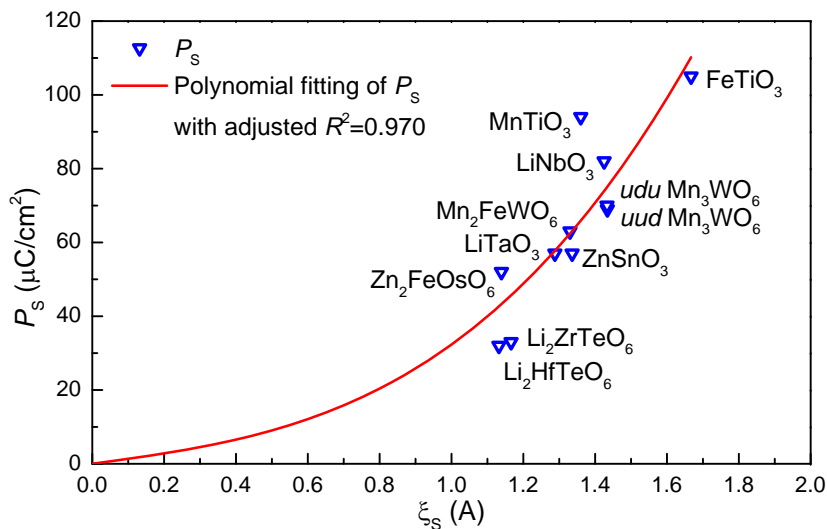


Figure 5.7: Empirical correlation between the spontaneous polarization and the reaction coordinate ξ in the ground state. The red curve is the fitting polynomial $P_S = m\xi_S + n\xi_S^3$ with $m = 13.3 \times 10^8 \mu\text{C}/\text{cm}^3$ and $n = 19.0 \times 10^{24} \mu\text{C}/\text{cm}^5$.

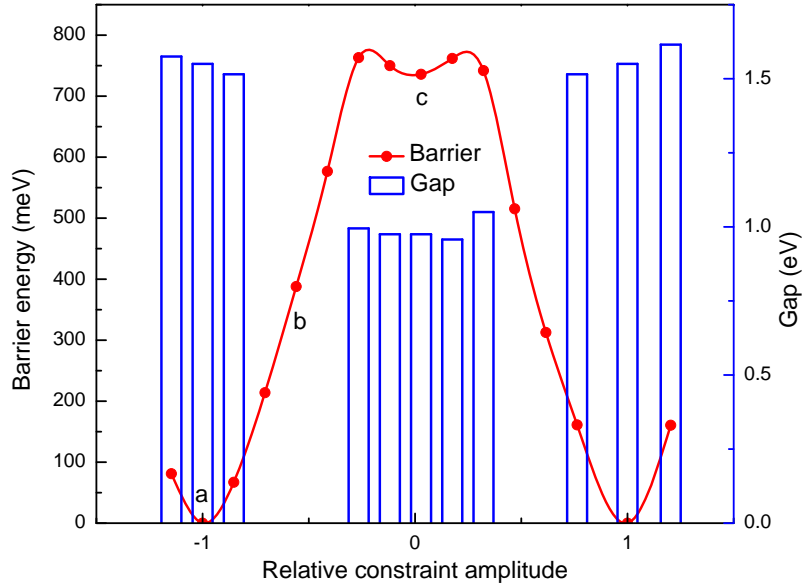


Figure 5.8: Energy profile and bandgap at the polarization reversal path of FeTiO_3 . The band gap is 1.56 eV and 0.98 eV at points a and c, but FeTiO_3 is conducting at point b.

5.4.4 Insulating vs conducting

FeTiO_3 and Mn_2FeWO_6 do not stay insulating along the coherent reversal path. The energy profile and bandgap of FeTiO_3 along the path is shown in Fig. 5.8 as an illustration. FeTiO_3 has a finite gap at points a and c, but becomes conducting at point b. In order to understand the orbital character around the Fermi energy, the projected density of states (PDOS) of points a, b, and c are shown in Fig 5.9(a-c), respectively.

A detailed analysis of the occupied d orbitals along the path reveals the reason for this metal-insulator transition. In the local octahedral environment of the ground state, the d orbitals are split into triply degenerated t_{2g} and doubly degenerated e_g orbitals. Under the threefold rotational symmetry, the t_{2g} orbitals are further split into a_{1g} and doubly degenerate e'_g irreps. The a_{1g} state has orbital character d_{z^2} with charge lobes directed along the rhombohedral axis, and since these lie closer to the neighboring cations, the energy of the a_{1g} state is lowered. Therefore, the ground-state arrangement of d orbitals in order of increasing energy is a_{1g} followed by e'_g and then e_g . In FeTiO_3 and Mn_2FeWO_6 , Fe is in the 2+ valence state and has a d^6 configuration. In the ground

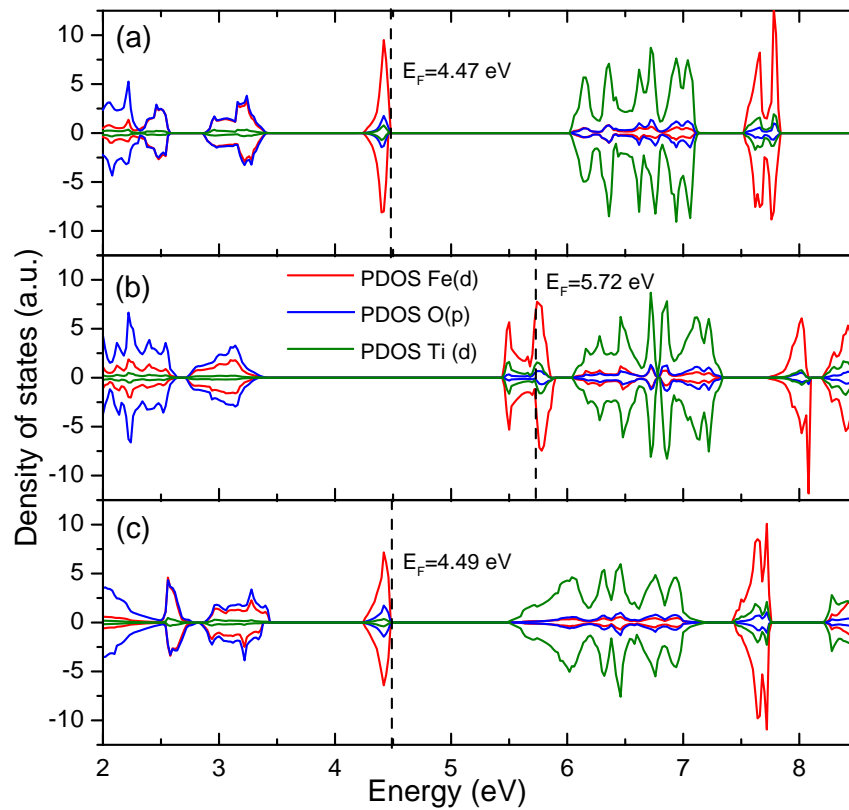


Figure 5.9: PDOS of FeTiO_3 at point (a), (b), and (c) along the coherent reversal path. Position of Fermi energy are indicated by dashed black lines. The density of states from two spin channels are represented by the positive branch and negative branch of density of states, respectively. The unit a.u. means arbitrary unit.

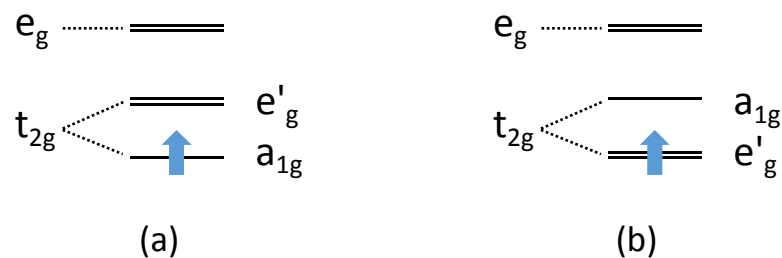


Figure 5.10: Sketch of energy levels of d orbital in the (a) insulating case and (b) the conducting case.

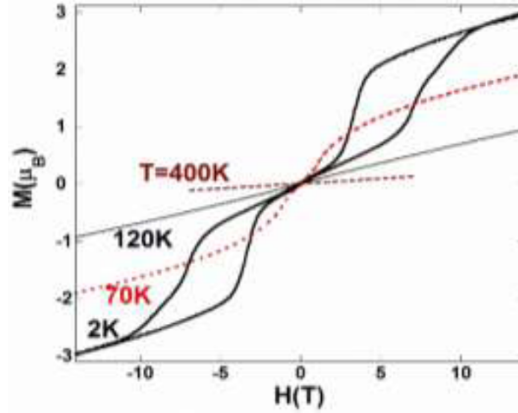


Figure 5.11: **M-H** relation (between -14 and 14 T) of Mn_2FeWO_6 at 2, 70, 120, and 400 K, taken from Ref. [44].

state, five electrons fully occupy one spin channel and the remaining one occupies the a_{1g} orbital in the minority spin channel, as shown by the PDOS in Fig. 5.9(a) and the energy level sketch in Fig. 5.10(a). However, during the polarization reversal process, the Fe^{2+} ion temporarily moves away from its neighboring cations, and as a result, the a_{1g} orbital is no longer energetically favored. Instead, the minority electron occupies the doubly degenerate e'_g orbitals, leading to a metallic state, as shown in Fig. 5.9(b) and Fig. 5.10(b). Since a metallic state along the polarization reversal path could short out the applied bias, it may be that the switching of polarization is not possible in such cases. Therefore, we propose that d^3 , d^5 , and d^8 orbital configurations should be much more likely to avoid this conducting problem, and are therefore more suitable targets in the search for ferroelectrically switchable magnetic corundum derivatives.

5.4.5 More complicated magnetic structures

In previous sections, only magnetic orderings that preserve the periodicity of the rhombohedral unit cell were considered, since our major focus is on the polarization reversal mechanism. Under such an assumption, the ground state magnetic order of Mn_2FeWO_6 is FiM udu at $T = 0$ K with a net magnetization of $\sim 4 \mu_B$. However, according to the experimental **M-H** relation [44] shown in Fig. 5.11, the magnetic structure at 2 K does not have a net magnetization at zero field, but exhibits an AFM double-hysteresis loop.

Table 5.10: Magnetic energies for AFM doubled-cell magnetic structures. ΔE_1 is for energies evaluated at the unrelaxed experimental structure, while ΔE_2 applies to energies calculated after relaxation of the internal coordinates. The energy is given with respect to the *udu* magnetic order in the experimental cell with unit meV/f.u. .

Magnetic order	<i>udu</i>	<i>uuu-ddd</i>	<i>uud-ddu</i>	<i>udu-dud</i>	<i>udu-udd</i>	<i>duu-udd</i>
ΔE_1	0	22	8	14	11	23
ΔE_2	-202	-197	-208	-204	-210	-192

In order to explain the observed low-temperature magnetic behavior, we consider AFM doubled-cell magnetic structures containing two formula units (f.u.). In the doubled-cell magnetic structure, one cell has a positive magnetization with a magnetic order *uuu*, *uud*, *udu* or *duu*, and the other cell has the opposite magnetization. Therefore, only five possible doubled-cell magnetic orders do not exhibit net magnetization, and they are *uuu-ddd*, *uud-ddu*, *udu-dud*, *udu-udd*, and *duu-udd*. In these notations, the letters before or after “-” are the magnetic orders in the first or second cell. Among these magnetic orders, four of them are composed by two subcells with magnetic orders that are related by time-reversal symmetry, and the only exception is the magnetic order *udu-udd*.

The energy of the five doubled-cell magnetic structures are shown in Table 5.10. With the unrelaxed experimental structure [44], the lowest-energy magnetic ordering among the doubled-cell configurations is *uud-ddu*, i.e., the one obtained by a combination of *uud* and *ddu* primitive cells. After relaxation of the internal coordinates, however, the *udu-udd* magnetic structure becomes the most stable. The energy reduction from lattice relaxation is largest for the *udu-udd* composite cell because the magnetic order of the two subcells is not related by time-reversal symmetry, so that additional zone-boundary phonon modes can relax and contribute to lowering the energy. The *udu-udd* double cell is even lower in energy than the *udu* single-formula-unit structure, by 8 meV/f.u. Therefore, the results suggest that the magnetic double-hysteresis loop visible at low temperature in Fig. 5.11 might be understood as a series of transitions from a *dud* FiM order at negative field to a *udu-udd* (or *dud-duu*) configuration at zero field, then back to a *udu* FiM configuration at positive field.

Table 5.11:

	$R\bar{3}c$		$R\bar{3}$	
	TO	LO	TO	LO
LiNbO ₃	216 <i>i</i>	109 <i>i</i>	158 <i>i</i>	150
LiTaO ₃	178 <i>i</i>	74 <i>i</i>	24	143

We have only considered collinear magnetic structures here. However, our study of the doubled-cell structures strongly suggests that there is a magnetic phase transition at finite magnetic field, below which the magnetic order is AFM, in a magnetic unit cell including at least two formula units, possibly with a more complex non-collinear magnetic structure that has not been considered here. Above the critical magnetic field, we expect the system to adopt the collinear *udu* FiM structure, with a single-formula-unit magnetic cell.

5.4.6 Hyperferroelectric?

Hyperferroelectrics are a class of proper FEs that polarize even at $\mathbf{D} = 0$ (vanishing electric displacement field) boundary conditions when the depolarization field is unscreened [11]. This condition is equivalent to the instability of a longitudinal optic (LO) mode, in addition to that of a transverse optic (TO) mode which is the characteristic of proper FEs. In a previous study [131], it was theoretically proposed that LiNbO₃ and LiTaO₃ are hyperferroelectric, because there is an unstable LO mode at the paraelectric $R\bar{3}c$ structure. However, our study of the polarization reversal path suggests that the FE polarization reversal does not pass through the structure with $R\bar{3}c$ symmetry, and instead the high-symmetry midpoint structure has the symmetry $R\bar{3}$. Therefore, it would be more relevant to study the LO mode instability at the $R\bar{3}$ midpoint structure.

Here we use Eq. 1.3 introduced in Chapter 1 and frequencies of the TO modes shown in Table 5.7 to calculate the frequencies of the LO modes, and the results for the unstable polar modes are summarized in Table 5.11. In the $R\bar{3}c$ structure, both the TO modes and the LO modes are unstable, consistent with previously reported

frequencies [125, 131]. As a result, in the $P_{R\bar{3}c}$ structure with $\mathbf{D} = 0$ condition, the LO mode displacement can lower the energy, and bring the structure to a stable state at $R\bar{3}c$ symmetry with a finite polarization. Here we use the notation $P_{R\bar{3}c}$ to denote the polar state. However, in the $R\bar{3}$ structure, the TO modes get less unstable and the LO modes are stabilized. Therefore at $\mathbf{D} = 0$ boundary condition, the non-polar $R\bar{3}$ structure is also a stable state and we call it $NP_{R\bar{3}}$.

Although we have shown that there is no unstable LO mode in the $R\bar{3}$ structure in LiNbO_3 and LiTaO_3 , we cannot conclude that they are not hyperferroelectric yet. After all, if the $NP_{R\bar{3}}$ state is only a metastable state, and the energy of the $P_{R\bar{3}c}$ state is lower than that of $NP_{R\bar{3}}$, a finite polarization can still exist at $\mathbf{D} = 0$. To answer this question, calculation in the $\mathbf{D} = 0$ boundary condition is required to explore the $P_{R\bar{3}c}$ state, which is not the calculation we have done at $\boldsymbol{\mathcal{E}} = 0$. Therefore, this question is left for future investigations.

5.5 Summary and outlook

In this chapter, we have proposed a method to study the coherent FE reversal path of the corundum derivative family. By analyzing the structures, it is shown that only the LNO-type and the ordered-LNO corundum derivatives can be FE in the usual sense. We have calculated the energy profiles of the reversal paths using first-principles density-functional methods. Our calculations reveal that the symmetry of the FE barrier structure is lower than that of the paraelectric phase. According to the calculated energy barrier, ZnSnO_3 , $\text{Li}_2\text{ZrTeO}_6$, $\text{Li}_2\text{HfTeO}_6$, Mn_3WO_6 , and $\text{Zn}_2\text{FeOsO}_6$ are predicted to be possible new FEs. In addition, we have found empirically that the energy barrier is roughly proportional to the square of the spontaneous polarization, and that the spontaneous polarization is strongly correlated with the reaction coordinate ξ in the ground state. Furthermore, we have also argued that magnetic corundum derivatives are unlikely to be suitable for FE switching unless the magnetic ion is d^3 , d^5 or d^8 , since metallic configurations otherwise tend to appear along the FE reversal path. At last, by considering the possible doubled-cell AFM magnetic structures in Mn_2FeWO_6 , we have proposed a possible explanation for the observed double-hysteresis loop in experiments.

Meanwhile, there are still many open questions that remain to be answered. Firstly, the polarization reversal path is only studied for the coherent reversal, which is not the actual physical process observed in experiments. The polarization reversal occurs through the motion of FE domain walls, which only have the thickness of a few unit cells for many FEs. Therefore, the reversal energy barrier and electronic structure at the domain walls might be very different from the bulk and the coherent reversal, and this is the subject of the next chapter. Secondly, we have only briefly discussed the hyperferroelectricity in LiNbO_3 and LiTaO_3 , and more investigations in the $\mathbf{D} = 0$ boundary conditions are needed to answer this question. Lastly, the predictions of magnetic orders are tricky if the magnetic symmetry is unknown. In the study of the coherent polarization reversal, we have only considered the simplest possible magnetic orderings which are consistent with the rhombohedral unit cell. However, it is found that in Mn_2FeWO_6 , a double-cell magnetic order is more stable, and we would not be surprised if the actual magnetic structure is even more complicated with non-collinear spins in a much larger magnetic cell.

Chapter 6

Ferroelectric and magnetoelectric domain walls in corundum derivatives

6.1 Introduction

In Chapter 5, we discussed the coherent ferroelectric (FE) reversal process in corundum derivatives. However, the hysteresis behavior of FE reversal is caused by the nucleation, expansion or shrinkage of domains through the motion of domain walls in an applied electric field. FE domains are regions of different polarization orientations that may coexist in a FE crystal. The interface between two domains are referred to as a domain wall (DW). The experimental images of FE domains and DWs of LiNbO_3 [132] and YMnO_3 [133] are shown in Fig. 6.1 as an illustration. An applied electric field would favor the domains with polarization paralleled to the field, so these domains would expand to gain electric energy while the opposite domains would shrink, which is achieved through the motion of domain walls. Meanwhile, defects can be attracted to the DW and can pin the DW motion [134].

DWs can be seen as topological defects which have different geometric and electronic structures compared to the bulk, so DWs may exhibit rich physics that is not present in the bulk. For instance, in the FE-antiferromagnetic insulating BiFeO_3 , experiments have shown that the DWs behave as conductive channels in the otherwise insulating background [135]. Meanwhile, the same DWs are suggested to exhibit photovoltaic properties as well [136]. Furthermore, it is recently observed that charged FE DWs, which are energetically unfavorable in general, are abundant in hybrid improper FEs $(\text{Ca, Sr})_3\text{Ti}_2\text{O}_7$ [137]. Moreover, in hexagonal manganite $R\text{MnO}_3$ ($R = \text{Sc, Y, In, and Ho-Lu}$), the FE DWs form topologically protected vortices [133], and alternating magnetic moments are found at the FE DW around the vortex core [138]. In addition,

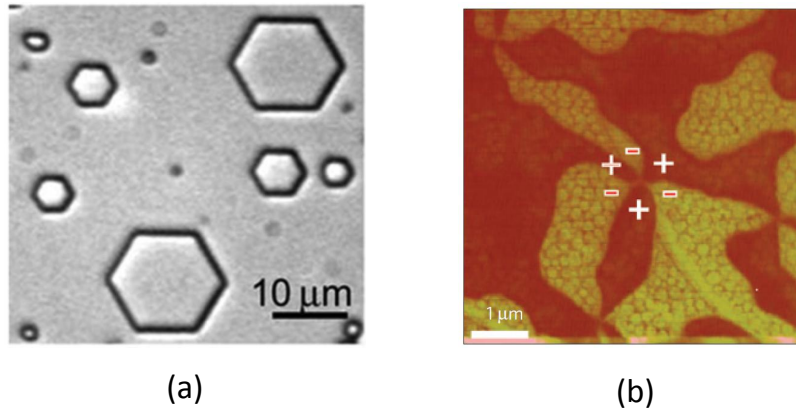


Figure 6.1: FE domains and domain walls observed in (a) LiNbO_3 , taken from Ref. [132] and (b) YMnO_3 , taken from Ref. [133]

the FE DWs are also observed interlocking with chiral DWs in Ni_3TeO_6 [139].

In the newly proposed FE corundum derivatives, the properties of FE DWs and the role of DWs in polarization reversal are not clear. Firstly, many corundum derivatives are in the form of powder samples because of the high-pressure syntheses, so that the growth of single crystals and the observations of domains and DWs are an ongoing problem. Secondly, corundum derivatives may exhibit magnetic orders in the ground state, making them multiferroics. Even if the origin of the polarization and magnetization are different in the bulk, the distinct structure at the domain wall may enhance the coupling between the polarization and magnetization. Thirdly, the ordered-LNO exhibits a chiral structure, so there might be an interplay between chiral domains and FE domains. Finally, as the DW structure is very different from the bulk, it would be interesting to investigate how the DW structure would influence the reversal barrier.

In this chapter, we use first-principles methods to study the formation and motion of FE DWs at the atomic scale in order to characterize the properties of DWs and their role in the FE reversal process. The FE candidates that we consider are LiNbO_3 (LNO), LiTaO_3 , ZnSnO_3 , FeTiO_3 , MnTiO_3 , $\text{Li}_2\text{ZrTeO}_6$, $\text{Li}_2\text{HfTeO}_6$, and Mn_3WO_6 . Our study of the 180° charge-neutral DWs predicts the orientation and shape of DWs in corundum derivatives. Moreover, the DW formation energy also suggests that in ferrimagnetic Mn_3WO_6 , the FE DWs are simultaneously magnetic DWs, and when the polarization

at the DW is reversed by an electric field, so is the magnetization. Therefore, this study demonstrates a strong magnetoelectric coupling at the DW of corundum derivatives. Finally, we point out that the DW-mediated reversal barrier is strongly correlated with the local bonding environment of A cations.

6.2 First-principles methodology

The calculations are performed with plane-wave density functional theory (DFT) implemented in VASP [56] with PBEsol [51] as the exchange-correlation functional. The ionic core environment is simulated by projector augmented-wave (PAW) pseudopotentials [61]. We use a Hubbard $U = 4.2$ eV on the $3d$ orbitals of Mn and Fe [53]. The magnetic moments are collinear and spin-orbit coupling is neglected. The cutoff energy for all calculations is 550 eV. The energy error threshold varies slightly in different calculations, but an accuracy between 1.0×10^{-5} and 1.0×10^{-7} eV is achieved. The forces are reduced below 0.01 eV/Angstrom in the DW structural relaxations. A $2 \times 6 \times 2$ Monkhorst-Pack k -mesh is used in X-wall calculations, and a $6 \times 6 \times 1$ k -mesh is used in the Y-wall calculations.

6.3 Results and discussion

6.3.1 Construction of domain walls

The general structure of corundum derivatives ABO_3 and $A_2BB'O_6$ were introduced in Chapter 5, and here we only focus on the LNO-type and ordered-LNO structure which are compatible with ferroelectricity at the rhombohedral [111] direction. In Fig. 6.2, both the rhombohedral unit cell and views from different hexagonal directions are illustrated. Each cation is in a distorted oxygen octahedron and one third of the oxygen octahedra are cation-vacant, which is denoted by “-” as defined in Chapter 5. The FE reversal is driven by migration of A cations from their own oxygen octahedron to the cation-vacant octahedron above or beneath them [124, 125] and the reversal path can be qualitatively described by two variables ξ_1 and ξ_2 defined as the vertical distances between each A cation and the oxygen plane that it penetrates during the

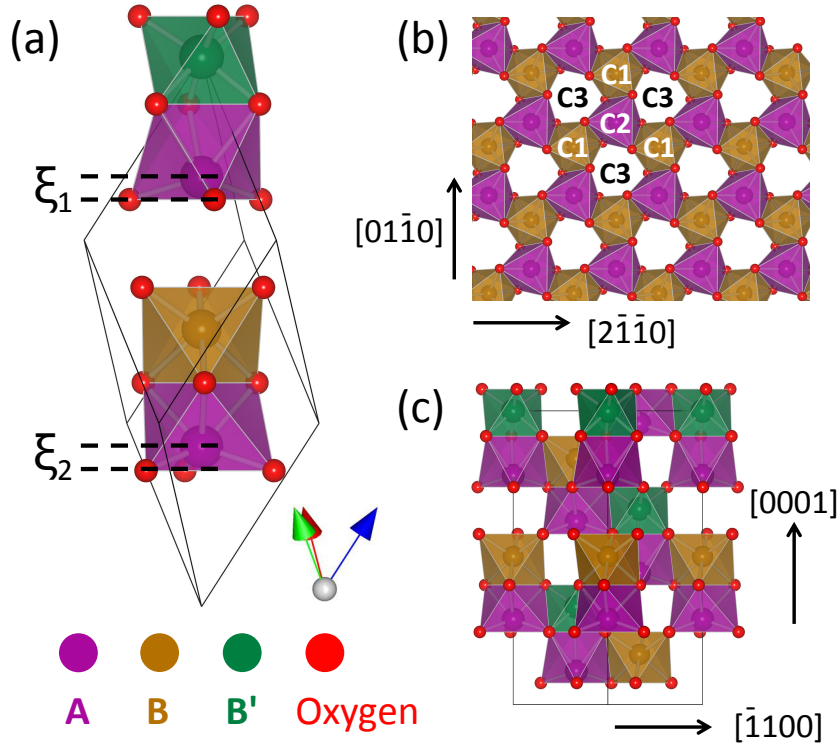


Figure 6.2: Structure of LNO-type corundum derivative ABO_3 when $B' = B$, and ordered-LNO corundum derivative $A_2BB'O_6$. (a) Side view of the rhombohedral unit cell. ξ_1 (or ξ_2) is the vertical distance between an A cation and the oxygen plane that it penetrates during the polarization reversal. (b) Top view of the AB layer and (c) side view in the enlarged hexagonal-setting cell. The enlarged hexagonal cell consists of three columns of octahedra C1, C2, and C3.

polarization reversal. The definitions of ξ_1 and ξ_2 are also shown in Fig. 6.2(a).

In order to study the properties of DWs, we construct a supercell with a polarization-up domain and a polarization-down domain that are related by the inversion symmetry, and the boundary between them is a FE DW [140]. Because of periodic boundary conditions, there are always two DWs in the supercell, a left-up-right-down $DW_{\uparrow\downarrow}$ and a left-down-right-up $DW_{\downarrow\uparrow}$, where \uparrow and \downarrow represent up and down polarization directions. In corundum derivatives, the $R3c$ symmetry of the LNO-type structure ensures that the $DW_{\uparrow\downarrow}$ and $DW_{\downarrow\uparrow}$ are equivalent, but in the ordered-LNO structure with $R3$ symmetry, the two DWs are inequivalent. However, as $DW_{\uparrow\downarrow}$ and $DW_{\downarrow\uparrow}$ coexist in calculations with periodic boundary conditions, we report the averaged DW

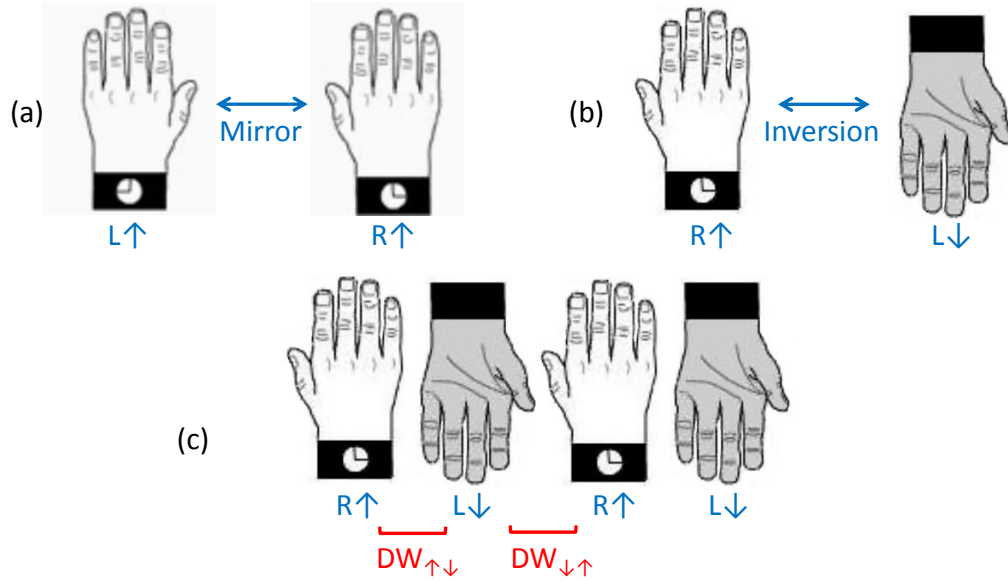


Figure 6.3: Illustration of domains and DWs in chiral polar object. Left and right hands represent left (L) and right (R) chirality, and the direction in which the fingers point (\uparrow or \downarrow) represents the polarization direction. (a) Left and right chirality are related by a mirror symmetry. (b) Upward right hand ($R\uparrow$) and downward left hand ($L\downarrow$) are related by the inversion symmetry. (c) FE domains and DWs formed by ($R\uparrow$) domains and ($L\downarrow$) domains. The DW between adjacent thumbs represents $DW_{\uparrow\downarrow}$ and the DW between adjacent little fingers represents $DW_{\downarrow\uparrow}$.

formation energy between $DW_{\uparrow\downarrow}$ and $DW_{\downarrow\uparrow}$ for ordered-LNO materials.

The intrinsic difference between $DW_{\uparrow\downarrow}$ and $DW_{\downarrow\uparrow}$ in ordered-LNO are attributed to the chiral nature of the structure. A structure is chiral if it is distinguishable from its mirror image. The symmetry of ordered-LNO is $R3$ which does not contain any mirror symmetry, so it has a chiral structure. In contrast, the LNO-type structure is not chiral because its symmetry is $R3c$. The term *chirality* is derived from the Greek word for hand; left hand has left chirality (L) while right hand has right chirality (R). In Fig. 6.3, hands are used as an illustration of FE domains to explain why $DW_{\uparrow\downarrow}$ and $DW_{\downarrow\uparrow}$ are inequivalent. The direction that the fingers are pointing towards represents the polarization direction, and the left or right hand represents the chirality L or R. The spatial inversion operation changes (x, y, z) to $(-x, -y, -z)$, so the upward right hand ($R\uparrow$) becomes the downward left hand ($L\downarrow$) under inversion, through which both

polarization and chirality are flipped, as shown in Fig. 6.3(b). The domains and DWs formed by upward right hands and downward left hands are shown in Fig. 6.3(c). It is apparent that the FE DW is also a chiral DW in chiral polar materials, and this interlocking effect between polarization and chirality at the DW is observed in chiral pyroelectric Ni_3TeO_6 [139]. It is also clear that there are two kinds of interfaces between hands, one between thumbs and the other one between little fingers, and these correspond to the $\text{DW}_{\uparrow\downarrow}$ and $\text{DW}_{\downarrow\uparrow}$.

Chirality can qualitatively explain or predict the shape of domains in corundum derivatives. In LiNbO_3 and other LNO-type materials with symmetry R3c, because $\text{DW}_{\uparrow\downarrow}$ and $\text{DW}_{\downarrow\uparrow}$ are identical, according to the Wulff construction [141], domains of LNO-type should form regular hexagons. In contrast, in order-LNO, domains should form equiangular but not equilateral hexagons, or even triangles. In fact, the regular-hexagon-shape domains are observed in LiNbO_3 [132] as shown in Fig. 6(a), while triangle shape domains are found in Ni_3TeO_6 with ordered-LNO structure [139].

To arrive at our domain wall configurations, we assume that the B/B' and O sublattices are preserved throughout the supercell, so that the DW only results from the interchange of A and “ $-$ ” sublattices (that is, migration of A cations into vacancies) on one side of the DW. This is motivated by the greater mobility of the A cation species. In addition, only the 180° charge-neutral DW is considered, in which the polarization direction is parallel to the DW plane but antiparallel between domains.

6.3.2 Orientation of domain walls

Since corundum derivatives have three-fold symmetry, there are two types of 180° DWs depending on the orientation of the DW plane. The DW in the x - z plane is called the X-wall and the one in the y - z plane is called the Y-wall. The top view and the side view of the X-wall and Y-wall are shown in Fig. 6.4 in comparison with the bulk structure in Fig. 6.2(b-c). In the layer shown in Fig. 6.4(a), octahedra containing A cations are densely packed at the X-wall. However, there are also layers where the octahedra at the X-wall are all cation-vacant. In short, the X-wall consists of alternating dense and sparse octahedra layers. In comparison, the A and $-$ sublattices are more evenly

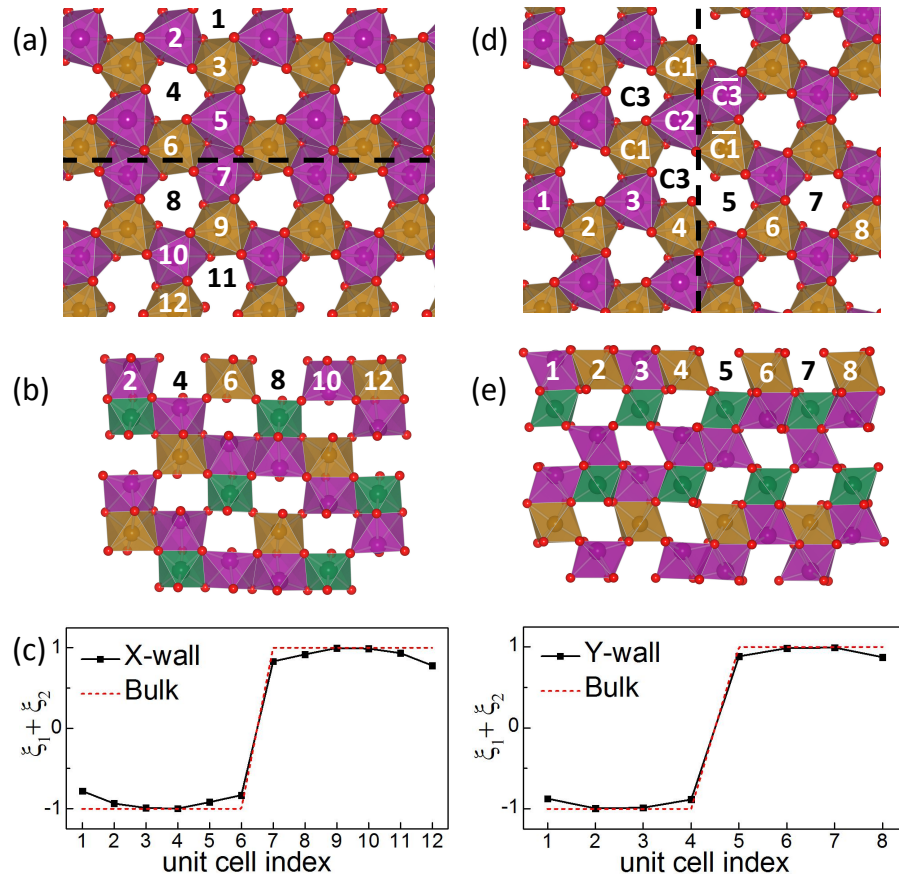


Figure 6.4: Structures of X-wall in the 6+6 supercell and Y-wall in the 4+4 supercell. (a)(d) Top views of the X-wall and Y-wall. The number in each octahedron is the unit cell label. The X-wall is in the x - z or $(01\bar{1}0)$ plane and is located between the 6th and the 7th unit cell, shown by the dashed line. The Y-wall is in the y - z or $(2\bar{1}\bar{1}0)$ plane and is located between the 4th and the 5th unit cell. (b)(e) Side views of the X-wall and Y-wall. Odd-number cells are behind even-number cells in the X-wall. (c)(f) The $\xi_1 + \xi_2$ displacement profile of X-wall and Y-wall. (d) C1, C2, and C3 are three different columns of octahedra in the left-side domain. $\bar{C}1$ and $\bar{C}3$ are columns of octahedra in the right-side domain. The column C1 becomes $\bar{C}1$ after the polarization reversal.

Table 6.1: Formation energy of X-wall and Y-wall. For the ordered-LNO structure, the formation energy is averaged between the $DW_{\uparrow\downarrow}$ and $DW_{\downarrow\uparrow}$. The unit is mJ/m^2 .

LNO-type	Magnetic order	X	Y	Ordered-LNO	Magnetic order	X	Y
LiTaO ₃		71	63	Li ₂ ZrTeO ₆		29	20
LiNbO ₃		160	138	Li ₂ HfTeO ₆		30	21
ZnSnO ₃		106	81	Mn ₃ WO ₆	<i>uud-uud</i>	68	42
MnTiO ₃	<i>ud-ud</i>	171	153	Mn ₃ WO ₆	<i>udu-dud</i>	67	41
FeTiO ₃	<i>ud-ud</i>	183	108	Mn ₃ WO ₆	<i>udu-udu</i>	75	45

spaced.

To calculate the formation energy of the X-wall and the Y-wall, we construct 6+6, 6+7 supercells for the X-wall, and 3+4, 4+4, and 4+5 supercells for the Y-wall. Here the supercell notation $m + n$ means that m unit cells are of polarization down and n unit cells are of polarization up. The $m + m$ supercell preserves some symmetry, while the $m + (m + 1)$ supercell has none because of the asymmetry of the size of up and down domains. In the $m + m$ supercells, the up and down domains are related by inversion symmetry through a center lying in the DW. Furthermore, for the LNO-type structure, the identical $DW_{\uparrow\downarrow}$ and $DW_{\downarrow\uparrow}$ are also related by two-fold rotation. The displacements $\xi_1 + \xi_2$ in each cell of the 6+6 X-wall and the 4+4 Y-wall of Li₂ZrTeO₆ are shown in Fig. 6.4(c) and Fig. 6.4(f). The displacement profiles suggest that the DWs in corundum derivatives are atomically sharp, which are similar to the DWs of perovskites [140, 142]. Meanwhile, our calculations also predict that the Y-wall is energetically favored in all the cases that we have studied, and the converged DW formation energies are shown in Table 6.1. Our results of LiNbO₃ and LiTaO₃ are consistent with the earlier DW simulations [143]. Experimental observations on the domains of LiNbO₃ also confirm that the Y-wall is more favorable [132].

6.3.3 Magnetic and magnetoelectric domain walls

Some corundum derivatives are magnetic compounds and exhibit magnetic orders. Here we use notations “*u*” and “*d*” to represent spin-up and spin-down states on magnetic cations A_1 , A_2 and B in that order, where A_1 and A_2 are face-sharing with B' and B

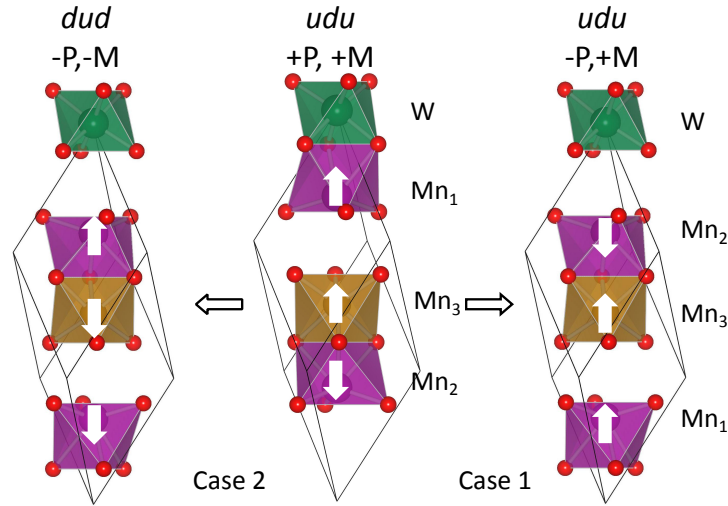


Figure 6.5: Two possible magnetic orders at FE DWs in Mn_3WO_6 . The structure in the center has polarization and magnetization (+P,+M) with the magnetic order udu . The structures on the left and right both have polarization $-P$ but the left one has the magnetic order dud while the right one is udu . In case 1, the FE DW is formed between structures in the center and on the right. In case 2, the FE DW is formed by the central and leftward structures.

cations, respectively. Since spin-orbit coupling is neglected in our calculations, “up” and “down” are not necessarily $\pm\hat{z}$. In Chapter 5, it was shown that for magnetic orders that preserve the rhombohedral unit cell, the ground state magnetic order is antiferromagnetic (or ud) for MnTiO_3 and FeTiO_3 , and ferrimagnetic udu for Mn_3WO_6 , while the magnetic order uud is close in energy in Mn_3WO_6 . Because of the time-reversal symmetry, a global reversal of all the spins would not affect the total energy, e.g., udu and dud magnetic order have exactly the same energy in the bulk Mn_3WO_6 .

The magnetic order is in the ground state in each FE domain, but time-reversal symmetry still allows a global spin reversal between domains leading to two different magnetic orders across FE DWs. For instance, in udu Mn_3WO_6 , if the magnetic orders are the same on both side of the DW, it is described by case 1 in Fig. 6.5 and the DW is denoted by $udu-udu$. Here the letters before and after “-” represent magnetic orders in two neighbouring domains. If the magnetic order is reversed on one side of the DW, as shown in case 2 of Fig. 6.5, the DW is denoted by $udu-dud$. In case 1, the net

magnetization stays unchanged across the DW, while in case 2 the net magnetization reverses direction on one side of the DW. Therefore, the *udu-dud* FE DW is also a magnetic DW. Similarly, there are also *ud-ud* DW and *ud-du* DW for MnTiO₃ and FeTiO₃, but neither of them have net magnetization.

In our calculations, we consider both the *udu-udu* DW and *udu-dud* DW, and their DW formation energies are summarized in Table. 6.1. Interestingly, the results suggest that the *udu-dud* is more energetically favorable than the *udu-udu*, which means that the FE, magnetic and chiral domains are interlocked. When the polarization is reversed at the domain wall in an electric field, so is the magnetization and chirality.

As the spin-orbit coupling is not even included in our calculations, the origin of the coupling between magnetization and polarization at the DW should be categorized as an exchange-striction effect. In the remainder of this subsection, we use a simple spin model to qualitatively explain the origin of the coupling. In the bulk Mn₃WO₆, *A*₁, *A*₂, and *B* cations are all Mn²⁺, and their spins are interacted through oxygen octahedra. In a very rough approximation, we assume that there are only three independent coupling constants *J*_f, *J*_e and *J*_c, describing the exchange interaction between face-sharing, edge-sharing and corner-sharing magnetic neighbors.

In the bulk structure with cation ordering *B'A₁-BA₂-*, the exchange-interaction map of magnetic cations in three neighboring columns of octahedra C1, C2, and C3 is shown in Fig. 6.6(a). The three columns C1, C2, and C3 are also highlighted in Fig. 6.2(b). Because of the three-fold symmetry, the column C2 is surrounded by a total of six columns of octahedra that consist of alternating C1 and C3 columns. Therefore, the edge-sharing and corner-sharing pairs shown in Fig. 6.6(a) only account for one third of the total number of pairs. For example, according to Fig. 6.6(a), the *A*₂ cation in the C2 column is face sharing (blue line) with the *B* cation in the same column as well as corner sharing (green line) with three *B* cations in the C1 columns and three *B* cations in the C3 columns. Therefore, the magnetic energy per unit cell can be approximated as

$$E_{\text{bulk}} = J_f S_{A_2} \cdot S_B + 3J_c S_{A_2} \cdot S_B + 6J_c S_{A_1} \cdot S_{A_2} + 3J_e S_{A_1} \cdot S_B. \quad (6.1)$$

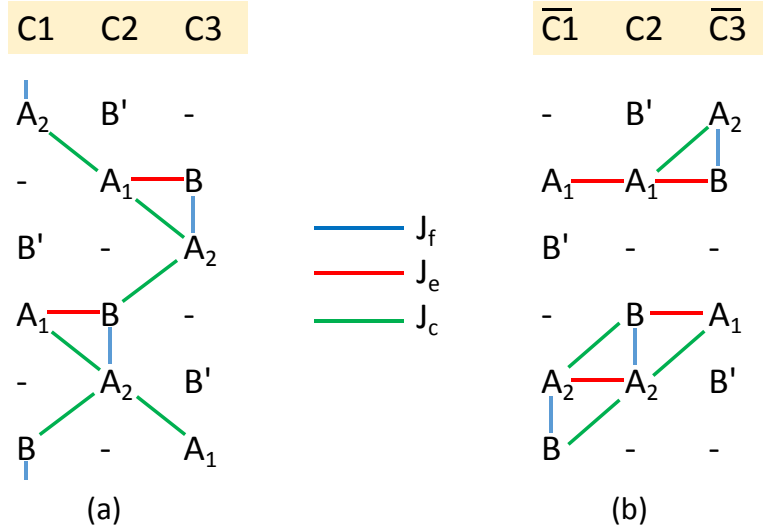


Figure 6.6: Exchange-interaction map of magnetic cations in Mn_3WO_6 (a) between C1, C2, and C3 columns of octahedra in the bulk structure, and (b) between $\bar{C}1$, C2, and $\bar{C}3$ columns of octahedra at the DW structure. The blue, red, and green lines represent the face-sharing, edge-sharing, and corner-sharing magnetic neighbors.

Inserting the energy of different magnetic orders in Table 5.5, we get $J_f = 19.4 \text{ meV}$, $J_e = 6.8 \text{ meV}$, and $J_c = 3.5 \text{ meV}$.

With the above parameters, we first estimate the energy cost to form a sharp magnetic DW in the y - z plane in the bulk structure. Similar to the Y-wall shown in Fig. 6.4(d), one third of the edge-sharing and corner-sharing exchange interactions are between different domains, which contribute to the magnetic energy at the DW. The explicit form of the magnetic energy between two columns at the DW is written as

$$E_{\text{Mdw}} = J_c(S_{A_2} \cdot S_{\bar{B}} + S_B \cdot S_{\bar{A}_2}) + 2J_c(S_{A_1} \cdot S_{\bar{A}_2} + S_{A_2} \cdot S_{\bar{A}_1}) + J_e(S_{A_1} \cdot S_{\bar{B}} + S_B \cdot S_{\bar{A}_1}). \quad (6.2)$$

Here the notation \bar{A}_1 means the A_1 cation on the other side of the DW. For the $udu\text{-}dud$ magnetic DW, $E_{\text{Mdw}} = 6J_c - 2J_e$. As a reference, if the magnetic orders are the same on both sides, i.e. $udu\text{-}udu$, which does not have a magnetic DW, $E_{\text{Mdw}} = -6J_c + 2J_e$. Therefore, the energy cost to form a $udu\text{-}dud$ magnetic DW is $2 \times (6J_c - 2J_e) = 14.8 \text{ meV}$. First-principles calculation on the $udu\text{-}dud$ magnetic DW in the bulk structure suggests that the magnetic DW energy is 13.9 meV , showing excellent agreement with results from the spin model.

Next, we use the obtained parameters to estimate the magnetic DW energy at the FE DW structure. The exchange-interaction map between column C2 in the $B'A_1-BA_2$ -domain and columns $\overline{C1}$ and $\overline{C3}$ in the $B'-A_2B-A_1$ domain at the DW structure are shown in Fig. 6.6(b). Here we see that the exchange interactions at FE DWs are quite different from the ones in the bulk structure, and the magnetic energy between two columns at the FE DW is

$$E_{\text{FEdw}} = J_c(S_{A_2} \cdot S_{\overline{B}} + S_B \cdot S_{\overline{A_2}}) + J_c(S_{A_1} \cdot S_{\overline{A_2}} + S_{A_2} \cdot S_{\overline{A_1}}) \\ + J_e(S_{A_1} \cdot S_{\overline{B}} + S_B \cdot S_{\overline{A_1}}) + J_e(S_{A_1} \cdot S_{\overline{A_1}} + S_{A_2} \cdot S_{\overline{A_2}}). \quad (6.3)$$

For the magnetic order $udu-dud$, $E_{\text{FEdw}} = 4(J_c - J_e)$, while for the magnetic order $udu-udu$, $E_{\text{FEdw}} = 4(J_e - J_c)$. As $J_e > J_c$, the $udu-dud$ FE DW is more stable, which agrees with our first-principles results qualitatively. However, quantitatively, the energy difference between the two types of magnetic orders at FE DW is 10 meV from calculation, but the spin model overestimates the energy difference as $8(J_e - J_c) = 26.4$ meV. This discrepancy comes from the rough approximation that there is only one J_c value and one J_e value, which neglects the significant change of atomic environment at the FE DW.

In the above calculations, the magnetic DW is assumed to be as sharp as the FE DW, but in most magnetic materials, their magnetic DWs are much thicker. Then should we also consider a thick magnetic DW instead? In most ferromagnetic DWs, the exchange energy prefers a gradual change of spin directions at the DW, but the magnetic anisotropy favors an abrupt change of spin directions at the DW. Thus, in the case of strong exchange and weak spin anisotropy, magnetic DWs are much wider than FE DWs. However, in udu Mn_3WO_6 , because of the distinct structure at the FE DW, the exchange energy also prefers the spins to align oppositely across the DW, i.e. $udu-dud$. Therefore, both exchange energy and anisotropy support the sharp magnetization change at the FE DW.

6.3.4 Domain wall reversal

The polarization reversal at the DW is accompanied with DW motions. For instance, in the 4+4 supercell illustrated in Fig. 6.7(a), the simultaneous polarization reversal at

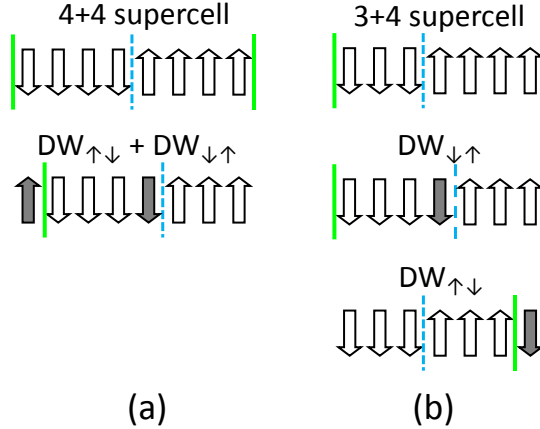


Figure 6.7: Illustrations of DW motions in 4+4 and 3+4 supercells. The upward and downward arrows represent the polarization in each unit cell. The dashed blue line represents the $DW_{\downarrow\uparrow}$ and the solid green line is the $DW_{\uparrow\downarrow}$. The filled black arrows represent the polarization that are reversed during the DW motion.

the 1st and the 5th cells (black arrows) makes the $DW_{\uparrow\downarrow}$ and $DW_{\downarrow\uparrow}$ move to the right by one unit cell. Similarly, in the 3+4 supercell shown in Fig. 6.7(b), the polarization reversal at the 4th cell is accompanied with the rightward motion of the $DW_{\downarrow\uparrow}$, and the polarization reversal at the 7th cell leads to the leftward motion of the $DW_{\uparrow\downarrow}$. In order to make sure that the supercell before and after the polarization reversal is equivalent, the $m + m$ supercell always involves the motion of two DWs, while the $m + (m + 1)$ supercell can disentangle the motion of the two DWs. Therefore, for LNO-type structures, either $m + m$ or $m + (m + 1)$ supercells can be used, while for ordered-LNO structures, only $m + (m + 1)$ supercells are used to calculate the DW-mediated FE reversal for the distinct $DW_{\uparrow\downarrow}$ and $DW_{\downarrow\uparrow}$.

The adiabatic polarization reversal at the DW is achieved by using the reaction coordinate $\xi_1 + \xi_2$ as a structural constraint and applying it only to the unit cell at the DW. The energy profiles of the DW-mediated reversal of selected materials are illustrated in Fig. 6.8(a), and the reversal barriers are listed in Table. 6.2. Comparing with the coherent reversal barrier reported at Table 5.8 in Chapter 5, the DW-mediated barrier is much lower in energy. For instance, the coherent barrier of LiTaO_3 is 129 meV while the DW-mediated barrier is only 55 meV. This huge energy reduction is caused

Table 6.2: DW-mediated polarization reversal barrier E_{barrier} for corundum derivatives. The energy barriers of $DW_{\uparrow\downarrow}$ and $DW_{\downarrow\uparrow}$ are the same in LNO-type structures, but different in ordered-LNO structure. The unit of E_{barrier} is meV per unit cell.

LNO-type	Magnetic order	$\uparrow\downarrow=\downarrow\uparrow$	Ordered LNO	Magnetic order	$\uparrow\downarrow$	$\downarrow\uparrow$
LiTaO ₃		55	Li ₂ ZrTeO ₆		28	39
LiNbO ₃		98	Li ₂ HfTeO ₆		32	42
ZnSnO ₃		86	Mn ₃ WO ₆	<i>uud-uud</i>	210	161
MnTiO ₃	<i>ud-ud</i>	229	Mn ₃ WO ₆	<i>udu-dud</i>	212	181
			Mn ₃ WO ₆	<i>udu-udu</i>	207	175

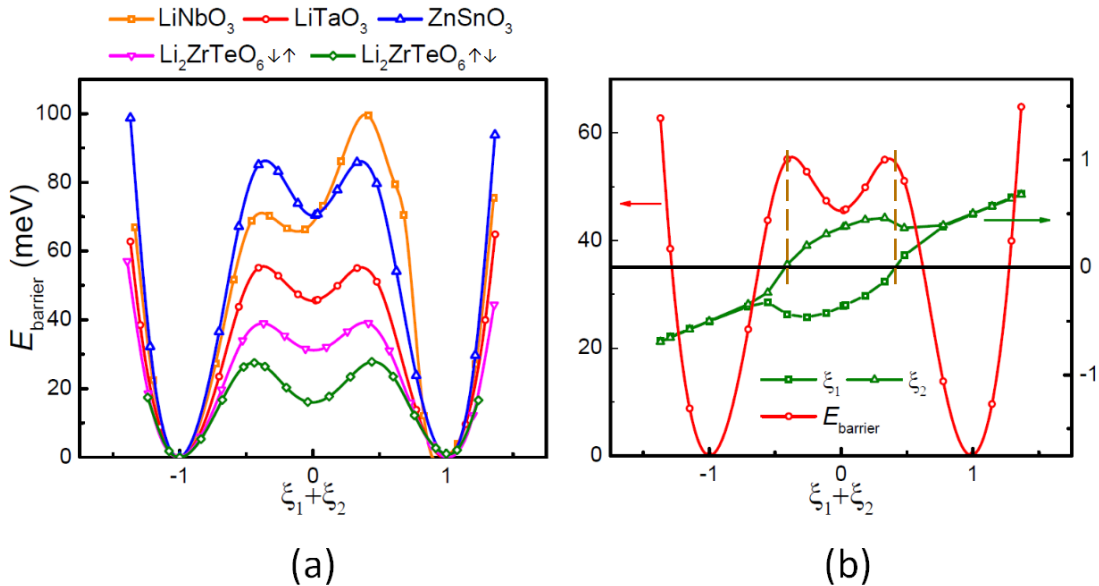


Figure 6.8: DW-mediated FE reversal in corundum derivatives. (a) Energy profiles of the DW reversal for selected corundum derivatives. The results of both the $DW_{\downarrow\uparrow}$ and $DW_{\uparrow\downarrow}$ are included for Li₂ZrTeO₆. The unit of energy is meV per unit cell. (b) Energy profile of the DW reversal in LiTaO₃ and the evolution of ξ_1 and ξ_2 . The dashed brown lines highlight the position when $\xi_1 = 0$ and $\xi_2 = 0$.

by the distinct structure at the DW. Since the symmetry at the DW is much lower than that in the bulk, there are more phonon modes, e.g., the breathing modes of the oxygen triangle, that can undergo displacement to lower the energy barrier. Moreover, the energy profile shown in Fig. 6.8 is symmetric with respect to $\xi_1 + \xi_2 = 0$ for most candidates, as their DW structures have inversion symmetry at $\xi_1 + \xi_2 = 0$. The only asymmetric profile in Fig. 6.8 is that of LiNbO_3 . This is caused by an in-plane unstable polar mode at the midpoint structure, which breaks the local inversion symmetry at $\xi_1 + \xi_2 = 0$. This unstable E_u mode in LiNbO_3 has also been previously reported in the literature [125].

In Fig. 6.8(b), we use results of LiTaO_3 as an example to clarify the relationship between the energy profile and the evolution of ξ_1 (or ξ_2) at the DW. Similar to the results in Chapter 5, $\xi_1 \neq \xi_2$ when the reaction coordinate $\xi_1 + \xi_2$ approaches zero. However, the barrier structures of DW-mediated reversal are qualitatively different from that of the coherent reversal. For the coherent reversal, the energy reaches the maximum at $\xi_1 + \xi_2 = 0$ in most cases. In contrast, the DW-mediated energy profile has two energy maxima located at approximately $\xi_1 = 0$ and $\xi_2 = 0$, as highlighted by the dashed vertical lines in Fig. 6.8(b). Those are the moments when one of the A cations is passing through the oxygen plane. Meanwhile, the saddle point at $\xi_1 + \xi_2 = 0$ in the coherent reversal becomes a local minimum in the DW-mediated reversal.

For magnetic compounds, their DW motions may be accompanied by spin flips at DWs. In the reversal process, the A_1 cation migrates away from the B' cation and becomes face sharing with the B cation. Similarly, the A_2 cation moves away from the B cation and forms face-sharing octahedron with the B' cation. Therefore, A_1 interchanges with A_2 , and e.g., udu magnetic order becomes dud in Mn_3WO_6 . In order to arrive at the magnetic ground state, either the spins on both A_1 and A_2 cations flip so that dud becomes udu , or the spin on B cation flips so that dud becomes dud . The former case happens at the udu - udu DW, and the latter case happens at the udu - dud DW.

The above-mentioned first-principles methods can be used to predict the DW-mediated reversal barrier in any corundum derivative, but it would be more valuable

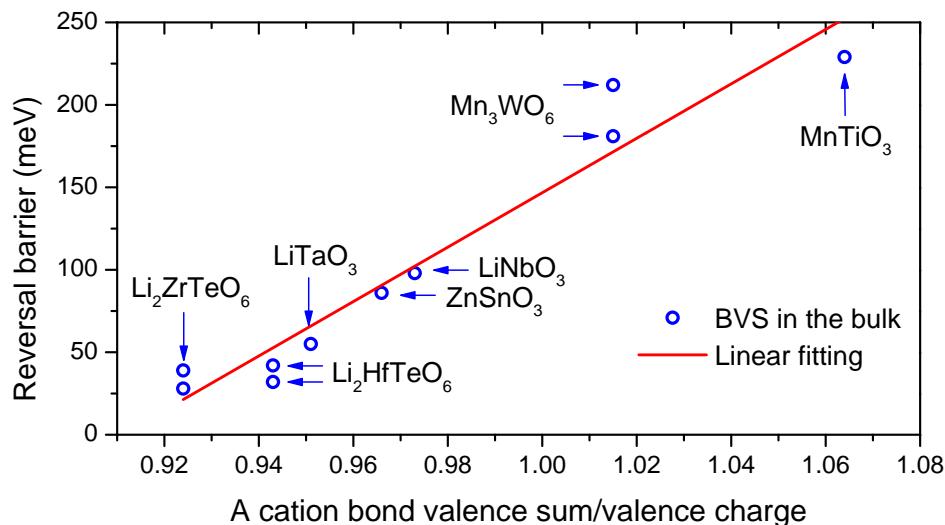


Figure 6.9: BVS of A cations *versus* DW-mediated reversal barriers. The linear fitting parameters are $a = 147$ meV and $b = 1650$ meV for $y = a + b(x - 1)$.

if some intuitive rules of thumb can be summarized to enhance our understanding. In the discussion of polar metal LiOsO_3 , which is also a corundum derivative, it has been pointed out that the polar distortion in metallic LiOsO_3 is driven by short-range interactions [131], or from the crystal chemistry point of view, it is caused by the local bonding preference of Li cations [144]. As the Li cations are loosely bonded in the centrosymmetric structure, they prefer a polar distortion to strengthen the local bonding environment. Because of the structural similarity between metallic LiOsO_3 and other insulating corundum derivatives, it is worthwhile to investigate the relationship between the bonding environment of A cations and the DW-mediated reversal barrier.

The local bonding of the A cation can be described by the empirical bond valence sum (BVS) through the equation [145]

$$V_{\text{BVS}} = \sum_i \exp[(R_0 - R_i)/b]. \quad (6.4)$$

The BVS estimates the number of electrons that are associated with the local bonds. Here R_i is the bond length between A cations and the i th nearest neighboring oxygen anions, R_0 is a tabulated parameter expressing the ideal bond length when the A cation has exactly valence 1, and b is an empirical constant 0.37 \AA . For ordered-LNO structures,

the two A cations are inequivalent. Instead of using the average BVS of two A cations, it is more relevant to only consider the A cation that is closer to the oxygen plane, because that is the one that would migrate first in the reversal process. Using the bond-length values extracted from bulk structures and Eq. (6.4), we plot the energy barrier *versus* the normalized V_{BVS} in Fig. 6.9. A roughly linear relationship is observed between the normalized V_{BVS} of A cations and DW-mediated reversal barriers, which also implies the dominance of short-range interactions in the corundum derivatives. Similarly, the bond valence model has also been used successfully in molecular dynamics simulations of ferroelectric PbTiO_3 in the previous literature [146].

6.4 Summary and outlook

A DW is a topological defect and it may exhibit rich physics that is not present in the bulk. FE DWs are the ones sandwiched between two polar domains. In this chapter, we have studied the properties of FE DWs in corundum derivatives. The mobile 180° charged-neutral DWs are constructed by interchanging A and vacancy sublattices while preserving B/B' and O sublattices. Interestingly, it is found that the mobile FE domains are interlocked with chirality domains, and the FE DW is also a chiral DW. For the orientation of DWs, our calculations suggest that the Y-wall that is in the y - z plane is more stable than the X-wall in the x - z plane. In addition, we have also considered the magnetic orders at the DW, and found that in Mn_3WO_6 with magnetic order udu , the domains with opposite polarization also have opposite magnetization, and the coupling is from the exchange-striction interaction at the DW. Therefore both the polarization and magnetization can be controlled by an electric field. Since the FE polarization reversal is achieved through DW motion, we have also studied the DW-mediated polarization reversal barriers by applying structural constraints at the DW. It is found that the DW-mediated reversal barrier is linearly correlated with the BVS of A cations. As the local bonding environment can be directly measured in experiments, the linear relationship can be used as a rough prediction of the DW-mediated reversal barrier and find new FEs.

Besides the FE DWs that we have studied, there are also many interesting properties

at DWs that are worthwhile to investigate, e.g., the purely chiral DWs. Meanwhile, the coupling between polarization and magnetization at the *udu-dud* DW in Mn_3WO_6 is sensitive to the magnetic order. As the magnetic structure of Mn_3WO_6 is still under investigation [126], it is possible that the actual magnetic structure has a larger magnetic cell that is similar to Ni_3TeO_6 , or even a non-collinear magnetic order instead of a collinear *udu* magnetic order. However, similar magnetoelectric mechanisms at DWs may still exist in other corundum derivatives.

Chapter 7

Conclusion and outlook

In this thesis, we have studied the magnetoelectric (ME) and ferroelectric (FE) properties in several complex oxides. The dynamical magnetic charge tensors that we systematically studied in Chapter 3 and Chapter 4 can be used as indicators of the coupling strength between the magnetization and lattice distortions. We expect the dynamical magnetic charge tensors to be important not only in insulating ME materials, but also in magnetic insulators and even metals. On the other hand, the structural constraint methods that we used in Chapter 5 and Chapter 6 can be applied to estimate the coherent barriers and the DW-mediated FE reversal barriers in the family of corundum derivatives. Moreover, our study of the mobile FE DW sheds light on the possible atomic structures and even ME couplings at DWs.

Although FE properties has been studied for several decades, there are still many open questions that are worth investigating. Firstly, along with the intense studies of two-dimensional (2D) or quasi-2D materials, some of them are theoretically proposed to be FEs [147, 148, 149]. We think that the FE properties in 2D and the one-dimensional FE domain walls may exhibit different properties compared with the three-dimensional FEs and 2D FE domain walls.

Secondly, most theoretical studies of ferroelectricity and ME effects focus on weakly correlated materials, because of the limitations of the density-functional methods in dealing with strongly correlated systems. Recently, the bulk polarization has been rewritten in terms of the Green's functions [150], and the method has been implemented [151] in the dynamical mean-field theory [152], which is a method to determine the electronic structure of strongly correlated materials. Therefore, we think that the new method can lead to the discovery of novel mechanisms of ferroelectricity and ME effects

from the electron correlations.

The field of ME effects and multiferroics keeps expanding, and here we enumerate a few interesting research directions. Since the spin-orbit coupling of $4d$ and $5d$ electrons is much larger than those in $3d$ transition-metal cations, the ME coupling in those materials are worth studying. In addition, our study of the FE domain walls suggests that the ME effects at DWs is also a possible future direction. Moreover, there are discussions on the ME monopoles [153] and their connections to spin ice systems [154].

On the other hand, theoretical discussions of the dynamical ME effects are very limited. The electric and magnetic responses are in general frequency- and momentum-dependent, and they have very definite physical meanings. For example, the dielectric function

$$\epsilon(\mathbf{q}, \omega) = \sum_i \frac{S_i}{\omega^2 - \omega_i^2(\mathbf{q})} \quad (7.1)$$

has poles at frequencies $\omega_i(\mathbf{q})$, which correspond to dipole-active collective excitations, such as optical phonons. Similarly, the poles of magnetic susceptibility $\chi(\mathbf{q}, \omega)$ are magnetic excitations, such as spin waves. The ME coupling $\alpha(\mathbf{q}, \omega)$ is also a function of wave vector \mathbf{q} and frequency ω . The static ME effects that we have studied are the properties at $\mathbf{q} = 0$, $\omega = 0$, but there are more rich dynamical properties at $\mathbf{q} \neq 0$, $\omega \neq 0$ that are waiting to be explored.

From a symmetry perspective, the antisymmetric components of the ME tensor can be written as a pseudovector \mathbf{T} that couples to the electric and magnetic fields through $\mathbf{T} \cdot (\mathcal{E} \times \mathbf{H})$. This \mathbf{T} is related to the magnetic toroidal moments [155]. Since the propagation direction of light \mathbf{k} is determined by the cross product of the electric field and the magnetic field, the ME pseudovector \mathbf{T} couples to the propagation direction through $\mathbf{T} \cdot \mathbf{k}$, and leads to non-reciprocal effects at certain frequencies. If the microscopic origin of the dynamical ME effect is from the electronic sector at the energy scale of a few electron volts, it can induce a significant optical non-reciprocal effect [156]. If the ME excitation is from electromagnons, which are magnons that mixed with certain phonon oscillations, non-reciprocal propagation of spin waves can be observed at terahertz frequency [157, 158].

In short, the fields of ferroelectricity and magnetoelectric effects are still very active, and many new research directions are connected with these fields. Meanwhile, first-principles computational theories will continue to provide insights into the microscopic mechanisms. Along with the rapid developments of computational science and computational methods, the first-principles computational theories will play a more important role in predicting new materials, structures and functionalities in the near future.

References

- [1] J. Valasek. Piezo-electric and allied phenomena in rochelle salt. *Phys. Rev.*, 17:475–481, Apr 1921.
- [2] Nicola A Spaldin and Manfred Fiebig. The renaissance of magnetoelectric multiferroics. *Science*, 309(5733):391–392, 2005.
- [3] Karin M. Rabe, Charles H Ahn, and Jean-Marc Triscone. *Physics of Ferroelectrics*, volume 105. Springer-Verlag Berlin Heidelberg, 1 edition, 2007.
- [4] James F. Scott. *Ferroelectric Memories*, volume 3. Springer-Verlag Berlin Heidelberg, 1 edition, 2000.
- [5] Manfred Fiebig. Revival of the magnetoelectric effect. *Journal of Physics D: Applied Physics*, 38(8):R123, 2005.
- [6] Claude Ederer and Nicola A. Spaldin. Recent progress in first-principles studies of magnetoelectric multiferroics. *Current Opinion in Solid State and Materials Science*, 9(3):128 – 139, 2005.
- [7] W. Eerenstein, N. D. Mathur, and James F. Scott. Multiferroic and magnetoelectric materials. *nature*, 442(7104):759–765, 2006.
- [8] Y. Tokura. Multiferroics - toward strong coupling between magnetization and polarization in a solid. *Journal of Magnetism and Magnetic Materials*, 310(2, Part 2):1145 – 1150, 2007. Proceedings of the 17th International Conference on MagnetismThe International Conference on Magnetism.
- [9] George K Horton and Alexei Alexei Maradudin. *Dynamical properties of solids*, volume 3. North-Holland, 1980.
- [10] Xavier Gonze and Changyol Lee. Dynamical matrices, born effective charges, dielectric permittivity tensors, and interatomic force constants from density-functional perturbation theory. *Phys. Rev. B*, 55:10355–10368, Apr 1997.
- [11] Kevin F. Garrity, Karin M. Rabe, and David Vanderbilt. Hyperferroelectrics: Proper ferroelectrics with persistent polarization. *Phys. Rev. Lett.*, 112:127601, Mar 2014.
- [12] Jeroen van den Brink and Daniel I Khomskii. Multiferroicity due to charge ordering. *Journal of Physics: Condensed Matter*, 20(43):434217, 2008.
- [13] Kunihiko Yamauchi and Paolo Barone. Electronic ferroelectricity induced by charge and orbital orderings. *Journal of Physics: Condensed Matter*, 26(10):103201, 2014.

- [14] Annette Bussmann-Holder and Naresh Dalal. Order/disorder versus or with displacive dynamics in ferroelectric systems. In *Ferro-and Antiferroelectricity*, pages 1–21. Springer, 2006.
- [15] Craig J. Fennie and Karin M. Rabe. Ferroelectric transition in YMnO_3 from first principles. *Phys. Rev. B*, 72:100103, Sep 2005.
- [16] T Kimura, T Goto, H Shintani, K Ishizaka, T Arima, and Y Tokura. Magnetic control of ferroelectric polarization. *nature*, 426(6962):55–58, 2003.
- [17] Pierre Curie. On symmetry in physical phenomena, symmetry of an electric field and of a magnetic field. *Journal de Physique*, 3:401, 1894.
- [18] AV Shubnikov. Symmetry and antisymmetry of finite figures. *USSR Academy of Sciences, Moscow*, 1951.
- [19] L.D. Landau, E.M. Lifshits, E.M. Lifshits, and Pitaevskiĭ. *Electrodynamics of continuous media*.
- [20] Franz Ernst Neumann and Oskar Emil Meyer. *Vorlesungen über die Theorie der Elasticität der festen Körper und des Lichtäthers: gehalten an der Universität Königsberg*, volume 5. BG Teubner, 1885.
- [21] J.-P. Rivera. A short review of the magnetoelectric effect and related experimental techniques on single phase (multi-) ferroics. *The European Physical Journal B*, 71(3):299–313, 2009.
- [22] IE Dzyaloshinskii. On the magneto-electrical effect in antiferromagnets, 1960.
- [23] DN Astrov. The magnetoelectric effect in antiferromagnetics. *Sov. Phys. JETP*, 11(3):708–709, 1960.
- [24] DN Astrov. Magnetoelectric effect in chromium oxide. *Sov. Phys. JETP*, 13(4):729–733, 1961.
- [25] GT Rado and VJ Folen. Observation of the magnetically induced magnetoelectric effect and evidence for antiferromagnetic domains. *Physical Review Letters*, 7(8):310, 1961.
- [26] VJ Folen, GT Rado, and EW Stalder. Anisotropy of the magnetoelectric effect in Cr_2O_3 . *Physical Review Letters*, 6(11):607, 1961.
- [27] GA Smolenskii, VA Isupov, NN Krainik, and AL Agranovskaya. Concerning the coexistence of the ferroelectric and ferrimagnetic states. *Izvestiya Rossijskoj Akademii Nauk. Seriya Fizika Atmosfery i Okeana*, 25:1333, 1961.
- [28] Edgar Ascher, Harry Rieder, Hans Schmid, and H Stössel. Some properties of ferromagnetoelectric nickel-iodine boracite, $\text{Ni}_3\text{B}_7\text{O}_{13}\text{I}$. *Journal of Applied Physics*, 37(3):1404–1405, 1966.
- [29] W. F. Brown, R. M. Hornreich, and S. Shtrikman. Upper bound on the magnetoelectric susceptibility. *Phys. Rev.*, 168:574–577, Apr 1968.

- [30] Thomas Henry O'Dell. *The electrodynamics of magneto-electric media*, volume 11. North-Holland Publishing Company, 1970.
- [31] Hans Schmid. Multi-ferroic magnetoelectrics. *Ferroelectrics*, 162(1):317–338, 1994.
- [32] Nicola A. Hill. Why are there so few magnetic ferroelectrics? *The Journal of Physical Chemistry B*, 104(29):6694–6709, 2000.
- [33] J. Wang, J. B. Neaton, H. Zheng, V. Nagarajan, S. B. Ogale, B. Liu, D. Viehland, V. Vaithyanathan, D. G. Schlom, U. V. Waghmare, N. A. Spaldin, K. M. Rabe, M. Wuttig, and R. Ramesh. Epitaxial bifeo₃ multiferroic thin film heterostructures. *Science*, 299(5613):1719–1722, 2003.
- [34] R. D. King-Smith and David Vanderbilt. Theory of polarization of crystalline solids. *Phys. Rev. B*, 47:1651–1654, Jan 1993.
- [35] Hena Das, Aleksander L Wysocki, Yanan Geng, Weida Wu, and Craig J Fennie. Bulk magnetoelectricity in the hexagonal manganites and ferrites. *Nature communications*, 5, 2014.
- [36] Lev Davidovich Landau, Evgenii Mikhailovich Lifshitz, JB Sykes, John Stewart Bell, and ME Rose. Quantum mechanics, non-relativistic theory. *Physics Today*, 11:56, 1958.
- [37] I. Dzyaloshinsky. A thermodynamic theory of weak ferromagnetism of antiferromagnetics. *Journal of Physics and Chemistry of Solids*, 4(4):241 – 255, 1958.
- [38] Tôru Moriya. Anisotropic superexchange interaction and weak ferromagnetism. *Phys. Rev.*, 120:91–98, Oct 1960.
- [39] John B. Goodenough. Theory of the role of covalence in the perovskite-type manganites [La, m(II)]Mno₃. *Phys. Rev.*, 100:564–573, Oct 1955.
- [40] Junjiro Kanamori. Superexchange interaction and symmetry properties of electron orbitals. *Journal of Physics and Chemistry of Solids*, 10(2):87 – 98, 1959.
- [41] Meng Ye and David Vanderbilt. Dynamical magnetic charges and linear magnetoelectricity. *Phys. Rev. B*, 89:064301, Feb 2014.
- [42] Meng Ye and David Vanderbilt. Magnetic charges and magnetoelectricity in hexagonal rare-earth manganites and ferrites. *Phys. Rev. B*, 92:035107, Jul 2015.
- [43] Meng Ye and David Vanderbilt. Ferroelectricity in corundum derivatives. *Phys. Rev. B*, 93:134303, Apr 2016.
- [44] Man-Rong Li, Mark Croft, Peter W. Stephens, Meng Ye, David Vanderbilt, Maria Retuerto, Zheng Deng, Christoph P. Grams, Joachim Hemberger, Joke Hadermann, Wen-Min Li, Chang-Qing Jin, Felix O. Saouma, Joon I. Jang, Hirofumi Akamatsu, Venkatraman Gopalan, David Walker, and Martha Greenblatt. Mn₂fewo₆: A new ni₃teo₆-type polar and magnetic oxide. *Advanced Materials*, 27(13):2177–2181, 2015.

- [45] Richard M Martin. *Electronic structure: basic theory and practical methods*. Cambridge university press, 2004.
- [46] P. Hohenberg and W. Kohn. Inhomogeneous electron gas. *Phys. Rev.*, 136:B864–B871, Nov 1964.
- [47] W. Kohn and L. J. Sham. Self-consistent equations including exchange and correlation effects. *Phys. Rev.*, 140:A1133–A1138, Nov 1965.
- [48] J. P. Perdew and Alex Zunger. Self-interaction correction to density-functional approximations for many-electron systems. *Phys. Rev. B*, 23:5048–5079, May 1981.
- [49] John P. Perdew and Yue Wang. Accurate and simple analytic representation of the electron-gas correlation energy. *Phys. Rev. B*, 45:13244–13249, Jun 1992.
- [50] John P. Perdew, Kieron Burke, and Matthias Ernzerhof. Generalized gradient approximation made simple. *Phys. Rev. Lett.*, 77:3865–3868, Oct 1996.
- [51] John P. Perdew, Adrienn Ruzsinszky, Gábor I. Csonka, Oleg A. Vydrov, Gustavo E. Scuseria, Lucian A. Constantin, Xiaolan Zhou, and Kieron Burke. Restoring the density-gradient expansion for exchange in solids and surfaces. *Phys. Rev. Lett.*, 100:136406, Apr 2008.
- [52] Axel D. Becke. A new mixing of hartreefock and local densityfunctional theories. *The Journal of Chemical Physics*, 98(2), 1993.
- [53] S. L. Dudarev, G. A. Botton, S. Y. Savrasov, C. J. Humphreys, and A. P. Sutton. Electron-energy-loss spectra and the structural stability of nickel oxide: An lsdau study. *Phys. Rev. B*, 57:1505–1509, Jan 1998.
- [54] A. I. Liechtenstein, V. I. Anisimov, and J. Zaanen. Density-functional theory and strong interactions:orbital ordering in mott-hubbard insulators. *Phys. Rev. B*, 52:R5467–R5470, Aug 1995.
- [55] Andrei Malashevich. *First-principles study of electric polarization in piezoelectric and magnetoelectric materials*. PhD thesis, Rutgers University-Graduate School-New Brunswick, 2009.
- [56] G. Kresse and J. Furthmüller. Efficient iterative schemes for *ab initio* total-energy calculations using a plane-wave basis set. *Phys. Rev. B*, 54:11169–11186, Oct 1996.
- [57] Paolo Giannozzi, Stefano Baroni, Nicola Bonini, Matteo Calandra, Roberto Car, Carlo Cavazzoni, Davide Ceresoli, Guido L Chiarotti, Matteo Cococcioni, Ismaila Dabo, Andrea Dal Corso, Stefano de Gironcoli, Stefano Fabris, Guido Fratesi, Ralph Gebauer, Uwe Gerstmann, Christos Gougoussis, Anton Kokalj, Michele Lazzeri, Layla Martin-Samos, Nicola Marzari, Francesco Mauri, Riccardo Mazzarello, Stefano Paolini, Alfredo Pasquarello, Lorenzo Paulatto, Carlo Sbraccia, Sandro Scandolo, Gabriele Sclausero, Ari P Seitsonen, Alexander Smogunov, Paolo Umari, and Renata M Wentzcovitch. Quantum espresso: a modular and open-source software project for quantum simulations of materials. *Journal of Physics: Condensed Matter*, 21(39):395502, 2009.

- [58] Peter Schwerdtfeger. The pseudopotential approximation in electronic structure theory. *ChemPhysChem*, 12(17):3143–3155, 2011.
- [59] D. R. Hamann, M. Schlüter, and C. Chiang. Norm-conserving pseudopotentials. *Phys. Rev. Lett.*, 43:1494–1497, Nov 1979.
- [60] David Vanderbilt. Soft self-consistent pseudopotentials in a generalized eigenvalue formalism. *Phys. Rev. B*, 41:7892–7895, Apr 1990.
- [61] P. E. Blöchl. Projector augmented-wave method. *Phys. Rev. B*, 50:17953–17979, Dec 1994.
- [62] R. Resta. Theory of the electric polarization in crystals. *Ferroelectrics*, 136(1):51–55, 1992.
- [63] Raffaele Resta. Macroscopic polarization in crystalline dielectrics: the geometric phase approach. *Rev. Mod. Phys.*, 66:899–915, Jul 1994.
- [64] R Clausius. *Die Mechanische Behandlung der Electricität*, volume 2. Vieweg+Teubner Verlag, 1879.
- [65] Turan Birol, Nicole A. Benedek, Hena Das, Aleksander L. Wysocki, Andrew T. Mulder, Brian M. Abbett, Eva H. Smith, Saurabh Ghosh, and Craig J. Fennie. The magnetoelectric effect in transition metal oxides: Insights and the rational design of new materials from first principles. *Current Opinion in Solid State and Materials Science*, 16(5):227 – 242, 2012.
- [66] Jorge Íñiguez. First-principles approach to lattice-mediated magnetoelectric effects. *Phys. Rev. Lett.*, 101:117201, Sep 2008.
- [67] Jacek C. Wojdeł and Jorge Íñiguez. Magnetoelectric response of multiferroic bifeo₃ and related materials from first-principles calculations. *Phys. Rev. Lett.*, 103:267205, Dec 2009.
- [68] Jacek C. Wojdeł and Jorge Íñiguez. *Ab Initio* indications for giant magnetoelectric effects driven by structural softness. *Phys. Rev. Lett.*, 105:037208, Jul 2010.
- [69] Eric Bousquet, Nicola A. Spaldin, and Kris T. Delaney. Unexpectedly large electronic contribution to linear magnetoelectricity. *Phys. Rev. Lett.*, 106:107202, Mar 2011.
- [70] A. Scaramucci, E. Bousquet, M. Fechner, M. Mostovoy, and N. A. Spaldin. Linear magnetoelectric effect by orbital magnetism. *Phys. Rev. Lett.*, 109:197203, Nov 2012.
- [71] T. Thonhauser, Davide Ceresoli, David Vanderbilt, and R. Resta. Orbital magnetization in periodic insulators. *Phys. Rev. Lett.*, 95:137205, Sep 2005.
- [72] R. Resta, Davide Ceresoli, T. Thonhauser, and David Vanderbilt. Orbital magnetization in extended systems. *ChemPhysChem*, 6(9):1815–1819, 2005.
- [73] Andrew M. Essin, Ari M. Turner, Joel E. Moore, and David Vanderbilt. Orbital magnetoelectric coupling in band insulators. *Phys. Rev. B*, 81:205104, May 2010.

- [74] Andrei Malashevich, Sinisa Coh, Ivo Souza, and David Vanderbilt. Full magnetoelectric response of Cr_2O_3 from first principles. *Phys. Rev. B*, 86:094430, Sep 2012.
- [75] Raffaele Resta. Lyddane-sachs-teller relationship in linear magnetoelectrics. *Phys. Rev. Lett.*, 106:047202, Jan 2011.
- [76] R. Resta. Zone-center dynamical matrix in magnetoelectrics. *Phys. Rev. B*, 84:214428, Dec 2011.
- [77] Kris T. Delaney, Maxim Mostovoy, and Nicola A. Spaldin. Superexchange-driven magnetoelectricity in magnetic vortices. *Phys. Rev. Lett.*, 102:157203, Apr 2009.
- [78] Xifan Wu, David Vanderbilt, and D. R. Hamann. Systematic treatment of displacements, strains, and electric fields in density-functional perturbation theory. *Phys. Rev. B*, 72:035105, Jul 2005.
- [79] N. Troullier and José Luís Martins. Efficient pseudopotentials for plane-wave calculations. *Phys. Rev. B*, 43:1993–2006, Jan 1991.
- [80] Di Xiao, Junren Shi, and Qian Niu. Berry phase correction to electron density of states in solids. *Phys. Rev. Lett.*, 95:137204, Sep 2005.
- [81] Davide Ceresoli, T. Thonhauser, David Vanderbilt, and R. Resta. Orbital magnetization in crystalline solids: Multi-band insulators, chern insulators, and metals. *Phys. Rev. B*, 74:024408, Jul 2006.
- [82] Zhongqin Yang, Zhong Huang, Ling Ye, and Xide Xie. Influence of parameters U and J in the $\text{lsda}+U$ method on electronic structure of the perovskites LaMO_3 ($m = \text{Cr, Mn, Fe, Co, Ni}$). *Phys. Rev. B*, 60:15674–15682, Dec 1999.
- [83] Adrian H. Hill, Andrew Harrison, Calum Dickinson, Wuzong Zhou, and Winfried Kockelmann. Crystallographic and magnetic studies of mesoporous eskolaite. *Microporous and Mesoporous Materials*, 130(13):280 – 286, 2010.
- [84] G. Lucovsky, R. J. Sladek, and J. W. Allen. Infrared-active phonons in Cr_2O_3 . *Phys. Rev. B*, 16:4716–4718, Nov 1977.
- [85] Simon Foner. High-field antiferromagnetic resonance in Cr_2O_3 . *Phys. Rev.*, 130:183–197, Apr 1963.
- [86] Sang-Wook Cheong and Maxim Mostovoy. Multiferroics: a magnetic twist for ferroelectricity. *Nature materials*, 6(1):13–20, 2007.
- [87] A Pimenov, AA Mukhin, V Yu Ivanov, VD Travkin, AM Balbashov, and A Loidl. Possible evidence for electromagnons in multiferroic manganites. *Nature Physics*, 2(2):97–100, 2006.
- [88] Maxim Mostovoy. Multiferroics: A whirlwind of opportunities. *Nature materials*, 9(3):188–190, 2010.
- [89] Bas B Van Aken, Thomas TM Palstra, Alessio Filippetti, and Nicola A Spaldin. The origin of ferroelectricity in magnetoelectric ymno_3 . *Nature materials*, 3(3):164–170, 2004.

- [90] Craig J. Fennie and Karin M. Rabe. Ferroelectric transition in YMnO_3 from first principles. *Phys. Rev. B*, 72:100103, Sep 2005.
- [91] T Choi, Y Horibe, HT Yi, YJ Choi, Weida Wu, and S-W Cheong. Insulating interlocked ferroelectric and structural antiphase domain walls in multiferroic ymno_3 . *Nature materials*, 9(3):253–258, 2010.
- [92] Yu Kumagai and Nicola A Spaldin. Structural domain walls in polar hexagonal manganites. *Nature communications*, 4:1540, 2013.
- [93] Sergey Artyukhin, Kris T Delaney, Nicola A Spaldin, and Maxim Mostovoy. Landau theory of topological defects in multiferroic hexagonal manganites. *Nature materials*, 13(1):42–49, 2014.
- [94] Shi-Zeng Lin, Xueyun Wang, Yoshitomo Kamiya, Gia-Wei Chern, Fei Fan, David Fan, Brian Casas, Yue Liu, Valery Kiryukhin, Wojciech H Zurek, et al. Topological defects as relics of emergent continuous symmetry and higgs condensation of disorder in ferroelectrics. *Nature Physics*, 10(12):970–977, 2014.
- [95] M. Fiebig, Th. Lottermoser, and R. V. Pisarev. Spin-rotation phenomena and magnetic phase diagrams of hexagonal rmno_3 . *Journal of Applied Physics*, 93(10):8194–8196, 2003.
- [96] F. Yen, C. dela Cruz, B. Lorenz, E. Galstyan, Y.Y. Sun, M. Gospodinov, and C.W. Chu. Magnetic phase diagrams of multiferroic hexagonal rmno_3 ($r = \text{er}, \text{yb}, \text{tm}, \text{and ho}$). *Journal of Materials Research*, 22:2163–2173, 8 2007.
- [97] Bernd Lorenz. Hexagonal manganites(rmno_3): class (i) multiferroics with strong coupling of magnetism and ferroelectricity. *ISRN Condensed Matter Physics*, 2013, 2013.
- [98] Yanan Geng, Hena Das, Aleksander L Wysocki, Xueyun Wang, SW Cheong, M Mostovoy, Craig J Fennie, and Weida Wu. Direct visualization of magnetoelectric domains. *Nature materials*, 13(2):163–167, 2014.
- [99] Steven M. Disseler, Julie A. Borchers, Charles M. Brooks, Julia A. Mundy, Jarrett A. Moyer, Daniel A. Hillsberry, Eric L. Thies, Dmitri A. Tenne, John Heron, Megan E. Holtz, James D. Clarkson, Gregory M. Stiehl, Peter Schiffer, David A. Muller, Darrell G. Schlom, and William D. Ratcliff. Magnetic structure and ordering of multiferroic hexagonal lufeO_3 . *Phys. Rev. Lett.*, 114:217602, May 2015.
- [100] Meng Ye and David Vanderbilt. Dynamical magnetic charges and linear magnetoelectricity. *Phys. Rev. B*, 89:064301, Feb 2014.
- [101] Ronald E Cohen. Origin of ferroelectricity in perovskite oxides. *Nature*, 358(6382):136–138, 1992.
- [102] David Vanderbilt. First-principles based modelling of ferroelectrics. *Current Opinion in Solid State and Materials Science*, 2(6):701 – 705, 1997.
- [103] V. M. Goldschmidt. Die gesetze der krystallochemie. *Naturwissenschaften*, 14(21):477–485, 1926.

- [104] Nicole A. Benedek and Craig J. Fennie. Why are there so few perovskite ferroelectrics? *The Journal of Physical Chemistry C*, 117(26):13339–13349, 2013.
- [105] Nicola A. Hill. Why are there so few magnetic ferroelectrics? *The Journal of Physical Chemistry B*, 104(29):6694–6709, 2000.
- [106] Andrew T. Mulder, Nicole A. Benedek, James M. Rondinelli, and Craig J. Fennie. Turning abo₃ antiferroelectrics into ferroelectrics: Design rules for practical rotation-driven ferroelectricity in double perovskites and a₃b₂o₇ ruddlesden-popper compounds. *Advanced Functional Materials*, 23(38):4810–4820, 2013.
- [107] Hong Jian Zhao, Wei Ren, Yurong Yang, Jorge Íñiguez, Xiang Ming Chen, and L Bellaiche. Near room-temperature multiferroic materials with tunable ferromagnetic and electrical properties. *Nature communications*, 5, 2014.
- [108] A. M. Glass and M. E. Lines. Low-temperature behavior of spontaneous polarization in linbo₃ and litao₃. *Phys. Rev. B*, 13:180–191, Jan 1976.
- [109] AW Sleight and CT Prewitt. Preparation of cunbo₃ and cutao₃ at high pressure. *Materials Research Bulletin*, 5(3):207–211, 1970.
- [110] T. Varga, A. Kumar, E. Vlahos, S. Denev, M. Park, S. Hong, T. Sanehira, Y. Wang, C. J. Fennie, S. K. Streiffer, X. Ke, P. Schiffer, V. Gopalan, and J. F. Mitchell. Coexistence of weak ferromagnetism and ferroelectricity in the high pressure linbo₃-type phase of fetio₃. *Phys. Rev. Lett.*, 103:047601, Jul 2009.
- [111] Yoshiyuki Inaguma, Masashi Yoshida, and Tetsuhiro Katsumata. A polar oxide znsno₃ with a linbo₃-type structure. *Journal of the American Chemical Society*, 130(21):6704–6705, 2008.
- [112] Yoshiyuki Inaguma, Masashi Yoshida, Takeshi Tsuchiya, Akihisa Aimi, Kie Tanaka, Tetsuhiro Katsumata, and Daisuke Mori. High-pressure synthesis of novel lithium niobate-type oxides. *Journal of Physics: Conference Series*, 215(1):012131, 2010.
- [113] Akihisa Aimi, Tetsuhiro Katsumata, Daisuke Mori, Desheng Fu, Mitsuru Itoh, Toru Kyomen, Ko-ichi Hiraki, Toshihiro Takahashi, and Yoshiyuki Inaguma. High-pressure synthesis and correlation between structure, magnetic, and dielectric properties in linbo₃-type mnmo₃ (m= ti, sn). *Inorganic chemistry*, 50(13):6392–6398, 2011.
- [114] Takahiro Kawamoto, Koji Fujita, Ikuya Yamada, Tomohiko Matoba, Sung Joo Kim, Peng Gao, Xiaoqing Pan, Scott D Findlay, Cedric Tassel, Hiroshi Kageyama, et al. Room-temperature polar ferromagnet scteo₃ transformed from a high-pressure orthorhombic perovskite phase. *Journal of the American Chemical Society*, 136(43):15291–15299, 2014.
- [115] J Choynet, A Rulmont, and P Tarte. Les tellurates mixtes li₂ zrteo₆ et li₂ hftéo₆: un nouveau phénomène d’ordre dans la famille corindon. *Journal of Solid State Chemistry*, 75(1):124–135, 1988.

- [116] R. Mathieu, S. A. Ivanov, G. V. Bazuev, M. Hudl, P. Lazor, I. V. Solovyev, and P. Nordblad. Magnetic order near 270 K in mineral and synthetic $\text{Mn}_2\text{FeSbO}_6$ ilmenite. *Applied Physics Letters*, 98(20), 2011.
- [117] Man-Rong Li, David Walker, Maria Retuerto, Tapati Sarkar, Joke Hadermann, Peter W. Stephens, Mark Croft, Alexander Ignatov, Christoph P. Grams, Joachim Hemberger, Israel Nowik, P. Shiv Halasyamani, T. Thao Tran, Swarnakamal Mukherjee, Tanusri Saha Dasgupta, and Martha Greenblatt. Polar and magnetic Mn_2FeMo_6 ($m=\text{Nb}$, Ta) with LiNbO_3 -type structure: High-pressure synthesis. *Angewandte Chemie International Edition*, 52(32):8406–8410, 2013.
- [118] Man-Rong Li, Maria Retuerto, David Walker, Tapati Sarkar, Peter W. Stephens, Swarnakamal Mukherjee, Tanusri Saha Dasgupta, Jason P. Hodges, Mark Croft, Christoph P. Grams, Joachim Hemberger, Javier Sanchez-Bentez, Ashfia Huq, Felix O. Saouma, Joon I. Jang, and Martha Greenblatt. Magnetic-structure-stabilized polarization in an above-room-temperature ferrimagnet. *Angewandte Chemie International Edition*, 53(40):10774–10778, 2014.
- [119] Man-Rong Li, Peter W. Stephens, Maria Retuerto, Tapati Sarkar, Christoph P. Grams, Joachim Hemberger, Mark C. Croft, David Walker, and Martha Greenblatt. Designing polar and magnetic oxides: $\text{Zn}_2\text{FeTaO}_6$ -in search of multiferroics. *Journal of the American Chemical Society*, 136(24):8508–8511, 2014.
- [120] Jong Yeog Son, Geunhee Lee, Moon-Ho Jo, Hyungjun Kim, Hyun M. Jang, and Young-Han Shin. Heteroepitaxial ferroelectric ZnSnO_3 thin film. *Journal of the American Chemical Society*, 131(24):8386–8387, 2009.
- [121] Craig J. Fennie. Ferroelectrically induced weak ferromagnetism by design. *Phys. Rev. Lett.*, 100:167203, Apr 2008.
- [122] X. F. Hao, A. Stroppa, S. Picozzi, A. Filippetti, and C. Franchini. Exceptionally large room-temperature ferroelectric polarization in the PbNiO_3 multiferroic nickelate: First-principles study. *Phys. Rev. B*, 86:014116, Jul 2012.
- [123] P. S. Wang, W. Ren, L. Bellaiche, and H. J. Xiang. Predicting a ferrimagnetic phase of Zn_2FeO_6 with strong magnetoelectric coupling. *Phys. Rev. Lett.*, 114:147204, Apr 2015.
- [124] Iris Inbar and R. E. Cohen. Comparison of the electronic structures and energetics of ferroelectric LiNbO_3 and LiTaO_3 . *Phys. Rev. B*, 53:1193–1204, Jan 1996.
- [125] M. Veithen and Ph. Ghosez. First-principles study of the dielectric and dynamical properties of lithium niobate. *Phys. Rev. B*, 65:214302, May 2002.
- [126] Private communication with Prof. Martha Greenblatt and Dr. Manrong Li, unpublished.
- [127] S. C. Abrahams, J. M. Reddy, and J. L. Bernstein. Ferroelectric lithium niobate. 3. single crystal x-ray diffraction study at 24 °C. *Journal of Physics and Chemistry of Solids*, 27(6-7):997–1012, 1966.

- [128] Masataka OHGAKI, Kiyooki TANAKA, and Fumiuyuki MARUMO. Anharmonic thermal vibration in a crystal of lithium (i) tantalum (v) trioxide, *litaO3*. *Mineralogical Journal*, 14(8):373–382, 1989.
- [129] K Leinenweber, J Linton, A Navrotsky, Y Fei, and JB Parise. High-pressure perovskites on the join *catio3-fetio3*. *Physics and Chemistry of Minerals*, 22(4):251–258, 1995.
- [130] Angel M Arévalo-López and J Paul Attfield. Weak ferromagnetism and domain effects in multiferroic *linbo3* 3-type *mntio3* 3-ii. *Physical Review B*, 88(10):104416, 2013.
- [131] Pengfei Li, Xinguo Ren, Guang-Can Guo, and Lixin He. The origin of hyperferroelectricity in *li b o 3* (*b*= v, nb, ta, os). *arXiv preprint arXiv:1510.06835*, 2015.
- [132] Donghwa Lee (), Haixuan Xu (), Volkmar Dierolf, Venkatraman Gopalan, and Simon R. Phillpot. Shape of ferroelectric domains in *linbo3* and *litaO3* from defect/domain-wall interactions. *Applied Physics Letters*, 98(9), 2011.
- [133] T Choi, Y Horibe, HT Yi, YJ Choi, Weida Wu, and S-W Cheong. Insulating interlocked ferroelectric and structural antiphase domain walls in multiferroic *ymno3*. *Nature materials*, 9(3):253–258, 2010.
- [134] Lixin He and David Vanderbilt. First-principles study of oxygen-vacancy pinning of domain walls in *pbtio3*. *Phys. Rev. B*, 68:134103, Oct 2003.
- [135] Jan Seidel, Lane W Martin, Q He, Q Zhan, Y-H Chu, A Rother, ME Hawkrige, P Maksymovych, P Yu, M Gajek, et al. Conduction at domain walls in oxide multiferroics. *Nature materials*, 8(3):229–234, 2009.
- [136] SY Yang, J Seidel, SJ Byrnes, P Shafer, C-H Yang, MD Rossell, P Yu, Y-H Chu, JF Scott, JW Ager, et al. Above-bandgap voltages from ferroelectric photovoltaic devices. *Nature nanotechnology*, 5(2):143–147, 2010.
- [137] Yoon Seok Oh, Xuan Luo, Fei-Ting Huang, Yazhong Wang, and Sang-Wook Cheong. Experimental demonstration of hybrid improper ferroelectricity and the presence of abundant charged walls in (*ca*, *sr*) *3ti2o7* crystals. *Nature materials*, 14(4):407–413, 2015.
- [138] Yanan Geng, Nara Lee, YJ Choi, S-W Cheong, and Weida Wu. Collective magnetism at multiferroic vortex domain walls. *Nano letters*, 12(12):6055–6059, 2012.
- [139] Xueyun Wang, Fei-Ting Huang, Junjie Yang, Yoon Seok Oh, and Sang-Wook Cheong. Interlocked chiral/polar domain walls and large optical rotation in *ni3teo6*. *APL Materials*, 3(7):076105, 2015.
- [140] J. Padilla, W. Zhong, and David Vanderbilt. First-principles investigation of 180° domain walls in *batio3*. *Phys. Rev. B*, 53:R5969–R5973, Mar 1996.
- [141] Paul Groth. *Zeitschrift für Krystallographie und Mineralogie*, volume 11. Wilhelm Engelmann, 1893.

- [142] B. Meyer and David Vanderbilt. *Ab initio* study of ferroelectric domain walls in PbTiO_3 . *Phys. Rev. B*, 65:104111, Mar 2002.
- [143] Donghwa Lee, Haixuan Xu, Volkmar Dierolf, Venkatraman Gopalan, and Simon R. Phillpot. Structure and energetics of ferroelectric domain walls in LiNbO_3 from atomic-level simulations. *Phys. Rev. B*, 82:014104, Jul 2010.
- [144] Nicole A. Benedek and Turan Birol. 'ferroelectric' metals reexamined: fundamental mechanisms and design considerations for new materials. *J. Mater. Chem. C*, 2016.
- [145] I. D. Brown and D. Altermatt. Bond-valence parameters obtained from a systematic analysis of the Inorganic Crystal Structure Database. *Acta Crystallographica Section B*, 41(4):244–247, Aug 1985.
- [146] Young-Han Shin, Valentino R. Cooper, Ilya Grinberg, and Andrew M. Rappe. Development of a bond-valence molecular-dynamics model for complex oxides. *Phys. Rev. B*, 71:054104, Feb 2005.
- [147] Sharmila N. Shirodkar and Umesh V. Waghmare. Emergence of ferroelectricity at a metal-semiconductor transition in a $1t$ monolayer of MoS_2 . *Phys. Rev. Lett.*, 112:157601, Apr 2014.
- [148] Paul Z. Hanakata, Alexandra Carvalho, David K. Campbell, and Harold S. Park. Polarization and valley switching in monolayer group-iv monochalcogenides. *Phys. Rev. B*, 94:035304, Jul 2016.
- [149] Ruixiang Fei, Wei Kang, and Li Yang. Ferroelectricity and phase transitions in monolayer group-iv monochalcogenides. *Phys. Rev. Lett.*, 117:097601, Aug 2016.
- [150] R. Nourafkan and G. Kotliar. Electric polarization in correlated insulators. *Phys. Rev. B*, 88:155121, Oct 2013.
- [151] R. Nourafkan, G. Kotliar, and A.-M. S. Tremblay. Electric polarization of $\text{Sr}_{0.5}\text{Ba}_{0.5}\text{MnO}_3$: A multiferroic Mott insulator. *Phys. Rev. B*, 90:220405, Dec 2014.
- [152] G. Kotliar, S. Y. Savrasov, K. Haule, V. S. Oudovenko, O. Parcollet, and C. A. Marianetti. Electronic structure calculations with dynamical mean-field theory. *Rev. Mod. Phys.*, 78:865–951, Aug 2006.
- [153] Nicola A. Spaldin, Michael Fechner, Eric Bousquet, Alexander Balatsky, and Lars Nordström. Monopole-based formalism for the diagonal magnetoelectric response. *Phys. Rev. B*, 88:094429, Sep 2013.
- [154] D.I. Khomskii. Electric dipoles on magnetic monopoles in spin ice. *Nature communications*, 3:904, 2012.
- [155] Nicola A Spaldin, Manfred Fiebig, and Maxim Mostovoy. The toroidal moment in condensed-matter physics and its relation to the magnetoelectric effect. *Journal of Physics: Condensed Matter*, 20(43):434203, 2008.

- [156] S. Toyoda, N. Abe, S. Kimura, Y. H. Matsuda, T. Nomura, A. Ikeda, S. Takeyama, and T. Arima. One-way transparency of light in multiferroic Cu_2O_4 . *Phys. Rev. Lett.*, 115:267207, Dec 2015.
- [157] A Pimenov, AA Mukhin, V Yu Ivanov, VD Travkin, AM Balbashov, and A Loidl. Possible evidence for electromagnons in multiferroic manganites. *Nature Physics*, 2(2):97–100, 2006.
- [158] A. B. Sushkov, R. Valdés Aguilar, S. Park, S-W. Cheong, and H. D. Drew. Electromagnons in multiferroic Ym_2O_5 and tbm_2O_5 . *Phys. Rev. Lett.*, 98:027202, Jan 2007.